2009

Multiscale Modeling of Airway Inflammation Induced by Mechanical Ventilation

Kittisak Koombua
Virginia Commonwealth University

School of Engineering
Virginia Commonwealth University

This is to certify that the dissertation prepared by Kittisak Koombua entitled MULTISCALE MODELING OF AIRWAY INFLAMMATION INDUCED BY MECHANICAL VENTILATION has been approved by his committee as satisfactory completion of the dissertation requirement for the degree of Doctor of Philosophy in Engineering

Ramana M. Pidaparti, Ph.D., Dissertation Director, School of Engineering

P. Worth Longest, Ph.D., Committee Member, School of Engineering

Kevin R. Ward, M.D., Committee Member, School of Medicine

Dianne T.V. Pawluk, Ph.D., Committee Member, School of Engineering

Shijian Chu, Ph.D., Committee Member, School of Medicine

Mohamed Gad-el-Hak, Ph.D., Committee Member and Department Chair, School of Engineering

Rosalyn Hobson, Ph.D., Associate Dean for Graduate Studies, School of Engineering

Russell D. Jamison, Ph.D., Dean, School of Engineering

F. Douglas Boudinot, Ph.D., Dean, School of Graduate Studies

Date

MULTISCALE MODELING OF AIRWAY INFLAMMATION INDUCED BY
MECHANICAL VENTILATION

A Dissertation submitted in partial fulfillment of the requirements for the degree of
Doctor of Philosophy in Engineering at Virginia Commonwealth University.

by

KITTISAK KOOMBUA

M.S.M.E., Purdue School of Engineering and Technology, IUPUI, 2005
B.Eng., Chulalongkorn University, Thailand, 2001

Director: Ramana M. Pidaparti, Ph.D.
Professor, Department of Mechanical Engineering

Virginia Commonwealth University
Richmond, Virginia
August 2009

Acknowledgement

I would like to thank my advisor Dr. Ramana Pidaparti for his tremendous support, encouragement, and mentorship during the last four years. I could not have asked for a better advisor. With his knowledge and guidance, he helped me to make this dissertation a reality. Not only did he provide all research resources, he also encouraged me to go to many conferences and student competitions. He also gave me an opportunity to work on many projects, which helped me develop my modeling and simulation skill. I cannot thank Dr. Pidaparti enough for his never-ending support.

I would also like to thank Dr. P. Worth Longest, Dr. Mohamed Gad-el-Hak, Dr. Kevin R. Ward, Dr. Dianne T.V. Pawluk, and Dr. Shijian Chu, members of my dissertation committee, for their time and helpful advice about my dissertation. In addition, I would like to thank the faculty members and staffs of the Department of Mechanical Engineering for facilitating the excellent academic experience I have had here at Virginia Commonwealth University. I would also like to extend my thanks to Ms. Ann Yates for her advice and support during my graduate study.

Last but not least, I would like to thank my parents who have always been there for me and pushed me to keep going. I would have given up, if not for my parents. Thank you very much.

Table of Contents

List of Tables

List of Figures

Abstract

MULTISCALE MODELING OF AIRWAY INFLAMMATION INDUCED BY

MECHANICAL VENTILATION

By Kittisak Koombua, M.S.M.E.

A Dissertation submitted in partial fulfillment of the requirements for the degree of
Doctor of Philosophy in Engineering at Virginia Commonwealth University.

Virginia Commonwealth University, 2009

Major Director: Ramana M. Pidaparti, Ph.D.
Professor, Department of Mechanical Engineering

Mechanical ventilation (MV) is a system that partially or fully assists patients whose respiratory system fails to achieve a gas exchange function. However, MV can cause a ventilator-associated lung injury (VALI) or even contribute to a multiple organ dysfunction syndrome (MODS) in acute respiratory distress syndrome (ARDS) patients. Despite advances in today technologies, mortality rates for ARDS patient are still high. A better understanding of the interactions between airflow from mechanical ventilator and

the airway could provide useful information used to develop a better strategy to ventilate patients.

The mechanisms, which mechanical ventilation induces airway inflammation, are complex processes and cover a wide range of spatial scales. The multiscale model of the airway have been developed combining the computational models at organ, tissue, and cellular levels. A model at the organ level was used to study behaviors of the airway during mechanical ventilation. Strain distributions in each layer of the airway were investigated using a model at the tissue level. The cellular inflammatory responses during mechanical ventilation were investigated through the cellular automata (CA) model incorporating all biophysical processes during inflammatory responses.

The multiscale modeling framework started by obtaining airway displacements from the organ-level model. They were then transferred to the tissue-level model for determining the strain distributions in each airway layer. The strain levels in each layer were then transferred to the cellular-level model for inflammatory responses due to strain levels. The ratio of the number of damage cells to healthy cells was obtained through the cellular-level model. This ratio, in turn, modulated changes in the Young's modulus of elasticity at the tissue and organ levels.

The simulation results showed that high tidal volume (1400 cc) during mechanical ventilation can cause tissue injury due to high concentration of activated immune cells and low tidal volume during mechanical ventilation (700 cc) can prevent tissue injury during mechanical ventilation and can mitigate tissue injury from the high tidal volume ventilation. The multiscale model developed in this research could provide useful

information about how mechanical ventilation contributes to airway inflammation so that

a better strategy to ventilate patients can be developed.

CHAPTER 1 Introduction

1.1 Motivation

Incidence of respiratory failure in US is about 137-253 per 100,000 US population (Behrendt, 2000; Sather and Schuur, 2007). Patients with this symptom need mechanical ventilation since their respiratory system fails to achieve a gas exchange function. Mortality rates of these patients are about 36%-44% (Behrendt, 2000; Khilnani et al., 2004; Vasilyev et al., 1995). Evidence suggested that these patients died from dysfunction in other vital organs rather than respiratory failure (Flaatten et al., 2003). Mechanical ventilation can cause lung injury (Halbertsma et al., 2005) (see Figure 1.1). This mechanism is known as ventilator-associated lung injury (VALI). VALI is very severe, especially for acute respiratory distress syndrome (ARDS) patient since VALI can lead to systemic inflammatory response syndrome (SIRS) or even multiple organ dysfunction syndrome (MODS) through volutrauma, atelectrauma or biotrauma mechanisms (Imai and Slutsky, 2006). MODS is irreversible, with the mortality rates of 80% of all intensive care unit (ICU) deaths (Khadaroo and Marshall, 2002). Understanding of the mechanisms that mechanical ventilation induces inflammatory responses could lead to a paradigm shift in mechanical ventilation for patients with respiratory failures and could reduce mortality rates from MODS in ARDS patients.

1.2 Approach

Inflammatory responses in the airway induced by mechanical ventilation are complex processes dealing with a spatial scale that ranges from ~ 1 nm for proteins to ~ 1 cm for the airway. It is clear that no single model can cover a factor of 10^7 in a spatial scale. A practical approach is to develop many models that cover a limit range of the spatial scale and to develop a technique that links these models together to investigate the airway inflammation induced by mechanical ventilation.

The multiscale model consists of the organ-level, tissue-level, and cellular-level models (see Figure 1.2). To investigate inflammation development during mechanical ventilation, airway displacements at the organ-level model are first determined by performing a finite element (FE) analysis. The results of the airway displacements at the organ-level model are then used to define the applied boundary conditions for the tissue-level model. Strains in each tissue layer are calculated employing the finite element (FE) analysis. These strains in each layer are then transferred to the cellular-level model. Change in inflammatory responses at the cellular-level model is associated with the transferred strains from the tissue-level model. The ultimate goal of the research is to better understand the mechanisms, which mechanical ventilation contributes to airway inflammation so that a better strategy to mechanically ventilate patients without inducing VALI or MODS can be developed.
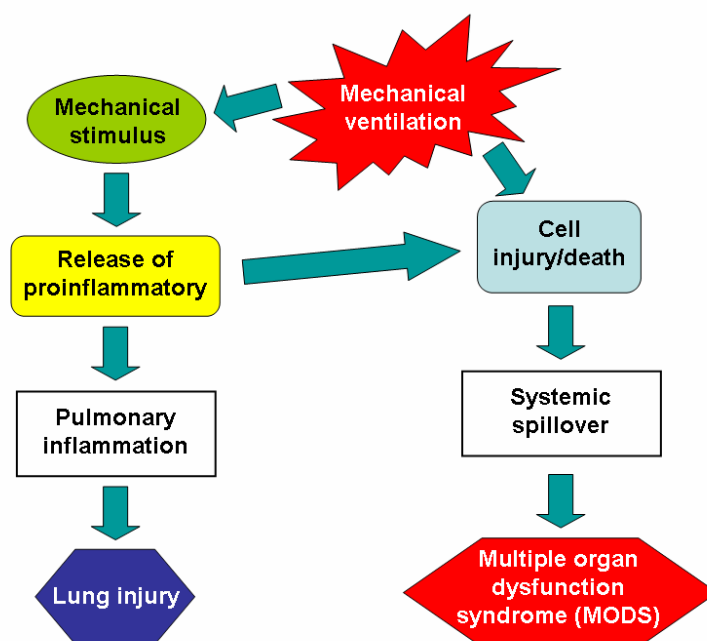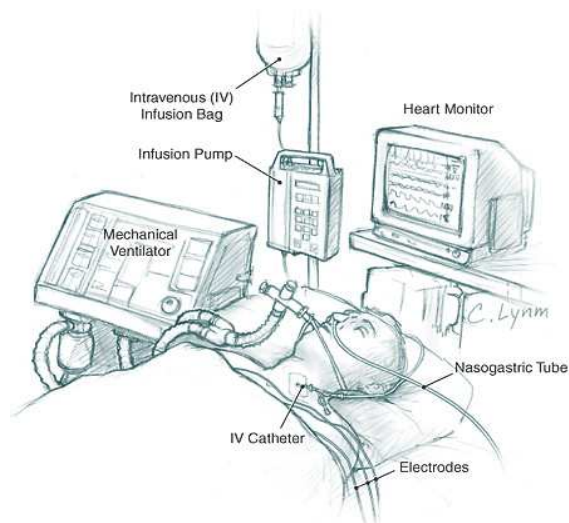
Figure 1.1   Mechanical ventilation for patients whose respiratory system fails to achieve a gas exchange function (top: image from www.madem.com) and the mechanism which mechanical ventilation contributes to lung injury or MODS (bottom)

1. Mechanical ventilation parameters (ultimate goal)

• Input parameters include tidal volume, flow waveform (constant, sine, or accelerating), maximum flow rate, inhalation-exhalation (I/E) ratio

2. Organ level model (objective 1)

• Input is mechanical ventilation parameters

• Finite element (FE) modeling will be used to address the interactions between airflow and airway walls on airway pressure and stresses

• Effects of airway diseases (tumor, asthma) on airway pressure and stresses

4. Cellular level model (objective 3)

• Input parameters are airway stresses and strains from the tissue level model

• Cellular automata (CA) model incorporating biophysical processes will be used to describe inflammatory responses during mechanical ventilation

Normal tissue Inflammation tissue
Images from www.answer.com

3. Tissue level model (objective 2)

• Input is airway pressure from the organ level model

• Finite element (FE) modeling will be used to investigate stress and strain distributions in each tissue layer

• Effects of material properties of airway walls on stress and strain distributions

Airway architecture image from Kamm [49]

5. Ventilator-associated lung injury, multiple organ dysfunction syndrome (MODS) and death

• Input parameters are number of damage and immune cells from the cellular level model

• Inflammation induced by mechanical ventilation contributes to lung injury or MODS

Figure 1.2   Components of the multiscale model for airway inflammation induced by mechanical ventilation

1.3 Specific Objectives

The ultimate goal of the research is achieved through the following four objectives.

Objective 1: Develop the organ-level model for studying the behaviors of the airway during mechanical ventilation. The continuum model incorporating the interactions between airflow and the airway wall is used to describe the behaviors of this level.

Objective 2: Develop the tissue-level model for studying the behaviors of the airway tissue during mechanical ventilation. The continuum model incorporating the heterogeneity of the airway wall is used to describe the behaviors of this level.

Objective 3: Develop the cellular-level model for studying the behaviors of the inflammatory responses during mechanical ventilation. The discrete model incorporating all biophysical processes during the inflammatory responses is used to describe the behaviors of this level.

Objective 4: Develop the multiscale model for airway inflammation induced by mechanical ventilation. The multiscale model is composed of the organ-level, tissue-level, and cellular-level models.

1.4 Background and Significance

1.4.1 <u>Mechanical Ventilation and Current Issues</u>

Mechanical ventilation is a method that partially or fully assists patients whose respiratory system fails to achieve a gas exchange function due to acute lung injury (ALI), acute respiratory distress syndrome (ARDS), airway disease, pulmonary vascular disease, or parenchymal lung disease (Lumb, 2005). It can be considered as an art more than a science since physicians must balance between gas exchange rate and tidal volume to prevent ventilator-associated lung injury (VALI) and it is critical, especially, for patients in an intensive care unit (ICU) with ARDS since VALI might contribute to a multiple organ dysfunction syndrome (MODS) from volutrauma, atelectrauma or biotrauma mechanisms (Imai and Slutsky, 2006) (see Figure 1.1). Despite advances in today technologies, the mortality rate in patients with ARDS remains very high. According to recent studies, the mortality rates are about 52% in US (Reynolds et al., 1998) and 42% in Europe (Ruffini et al., 2001).

Many techniques have been suggested to prevent VALI by using positive end-expiratory pressure (PEEP) and lowering the tidal volume and airway pressure (Lumb, 2005); however, there are some drawbacks. Lowering the tidal volume can cause hypercapnia, decrease in aerated lung volume, and increase in shunting and worsening oxygenation (Tobin, 2001). In addition, PEEP can cause transient oxygen desaturation, hypotension, barotrauma, arrhythmia, and bacterial translocation (Fan et al., 2005). A better strategy to mechanical ventilate patients with respiratory failure is needed to prevent VALI and reduce mortality rates from MODS in ARDS patients.

1.4.2 *In Vivo* and *In Vitro* Models for Studying Effects of Force on Airways

Knowledge about the interactions between airflow and the airway wall in the human respiratory system is the first step for understanding mechanisms during mechanical ventilation. The human airway is shaped by the complex mechanical environment even in the uterus. This complex mechanical environment continues to influence and alter the mature airway in healthy and diseased people (Tschumperlin and Drazen, 2006). Many *in vivo* and *in vitro* models have been developed to study the effect of a mechanical stress on the airway wall.

An *in vivo* experiment by Ranieri et al. (1999) and Dhanireddy et al. (2006) showed that high peak airway pressure from the conventional mechanical ventilation caused airway distention and an increase in the level of a proinflammatory mediator, cytokine. This overproduction of cytokine can exacerbate lung injury and can even lead to a mortality of patient with ALI or ARDS. Goldstein et al. (2001) supported previous studies by showing that mechanical ventilation in piglet model not only caused alveolar distention, but also induced bronchiolar distention.

Swartz et al. (2001) applied a hydrostatic pressure on the cultured airway epithelial cells which were in contact with the cultured fibroblasts via a soluble mediator. Their results showed that a mechanical stress increased the level of Egr-I, fibronectin protein, and MMP-9/TIMP-1 ratio. These increases in Egr-I protein, fibronectin protein, and MMP-9/TIMP-1 ratio from a mechanical stress are also observed in the airway thickening responses of patients with asthma. Choe et al. (2003) developed a three-

dimensional *in vitro* airway wall model composed of fibroblasts suspended in a collagen matrix and bronchial epithelial cells to study the effects of a mechanical stress on airway wall remodeling. Their results showed that a mechanical stress caused an increase in the thickness of the epithelial layer.

None of the *in vivo* and *in vitro* models mentioned earlier can describe how the mechanical stress/strain distributes throughout the airways. Understanding the stress/strain distributions could be helpful for preventing airway distention and reducing VALI in patients with respiratory failure.

1.4.3 Computational Models for Investigating Airflow in Airways

Since measuring the airflow field in the human airways during mechanical ventilation is very difficult, a computational model can help researchers or physicians to investigate this airflow field. Many researchers have developed computational models to investigate the effects of airway diseases, e.g., tumors (Guan et al., 2000; Kleinstreuer and Zhang, 2003; Martonen and Guan, 2001a; Martonen and Guan, 2001b; Segal et al., 2000), asthma (Longest et al., 2006), stenosis (Brouns et al., 2007), COPD (Luo et al., 2007; Yang et al., 2006), and airway geometry, e.g., carinal shape (Martonen et al., 1994) and cartilage rings (Zhang and Finlay, 2005), on airflow and particle deposition in the airway bifurcation.

However, these models failed to consider the interactions between airflow and the airway wall. In other words, the airway wall was assumed to be rigid and could not be

deformed or distended by fluid force from the airflow. Human airways are, in fact, soft tissues and can be distended by airflow during mechanical ventilation (Lumb, 2005). Therefore, the computational model that incorporates the interactions between airflow and the airway wall is needed in order to investigate the airflow in our airways during mechanical ventilation.

1.5 Organization of the Dissertation

The remainder of the dissertation is organized as follows. Chapter 2 discusses the details used to develop the organ-level model. The results of the organ-level model are also provided. Chapter 3 describes the procedures and the continuum model used to develop the tissue-level model. The results from the tissue-level model are also discussed. Chapter 4 provides all details of the cellular-level model and the results of the cellular-level model. Chapter 5 illustrates the techniques that are used to develop the multiscale model. Applications of the multiscale model to clinical care are also demonstrated through case studies. Finally, scientific contributions of the research and recommendations for other researchers are presented in the Chapter 6.

CHAPTER 2 Organ-Level Models

2.1 Introduction

Based on Weibel (1963), airways can be numbered successively from the trachea (generation 0) down to the alveolar sacs (generation 23). Each generation bifurcates into two smaller daughter branches; therefore the number of the airways in each generation is indicated by the number 2 rose to the power of the generation number. The airways can be separated into two zones (conducting and respiratory zones) based on their functions (Hlastala and Berger, 2001). The conduction airways transport air between the outside and the gas-exchanging region of the lung. The function of the airways gradually changes from conducting to gas exchange as the airways progress down to the respiratory zone. Many computational models have been developed for studying airflow in the airways (Brouns et al., 2007; Guan et al., 2000; Kleinstreuer and Zhang, 2003; Longest et al., 2006; Martonen and Guan, 2001a; Martonen et al., 1994; Segal et al., 2000; Yang et al., 2006); however, those models failed to consider the interactions between airflow and the airway wall. In other words, the airway wall was assumed to be rigid and could not be deformed or distended by fluid force from the airflow. The more detailed computational

model that incorporates the interactions between airflow and the airway wall could lead to better understanding of the mechanisms during mechanical ventilation.

In this chapter, the detail geometry and computational method of the organ-level model are described. The continuum model that incorporates the interactions between airflow and the airway wall is employed to study the effects of mechanical ventilation parameters and airway diseases on airway pressure and airway strains.

2.2 Airway Geometry

The research will focus mainly on airway generations 3 to 5 for three reasons. First, these airway generations are in the conducting zone (Hlastala and Berger, 2001). There is no gas-exchanging process in this zone. Second, these airway generations have less cartilage plates and no rings when compared to the proximal generations; therefore the airway wall is assumed to be smooth (Hlastala and Berger, 2001). Third, diameters of these airways do not change as a function of a lung volume but their diameters depend on a transmural pressure across the airway wall (Lumb, 2005).The geometric dimensions of airway generations 3 to 5 used for an organ-level model are based on the ICRP (1994) tracheobronchial geometry and airway thickness for each generation is based on measurement by Habib et al. (1994). The branching angle of the bifurcation is 70° based on the morphological data of Horsfield and Cumming (1967). The surface geometry of the model is constructed based on the physiologically realistic bifurcation (PRB) model suggested by Heistracher and Hofmann (Heistracher and Hofmann, 1995) (see Figure

2.1). The corresponding geometric diameter, length, and thickness of the bifurcation are

tabulated in Table 2.1.
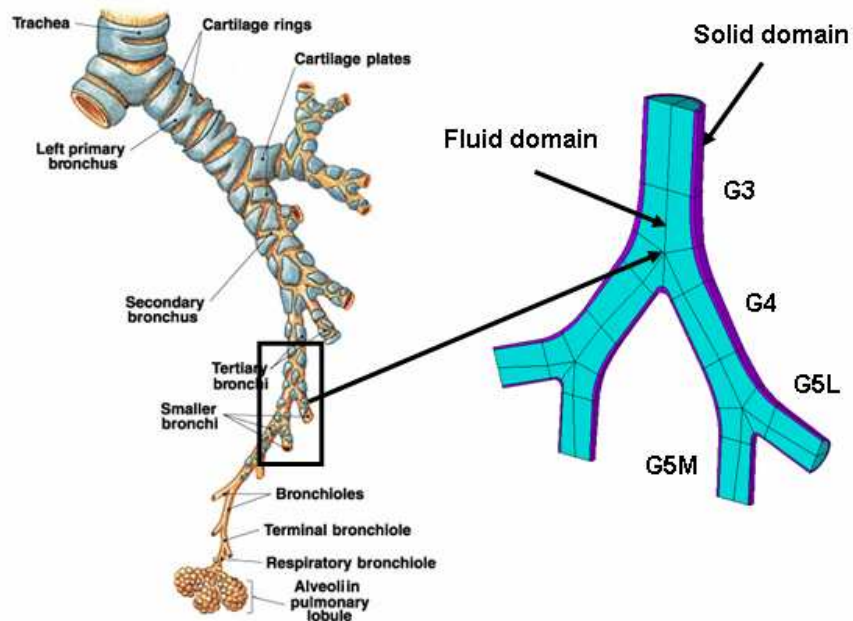
Figure 2.1   Geometric representations of the airway bifurcation generations 3 to 5 based on ICRP (1994) tracheobronchial geometry and measurement by Habib et al. (1994). These bifurcations are used as a computational domain for the organ level model.

Table 2.1   Parameters for airway generations 3 to 5 based on ICRP (1994) tracheobronchial geometry and measurement by Habib et al. (1994)

Generation	Diameter (cm)	Length (cm)	Thickness (cm)
3	0.56	1.10	0.053
4	0.45	0.92	0.041
5	0.36	0.77	0.024

2.3 Governing Equations and Computational Method

The transient interactions between airflow and the airway wall during mechanical ventilation are investigated by solving two coupled sets of the governing equations with associated boundary conditions.

The governing equations for transient airflow are Navier-Stokes equations on a moving mesh with the assumption of incompressible flow. These equations govern the principles of mass and momentum conservation and are described below using Einstein's repeated index convention (Longest and Kleinstreuer, 2005).

Conservation of mass

$$\frac{\rho_g}{\sqrt{g}} \frac{\partial}{\partial t}\left(\sqrt{g}\right) + \rho_g \frac{\partial}{\partial x_j}\left(u_j - \frac{\partial \tilde{x}_j}{\partial t}\right) = 0 \qquad (1)$$

Conservation of momentum

$$\frac{\rho_g}{\sqrt{g}} \frac{\partial}{\partial t}\left(\sqrt{g}\, u_i\right) + \rho_g \frac{\partial}{\partial x_j}\left[\left(u_j - \frac{\partial \tilde{x}_j}{\partial t}\right)u_i\right] = -\frac{\partial p}{\partial x_i} + \mu \frac{\partial^2 u_i}{\partial x_j^2} \qquad (2)$$

In these equations, $\tilde{x}_i$ represents the moving mesh location, $\sqrt{g}$ is the metric tensor determinate of the transformation, i.e., the local computational control-volume size, ρ_g is fluid density, p is fluid pressure, μ is fluid viscosity, and u is fluid velocity.

The governing relations for movement of the airway wall during mechanical ventilation are the time-dependent structural equations and are described below using Einstein's repeated index convention (Reddy, 1993).

Equation of motion

$$\frac{\partial \sigma_{ij}}{\partial x_j} + F_i = \rho \frac{\partial^2 u_i}{\partial t^2} \tag{3}$$

Constitutive relations

$$\sigma_{ij} = C_{ijkl} \varepsilon_{kl} \tag{4}$$

In the equation above, σ is the stress in each direction, F is the body force, ρ is density, u is the displacement, C is the elasticity tensor, and ε is the strain in each direction.

The effect of fluid pressure on a structure is significant, especially if the structure is flexible, such as human airways. The numerical solutions of the interaction between airflow and airway walls during mechanical ventilation were implemented using two software packages, ANSYS and ANSYS CFX. ASNYS is general-purpose finite element (FE) software for structural modeling and ANSYS CFX is general-purpose computational fluid dynamics (CFD) software for modeling fluid flows. The fluid-structure interaction (FSI) procedures begin by solving the flow equations to obtain fluid pressure. Structural

equations are then solved for the displacement using the fluid pressure as an external force. The flow equations are solved again to obtain the fluid pressure after the structural displacement changes the fluid boundaries. This loop continues until both fluid pressure and structural displacement converge for each time period (ANSYS, 2005) (see Figure 2.2).
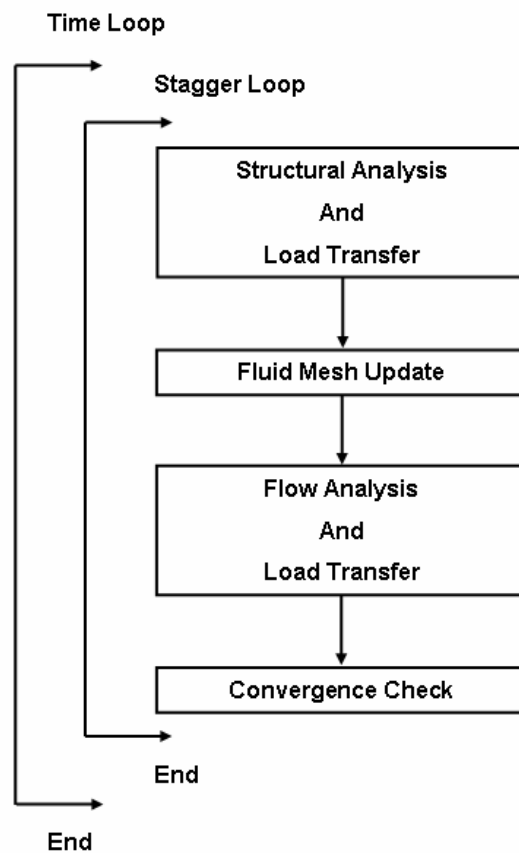
Figure 2.2   A diagram of the fluid-structure interaction (FSI) algorithm.

2.4 Computational Models and Boundary Conditions

The computational domains of the bifurcation are created in ANSYS and ANSYS CFX. Due to symmetry, only one half of the domains are constructed. The solid domain is the airway wall with a finite thickness and the fluid domain is the internal volume of air in the bifurcation. Solid elements, BRICK45 (ANSYS, 2005), are used to represent the solid domain and fluid elements, FLUID142 (ANSYS, 2005), are used to represent the fluid domain. A structural hexahedral mesh is employed to provide a high quality flow field solution, as suggested by Longest and Vinchurkar (2007) and Vinchurkar and Longest (2008).

The inlet boundary condition of the fluid domain is an airflow waveform, which is produced by mechanical ventilation in intubated patients. The properties of air are assumed to be those at 27 °C. A pressure accounting for an impedance pressure for the rest of the airways was applied at the outlet of the fluid domain (Vassiliou et al., 2000). A no-slip boundary condition is applied at the fluid-solid interface. A zero-displacement boundary condition is applied to the solid domain at both inlet and outlet to represent a tethering of the airway wall from other tissues and organs (Plopper et al., 2003). Figure 2.3 shows the finite element model and all boundary conditions that are used for the organ-level model. The normal airway wall at the organ-level model are assumed to be of a homogeneous and orthotropic material with a density of 1365.6 kg/m^3 (Sera et al., 2003), a Young's modulus of elasticity in longitudinal direction of 130.89 kPa (Croteau

and Cook, 1961), a Young's modulus of elasticity in circumferential direction of 74.07

kPa (Prakash and Hyatt, 1978), and Poisson's ratio of 0.45 (Prakash and Hyatt, 1978).
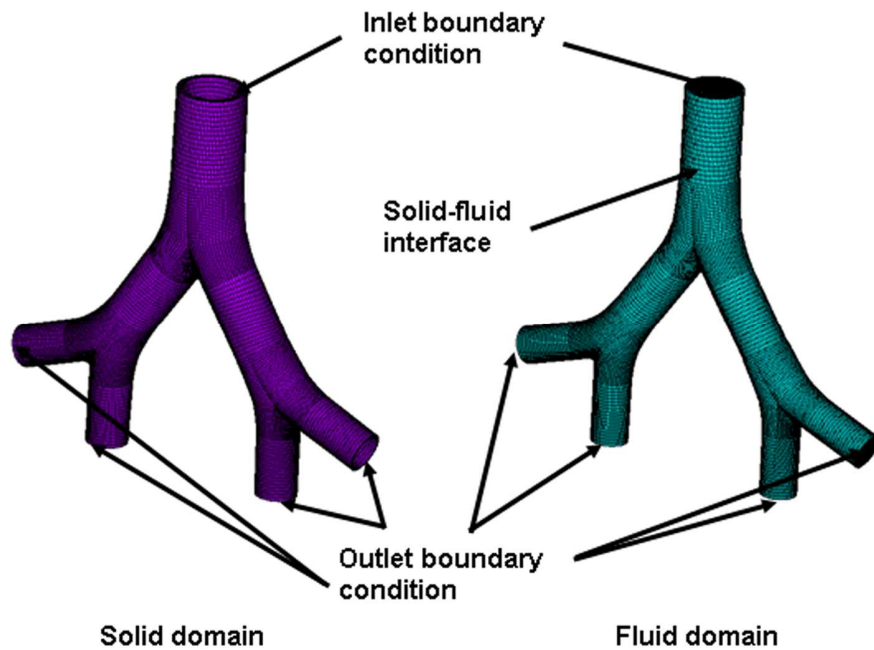
Figure 2.3   The finite element model of the airway bifurcation generations 3 to 5 for the organ-level model and the boundary conditions for both solid and fluid domains.

2.5 Model Validation

A mesh-independence study was performed on the solid and fluid domains to confirm that a fine enough element had been used to represent both solid and fluid domains. The mesh-independence study begun with a mesh discretization and recorded a solution. Then the finer elements were used to represented both solid and fluid domains. The results from the finer-element model were then compared with those from the first model. If the results are nearly similar, then the first mesh is probably good enough for

that particular geometry, loading and constraints. If the results differ by a large amount, the process was repeated with the finer elements. Maximum pressure and velocity were used as convergence criteria for the fluid domain and maximum displacement and von Mises strain were used as convergence criteria for the solid domain. A converged model was obtained when changes in those solutions were less than 5%. Having performed the mesh-independence study, the airflow velocity from the finite element model for a single bifurcation was then compared to the experiment by Zhao & Lieber (1994) (see Figure 2.4).
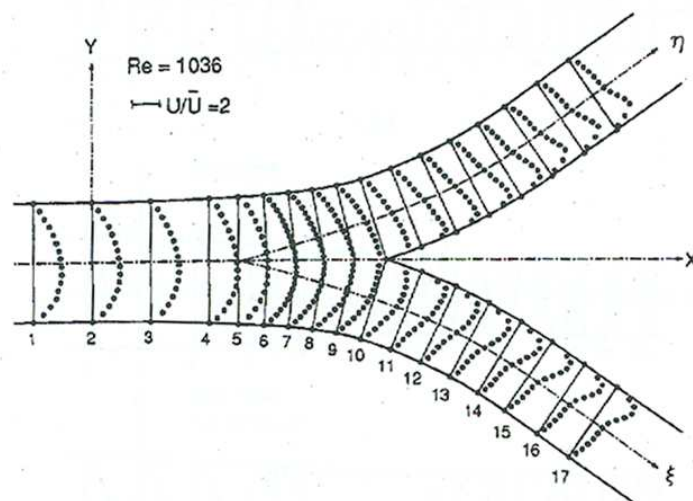
Figure 2.4   Airflow velocity in the symmetric bifurcation. Images are from the experiment by Zhao & Lieber (1994).

2.6 Method of Analysis

2.6.1 Effect of Airflow Rate

The effect of airflow rate during mechanical ventilation on airway pressure and strains in the airway wall were studied by implementing three flow rate waveforms: 30, 60, and 90 l/min in the trachea. The flow rate at the airway generation 3 was obtained assuming that flow divides equally at each bifurcation. The obtained flow rate was then applied as the inlet boundary condition of the fluid domain. Based on the previous experiment by Zhao & Lieber (1994), the airflow was assumed to be a laminar flow for the cases of 30 and 60 l/min. However, airflow becomes a turbulent flow for flow rate 90 l/min. In order to take this aspect into account for higher airflow rates from mechanical ventilation, the shear stress transport (SST) model was employed in the computational model. The flow waveforms from mechanical ventilation were characterized by active constant inhalation and passive exhalation. The flow waveforms were constructed assuming that the tidal volume was 700 cm^3. The passive exhalation was described by the following equation.

$$v\left(t\right) = -\frac{V_0}{\tau}e^{-t/\tau}$$ (5)

where v is airflow velocity (m/s), t is time (s), V_0 is the tidal volume (cm^3), and τ is a time constant equal to the product of lung compliance and resistance. The time constant in this study was chosen such that the ratios between the duration of inhalation and exhalation were 1/2, 1/4, and 1/8 for airflow rates of 30, 60, and 90 l/min, respectively (Lumb, 2005).

2.6.2 <u>Effect of Airflow Waveform</u>

Four waveforms from mechanical ventilation were chosen for this study. These waveforms were ascending, descending, constant, and sine waveform. To construct the active inhalation flow waveform, the lung was assumed to be inflated 700 cc in 0.7-s duration and the ratio between a minimum airflow rate and a maximum airflow rate was assumed to be 1/3 for ascending and descending flow waveforms. The passive exhalation flow waveform was described by equation (5).

2.6.3 <u>Effect of Tidal Volume</u>

This analysis was based on three tidal volume–namely 350, 700, and 1400 cc. These tidal volumes represent low volume (6 cm^3/kg), mean volume (12 cm^3/kg), and high volume (25 cm^3/kg) (Sinclair et al., 2007). The airflow rate of 60 l/min with constant flow waveform was chosen for this analysis.

2.6.4 <u>Effect of Positive End-Expiratory Pressure</u>

Positive end-expiratory pressure (PEEP) refers to the amount of above atmospheric pressure in the airway at the end of passive expiration. PEEP is used mainly to recruit or stabilize lung units and improve oxygenation in patients (Lumb, 2005). The constant flow waveform with the airflow rate of 60 l/min was chosen for this study. Three

positive end-expiratory pressures (PEEP) were employed: 0, 5, and 10 hPa. To account for an impedance pressure for the rest of the airways, the equation developed by Vassiliou et al. (2000) was used to calculate the pressure at the outlet of the fluid domain for each PEEP.

2.6.5 <u>Effect of Airway Constriction from Airway Disease</u>

The effect of airway constriction from airway diseases on airway pressure and airway strains was investigated by employing two types of airway disease: tumor and asthma. The simplified spherical tumor was introduced at the first bifurcation between airway generations 3 and 4. The tumor was assumed to be isotropic material with a Young's modulus of elasticity of 81.5 kPa (Weisenhorn et al., 1993) and density of 1047 kg/m^3 (Reitz et al., 2008). The parametric study was performed to study the effect of tumor size and stiffness on airway pressure and airway strains. The tumor size was varied by changing a ratio between tumor radius and airway radius from 0 to 1. The 0 represents no tumor and the 1 represents a half obstruction of the airway. For a tumor stiffness parametric study, the stiffness was varied from 15-150 kPa. This range is a normal range of the stiffness for the tumor (Weisenhorn et al., 1993).

The airway thickening was introduced for the asthma disease. The asthmatic airway was two-time thicker than the normal airway (Kamm, 1999). Thickness of each layer for the asthmatic airway is obtained from the histological section of airway tissue (Benayoun et al., 2003) and it is 460, 230, and 110 μm for mucosa, smooth muscle, and

cartilage layer, respectively. Material properties of the homogeneous asthma airway can be calculated using material properties of each tissue layer (see Table 2.2) and a composite-material theory (Barbero, 1999).

$$E = V_{mu\cos a} E_{mu\cos a} + V_{SM} E_{SM} + V_{cartilage} E_{cartilage} \qquad (8)$$

In the above equation, E is a Young's modulus of elasticity of the homogeneous airway wall, $E_{mu\cos a}$ is a Young's modulus of elasticity of the mucosa, E_{SM} is a Young's modulus of elasticity of the smooth muscle, $E_{cartilage}$ is a Young's modulus of elasticity of the cartilage, $V_{mu\cos a}$ is a volume fraction of the mucosa, V_{SM} is a volume fraction of the smooth muscle, and $V_{cartilage}$ is a volume fraction of the cartilage. The volume fraction of each layer is a ratio of the thickness in each layer to total thickness of the airway tissue.

Table 2.2   Material properties of each layer in the airway wall

Airway wall layer	Young's modulus (kPa)	
Mucosa (Yamada, 1970)	Circumferential	80
	Longitudinal	150
Smooth muscle with cartilage (Jiang and Stephens, 1990)	Circumferential	75
	Longitudinal	75

Substituting values of the Young's modulus for Table 2.2 and the volume fraction for each layer into (8), we obtain

In a circumferential direction

$$E = \frac{460}{820}(80) + \frac{250}{820}(75) + \frac{110}{820}(75) = 78 \quad kPa$$

In a longitudinal direction

$$E = \frac{460}{820}(150) + \frac{250}{820}(75) + \frac{110}{820}(75) = 120 \quad kPa$$

2.6.6 Airflow velocity, Pressure, and Strain at Alveolar-Sac Level

Airflow velocity, airway pressure and airway strains at the alveolar-sac level were investigated using the simplified model of the alveolar sac. The alveolar sac has a diameter of 500 μm. The alveolar duct diameter was 200 μm and the entrance length was

100 μm (Dailey and Ghadiali, 2007). Thickness of the alveolar sac is 0.3 μm (Lumb, 2005). The alveolar sac was assumed to be homogeneous and isotropic material with the Young's modulus of 80 kPa (Yamada, 1970) and Poisson's ratio of 0.45 (Prakash and Hyatt, 1978). The parametric study was performed to investigate an effect of tidal volume on airway pressure and airway strains. The constant flow waveform of 60 l/min with three tidal volumes (350, 700 and 1400 cc) was chosen for this analysis.

2.7 Results

2.7.1 Validation against Measurement in a Single Bifurcation

Figure 2.5 shows a comparison of the axial velocity in the airway generation 4 between the finite element solutions and the experimental results from Zhao & Lieber (1994). As can be seen from this figure, the finite element solutions and the experimental results were in good agreement. The axial velocity in the bifurcation plane had a skewed velocity profile toward the inside wall. The axial velocity in the vertical plane had an M-shape profile. These skewed velocity and M-shape profiles were from the effect of a secondary flow after the bifurcation.
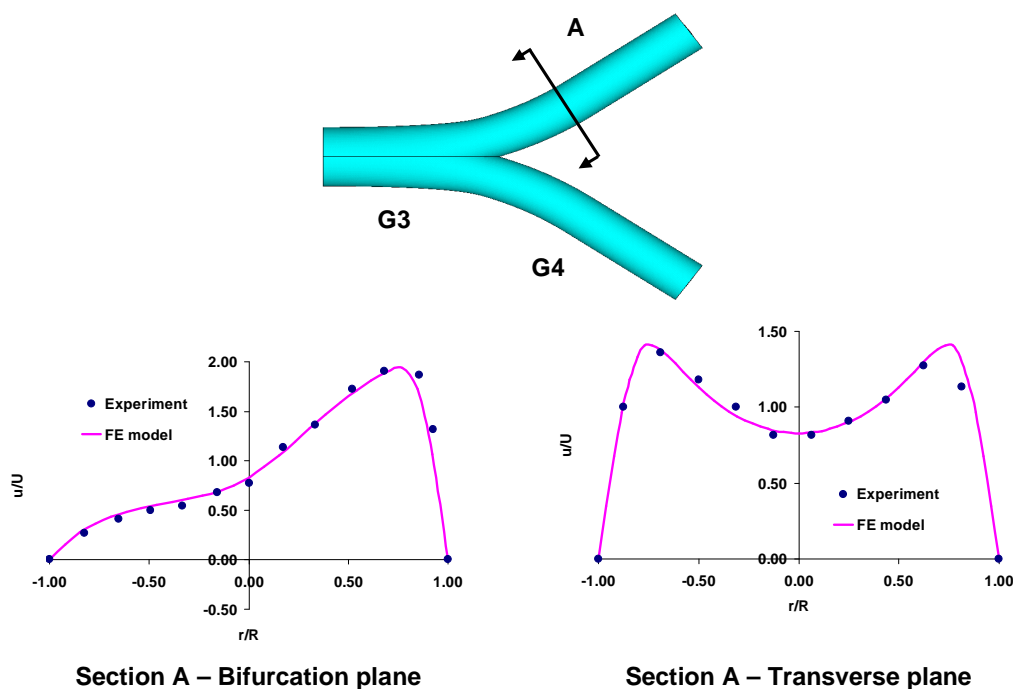
Figure 2.5   A validation between the computational and experimental results of airflow velocity in the airway generation 4.

2.7.2 Airflow Velocity and Airway Pressure

Airflow velocity and airway pressure distributions for all normal airway cases were similar. For brevity, results of the 60-l/min constant flow rate were shown here. High airflow velocity spread throughout G3. After the first bifurcation, high airflow velocity moved toward medial side of G4. Airflow velocity in both G3 and G4 was symmetric; however velocity profiles in G5 were not symmetric. Airflow velocity in the branch G5M was higher than that in the branch G5L (see Figure 2.6). The difference in airflow velocity in G5 was from high airflow velocity at the medial side of G4. The maximum airflow velocity for 60 l/min was 6.00 m/s.

High airway pressure areas were at the beginning of G3 and at the bifurcations at the end of inhalation (see Figure 2.7). The pressure at the first bifurcation between G3 and G4 was higher than that at the second bifurcation between G4 and G5. The maximum airway pressure at the end of inhalation for 60 l/min was 95.33 Pa.
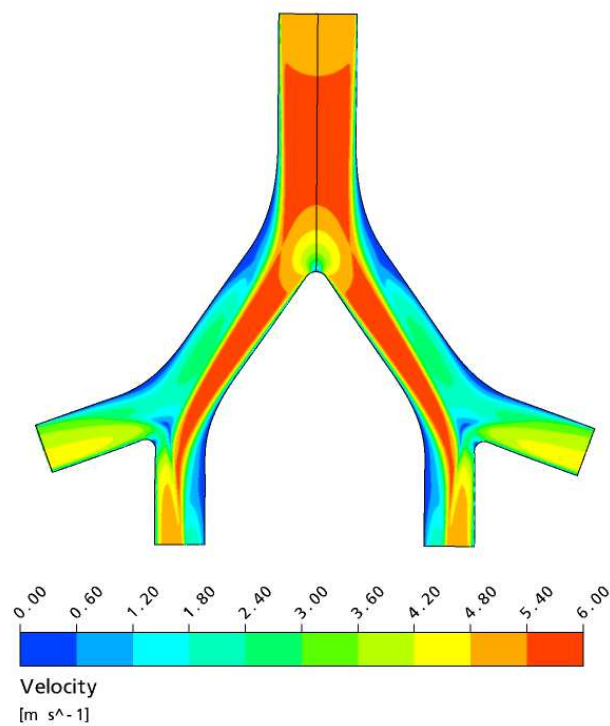
Figure 2.6   Airflow velocity at the end of inhalation for airflow rate of 60 l/min with a constant flow waveform
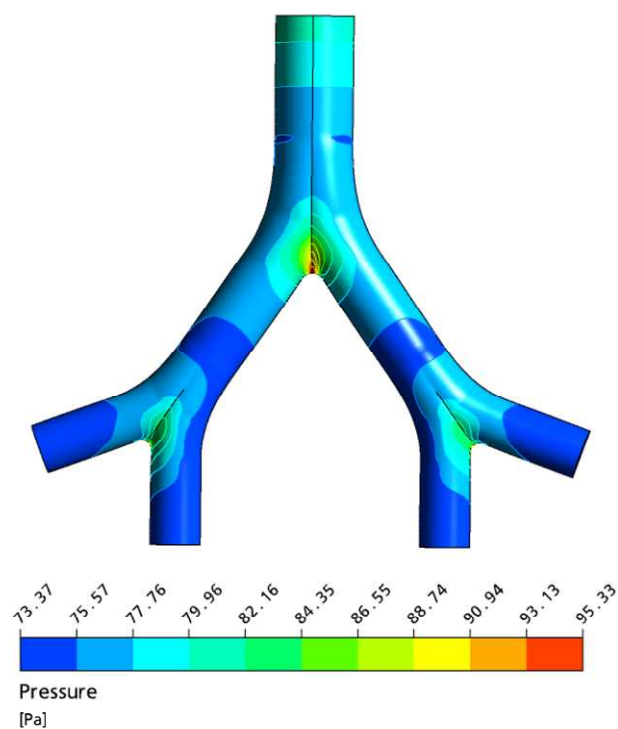
Figure 2.7   Airway pressure at the end of inhalation for airflow rate of 60 l/min with a constant flow waveform

2.7.3 Airway Displacement and Airway Strains

Airway displacement and airway strain distributions for all normal airway cases were similar. For brevity, results of the 60-l/min constant flow rate were shown here. High airway displacements were at the bifurcations at the end of inhalation (see Figure 2.8). The airway displacements at the first bifurcation were lower than those at the second bifurcation. The maximum airway displacement for 60 l/min was 0.3 mm (about 13 % increases in airway diameter).
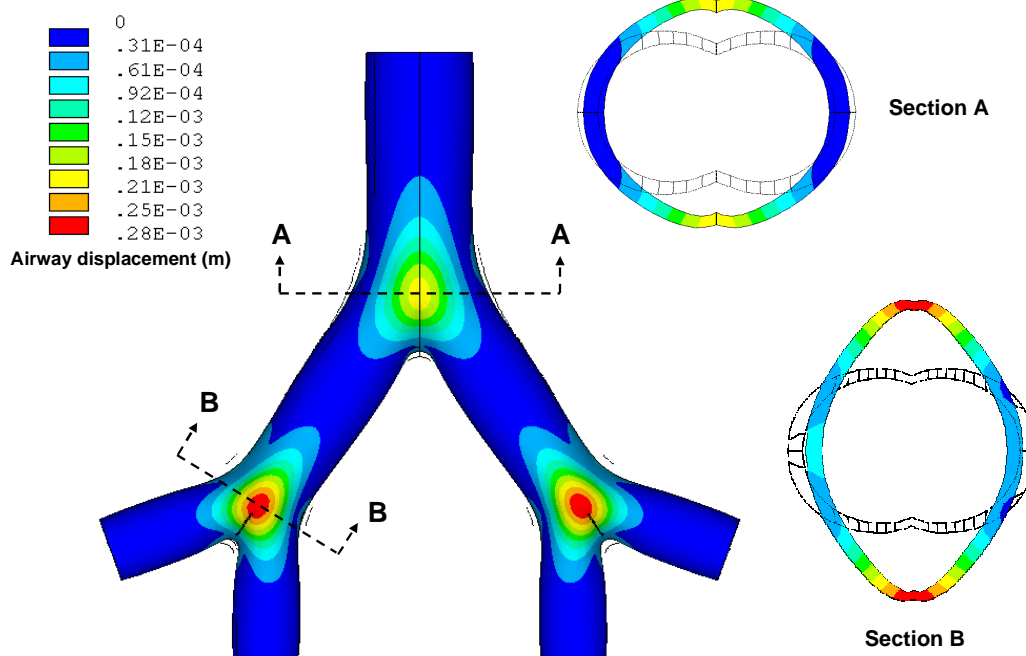
Figure 2.8   Airway displacement at the end of inhalation for airflow rate of 60 l/min with a constant flow waveform

Figure 2.9 shows distributions airway strains in both longitudinal and circumferential directions at the end inhalation. High longitudinal and circumferential strains were observed at the bifurcation. The highest longitudinal and circumferential strains were at the second bifurcation. The strain levels are higher in circumferential direction in comparison to the longitudinal direction, which means that airways distended more in the circumferential direction than in the longitudinal direction. In the longitudinal direction, the maximum strain levels are 2.9%, whereas in the circumferential direction, the maximum strain levels are 4.8%.
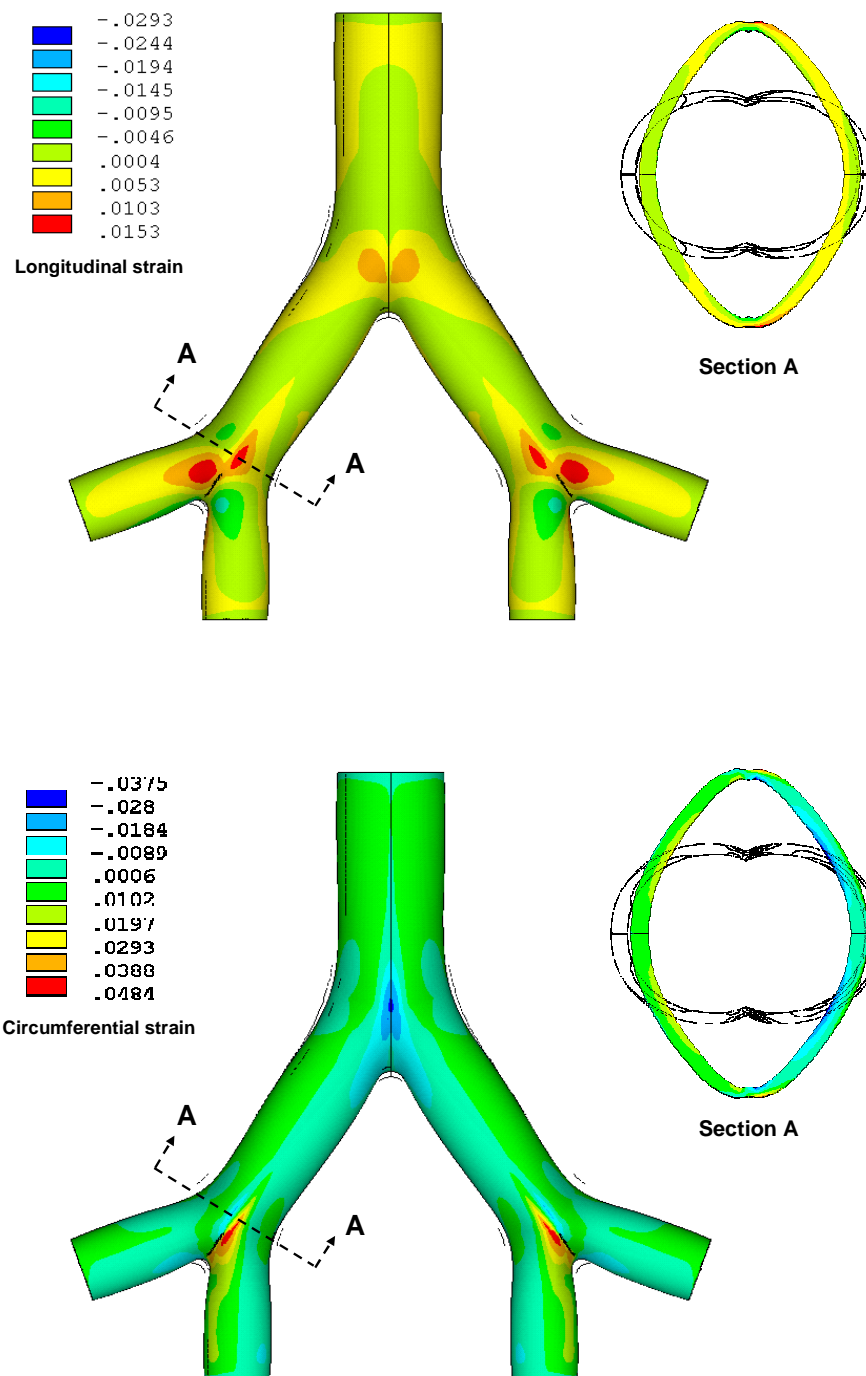
Figure 2.9   Airway strains in longitudinal (top) and circumferential (bottom) direction at the end of inhalation for airflow rate of 60 l/min with a constant flow waveform

2.7.4 <u>Effect of Airflow Rate</u>

The effect of airflow rate was investigated employing three airflow rates: 30, 60, and 90 l/min (see Figure 2.10). Figure 2.11 shows the effect of airflow rate on airflow velocity, airway pressure, and airway strains. As can be seen from this figure, airflow rate affects each parameter in different degrees. Airflow rate highly affected airflow velocity. A maximum airflow velocity increased about 46% and 34% when airflow rate increased from 30 l/min to 60 and 90 l/min, respectively. A maximum airway pressure increased about 29% and 23% when airflow rate increased from 30 l/min to 60 and 90 l/min, respectively. A maximum airway displacement increased about 21% and 18% when airflow rate increased from 30 l/min to 60 and 90 l/min, respectively. A maximum longitudinal strain increased about 21% and 17% when airflow rate increased from 30 l/min to 60 and 90 l/min, respectively. A maximum circumferential strain increased about 24% and 16% when airflow rate increased from 30 l/min to 60 and 90 l/min, respectively.
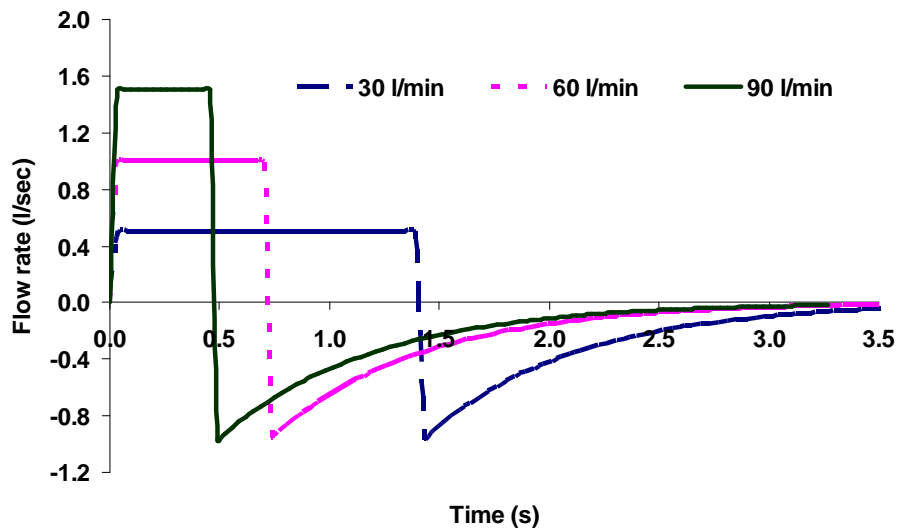
Figure 2.10 Flow waveforms of active inhalation with a constant flow rate and passive exhalation for airflow rates of 30, 60, and 90 l/min
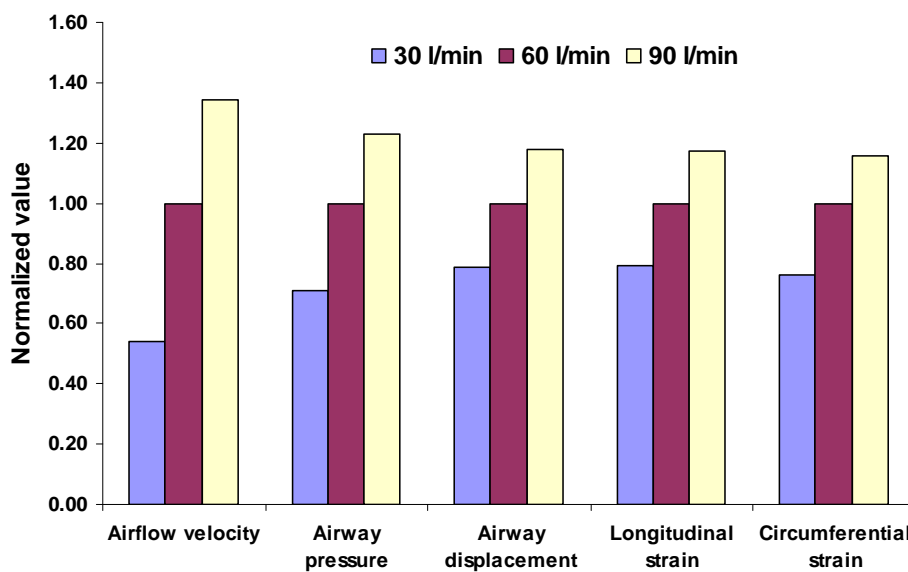
Figure 2.11 Effect of airflow rate from mechanical ventilation on airflow velocity, airway pressure, airway displacement, longitudinal strain, and circumferential strain. The normalized values are based on airflow rate of 60 l/min.

2.7.5 <u>Effect of Airflow Waveform</u>

This analysis was based on four airflow waveform from mechanical ventilation: ascending, constant, descending, and sine (see Figure 2.12). The effect of airflow waveform on airflow velocity, airway pressure, and airway strains is shown in Figure 2.13. The normalized values in this figure were based on the constant flow waveform. As can be seen, sine waveform provides the highest airflow velocity, which was about 44% higher than the constant flow waveform. Airway pressure, airway displacement, and airway strains were lowest for the descending waveform. They were about 17%, 11%, 11%, and 12% lower than the constant flow waveform for airway pressure, airway displacement, longitudinal strain, and circumferential strain, respectively.
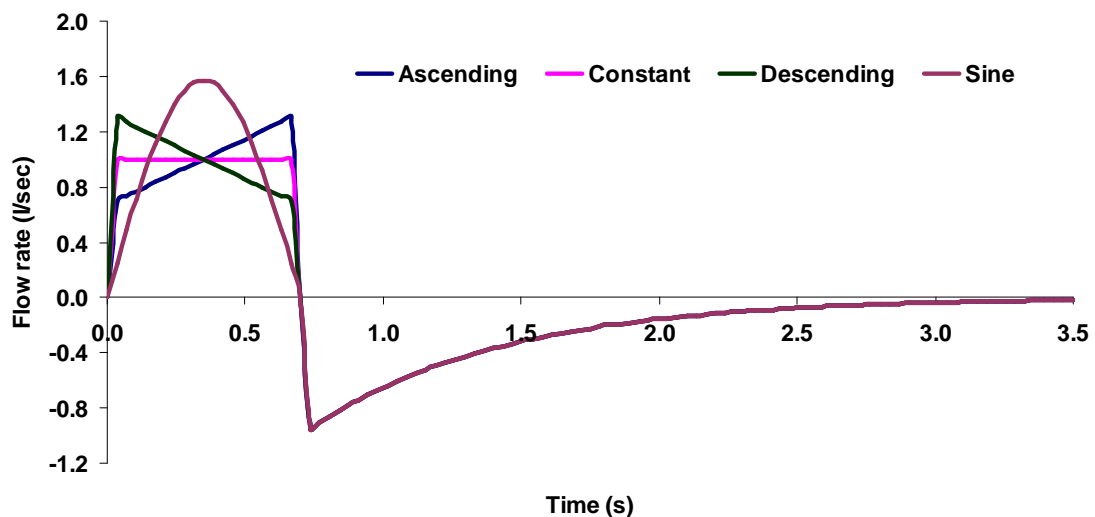
Figure 2.12 Different four flow waveforms generated from mechanical ventilator. Lung was assumed to be inflated 700 cc in 0.7-s duration
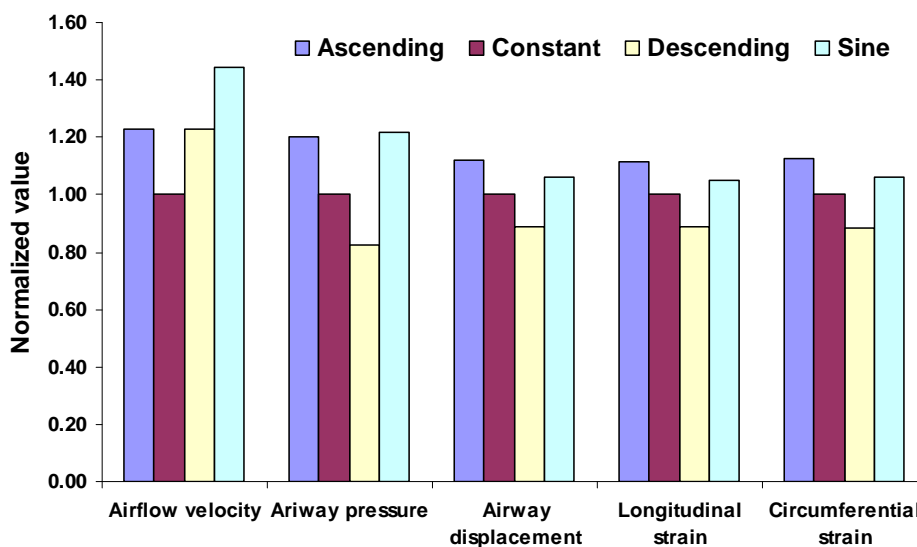
Figure 2.13 Effect of airflow waveform from mechanical ventilation on airflow velocity, airway pressure, airway displacement, longitudinal strain, and circumferential strain. The normalized values are based on constant flow waveform.

2.7.6 Effect of Tidal Volume

Three tidal volumes were employed in this analysis: 350, 700, and 1400 cc. The effect of tidal volume on airflow velocity, airway pressure, and airway strains is shown in Figure 2.14. Tidal volume did not affect a maximum airflow velocity; however, airway pressure and airway strains increased with increasing tidal volume. The maximum airway pressure increased about 24% and 47% when tidal volume increased from 350 cc to 700, and 1400 cc, respectively. The maximum airway displacement increased about 29% and 50% when tidal volume increased from 350 cc to 700, and 1400 cc, respectively. The maximum longitudinal strain increased about 28% and 57% when tidal volume increased from 350 cc to 700, and 1400 cc, respectively. The maximum circumferential strain

increased about 30% and 53% when tidal volume increased from 350 cc to 700, and 1400 cc, respectively.
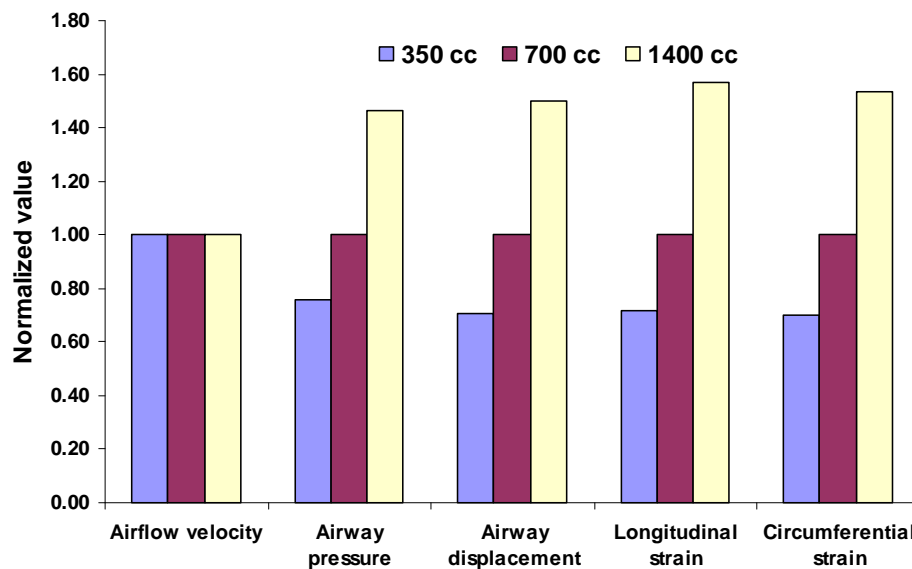
Figure 2.14   Effect of tidal volume on airflow velocity, airway pressure, airway displacement, longitudinal strain, and circumferential strain. The normalized values are based on 700-cc tidal volume.

2.7.7 Effect of Positive-End Expiratory Pressure

The effect of positive-end expiratory pressure (PEEP) on airflow velocity, airway pressure, and airway strains was investigated using 0-, 5-, and 10-hPa PEEP. As can be seen from Figure 2.15, PEEP did not affect a maximum airflow velocity. Airway pressure, airway displacement, and airway strains in creased with increasing PEEP. The maximum airway pressure increased about 12% and 32% when PEEP increased from 0 hPa to 5, and 10 hPa, respectively. The maximum airway displacement increased about

11% and 33% when PEEP increased from 0 hPa to 5, and 10 hPa, respectively. The maximum longitudinal strain increased about 16% and 40% when PEEP increased from 0 hPa to 5, and 10 hPa, respectively. The maximum circumferential strain increased about 12% and 35% when PEEP increased from 0 hPa to 5, and 10 hPa, respectively.
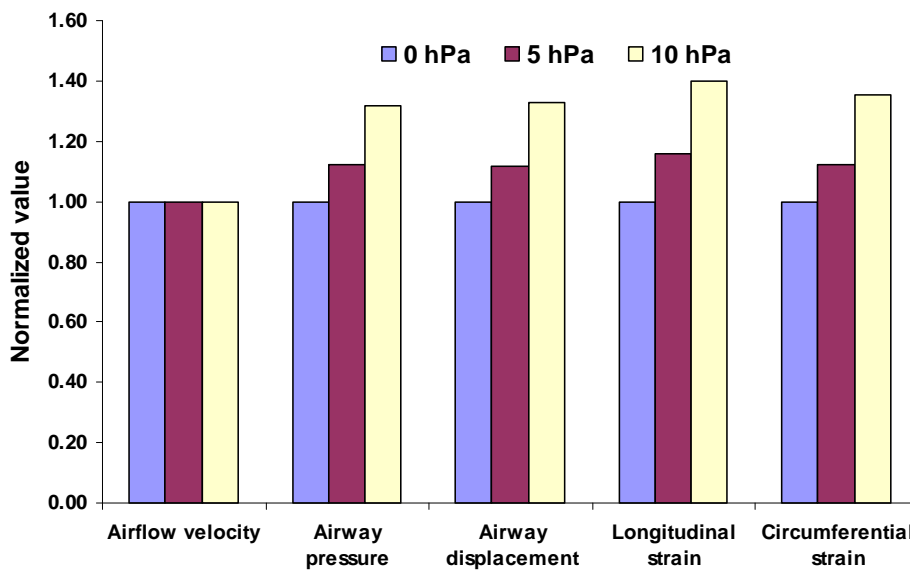
Figure 2.15   Effect of PEEP on airflow velocity, airway pressure, airway displacement, longitudinal strain, and circumferential strain. The normalized values are based on 0-hPa PEEP.

2.7.8 Effect of Airway Constriction from Airway Disease

The effect of airway constriction on airflow velocity, airway pressure, airway displacement, and airway strains was investigated using two airway diseases: tumor and asthma. The simplified spherical tumor was introduced at the bifurcation for tumor case (see Figure 2.16). The distributions of airflow velocity and airway pressure for tumor

case were quite similar to those in the normal airway. The air from airway G3 divided symmetrically into airway G4 at the tumor instead of at the bifurcation (see Figure 2.17). The maximum airway pressure was observed at the tumor instead of the bifurcation (see Figure 2.17). The distributions of the airway displacement and airway strains for the tumor airway were similar to the normal airway (see Figures 2.18 and 2.19). The parametric study was performed on tumor size and stiffness. Tumor size highly affected airflow velocity; however, it insignificantly affected airway pressure, airway displacement, longitudinal strain, and circumferential strain (see Figure 2.20). The tumor size effect on airflow velocity was significant when ratio of tumor radius to airway radius was at least 0.8. In contrast, tumor stiffness highly affected longitudinal strain but insignificantly affected airflow velocity, airway pressure, airway displacement, and circumferential strain (see Figure 2.21).
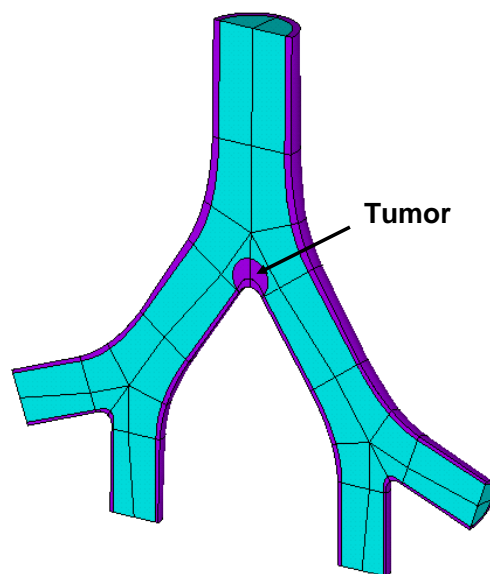
Figure 2.16   Geometric representations of the airway bifurcation generations 3 to 5 based on ICRP (1994) tracheobronchial geometry and measurement by Habib et al. (1994). The simplified spherical tumor is introduced at the first bifurcation for tumor airway analysis.
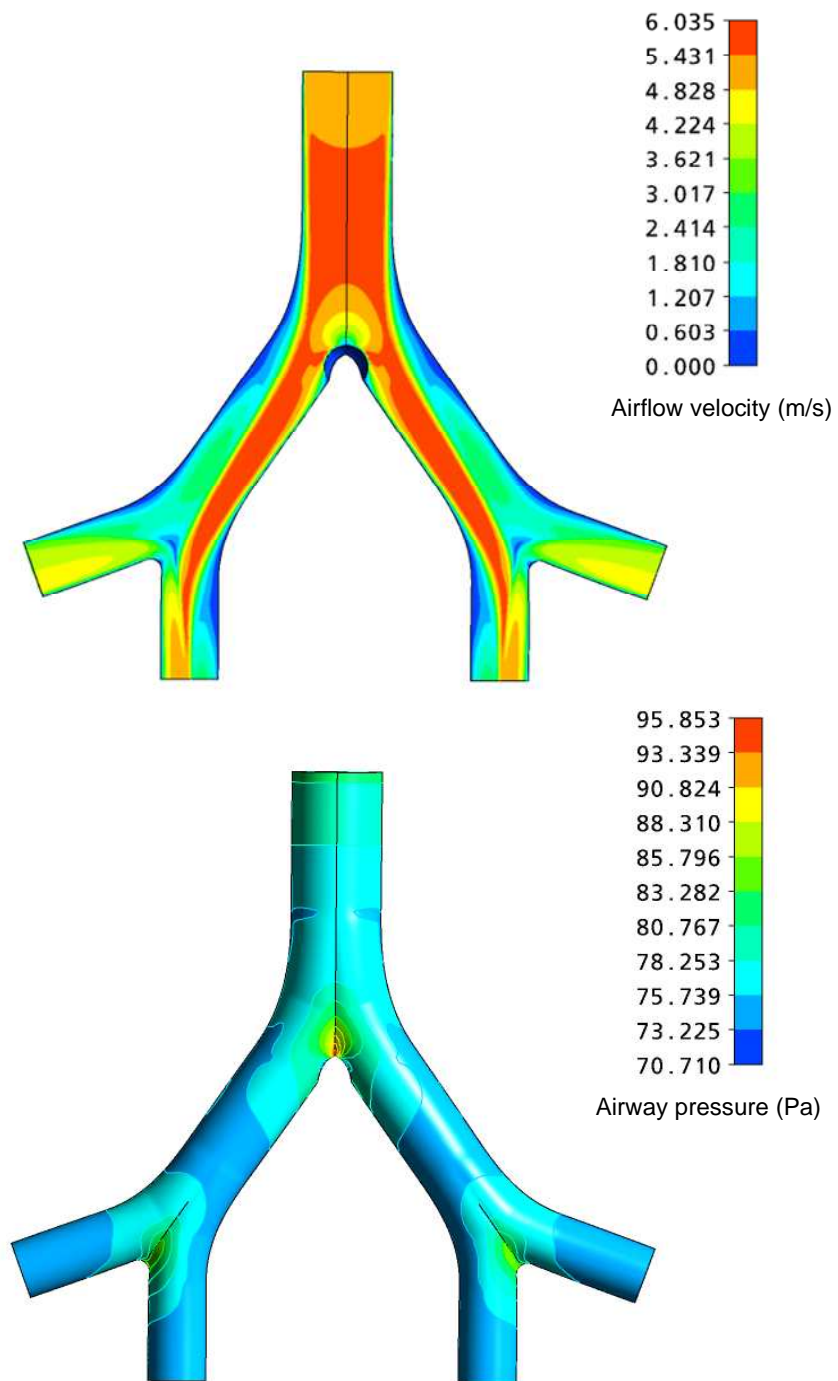
Figure 2.17 Airflow velocity (top) and airway pressure (bottom) at the end of inhalation for tumor case. Airflow rate of 60 l/min with a constant flow waveform is used for the analysis.
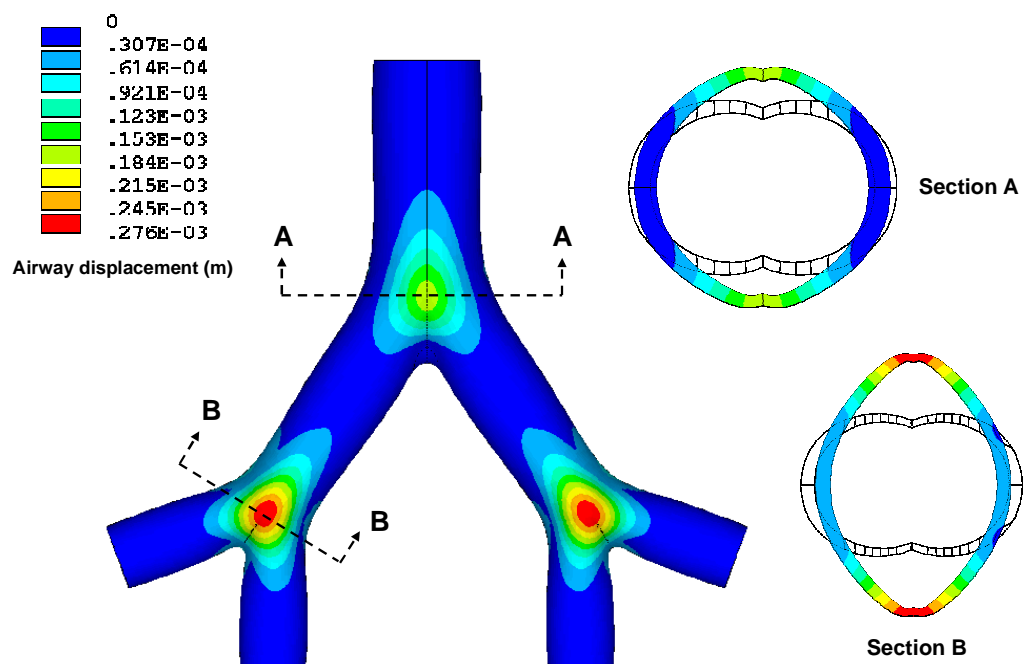
Figure 2.18 Airway displacement at the end of inhalation for tumor case. Airflow rate of 60 l/min with a constant flow waveform is used for the analysis.
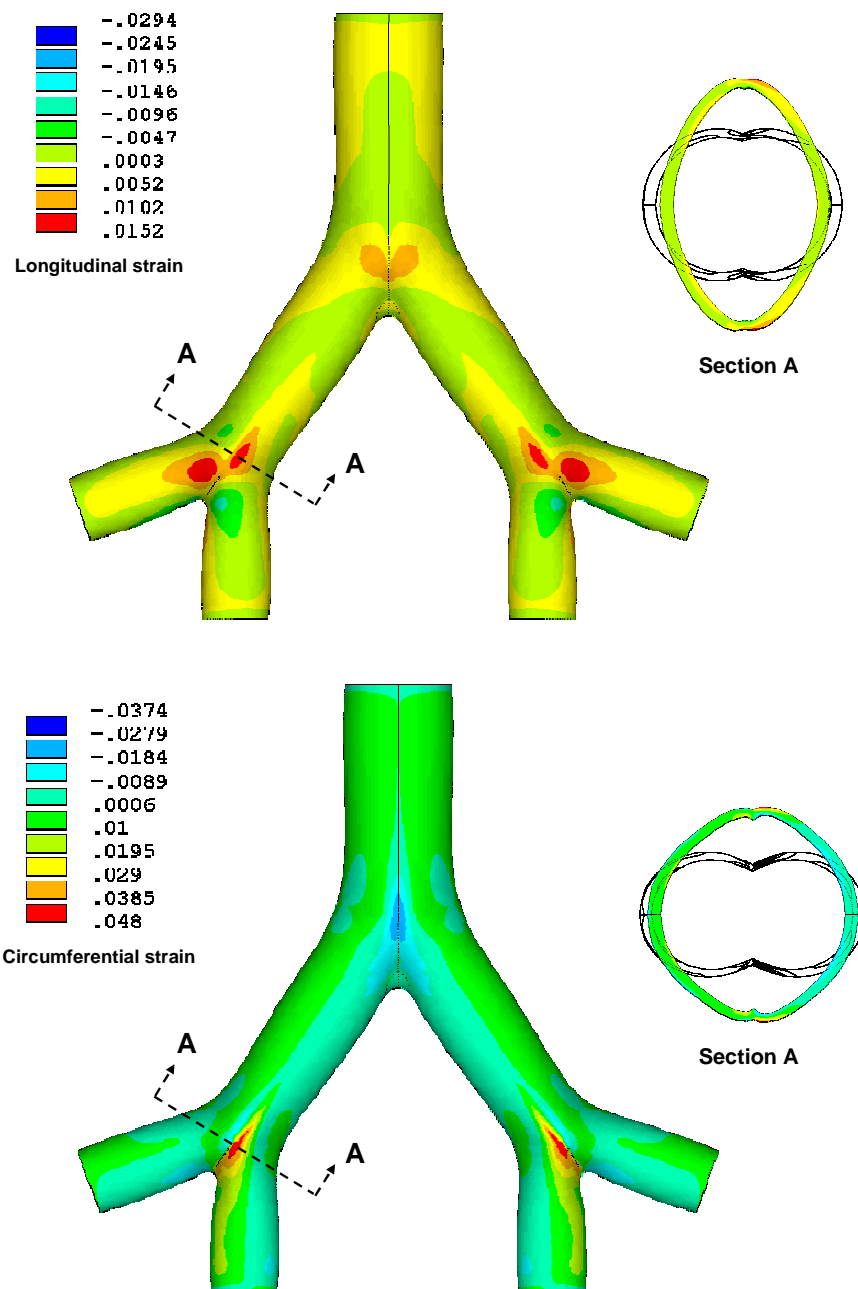
Figure 2.19   Longitudinal strain (top) and circumferential strain (bottom) at the end of inhalation for tumor case. Airflow rate of 60 l/min with a constant flow waveform is used for the analysis
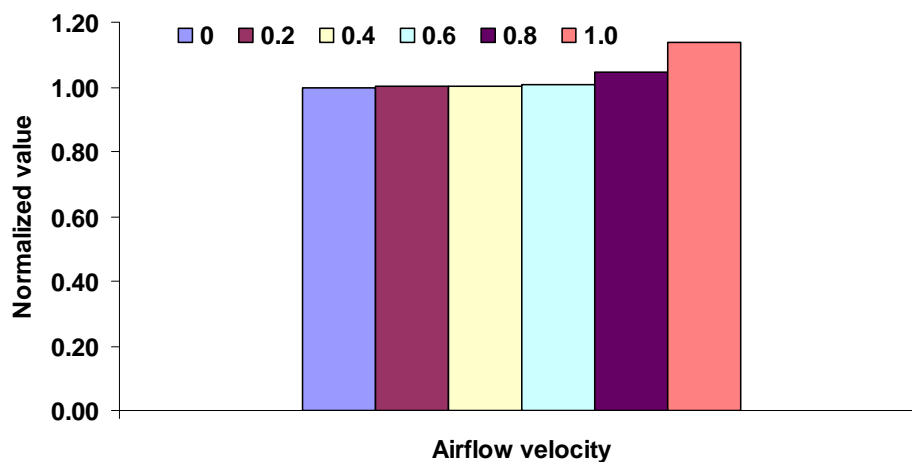
Figure 2.20   Effect of tumor size on airflow velocity. The normalized values are based on normal airway case.
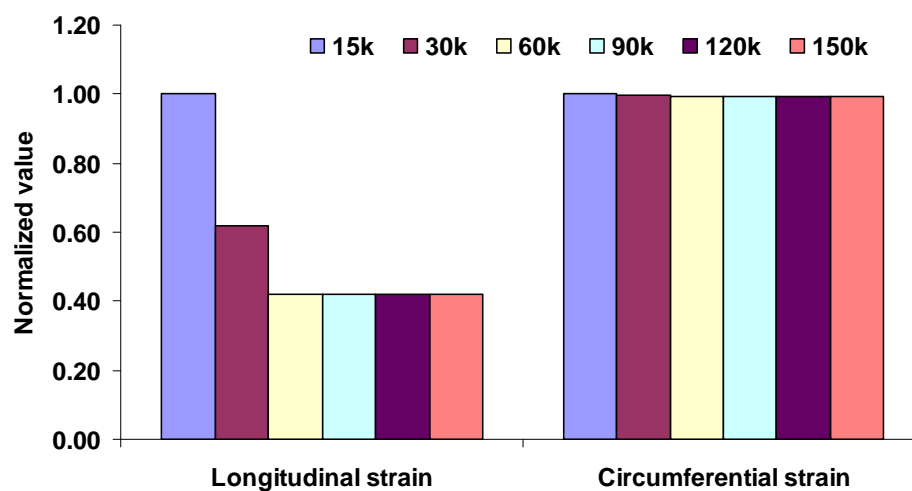
Figure 2.21   Effect of tumor stiffness on airflow velocity, airway pressure, airway displacement, longitudinal strain, and circumferential strain. The normalized values are based on normal airway case.

For asthma case, the two-time thicker airway walls than the normal airway walls was used for the analysis. Distributions of airflow velocity, airway pressure, airway

displacement, and airway strains for the asthmatic case were similar to those of the normal case. Figure 2.22 shows an effect of asthma on airflow velocity, airway pressure, airway displacement, and airway strains. The values from the asthmatic case were compared with those from 90-l/min normal case. As can be seen from Figure 2.22, the maximum airflow velocity increased about 2% and the maximum airway pressure increased about 59% for the asthmatic case. However, the maximum airway displacement, longitudinal strain, and circumferential decreased about 73%, 46%, and 43%, respectively for the asthmatic case.
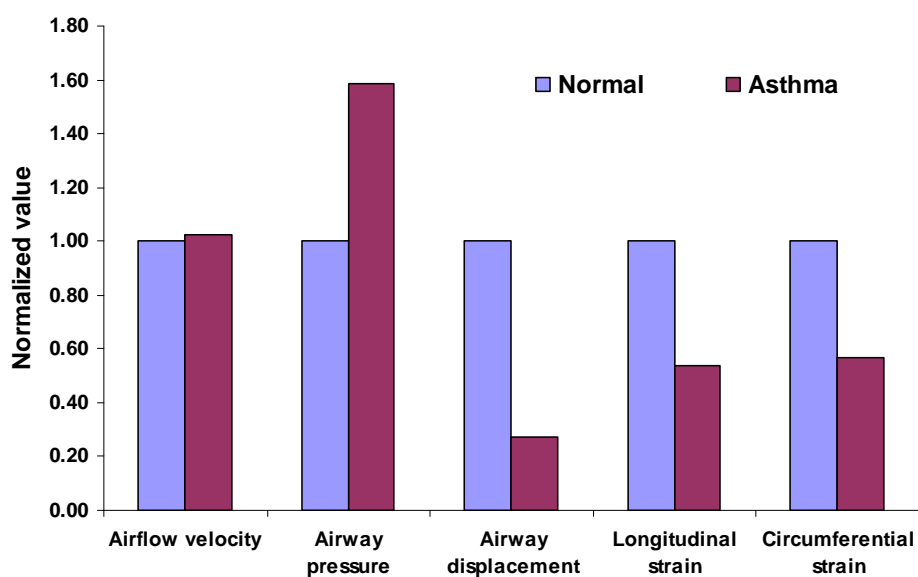
Figure 2.22   Effect of asthma on airflow velocity, airway pressure, airway displacement, longitudinal strain, and circumferential strain. The normalized values are based on normal airway case at 90-l/min constant flow rate.

2.7.9 <u>Airflow velocity, Pressure, and Strain at Alveolar-Sac Level</u>

The simplified model of the alveolar sac is shown in Figure 2.23. The simulation results at the alveolar sac were obtained through a one-way FSI algorithm. The procedure began by solving for airflow velocity and sac pressure from the fluid domain. The sac pressure was then transferred to the solid domain. The strain at the sac was then calculated using the sac pressure from the fluid domain as an external force. Airflow velocity, sac pressure, and sac strain distributions for all tidal volumes were similar. For brevity, results of the 60-l/min constant flow rate with 700-cc tidal volume were shown here. Distributions of airflow velocity and sac pressure at the end of inhalation are shown in Figure 2.24. The maximum airflow velocity was observed at the beginning of the sac. It is 0.0052 m/s. The airflow velocity is low near the sac wall. The sac pressure was similar in every location of the sac. This pressure was 28.17 Pa. The displacement distributions in the alveolar sac are shown in Figure 2.25. The pressure in the sac expanded the sac about 10% during the inhalation. The 1st, 2nd, and 3rd principal strains were uniformly distributed throughout the sac (see Figures 2.26-2.28). The maximum principal strains were 12%, 10%, and 22% for the 1st, 2nd, and 3rd principal strains, respectively. The maximum von Mises strain in the sac was about 27% (see Figure 2.29). The von Mises strain is the average strain in the sac and can be calculated using the 1st, 2nd, and 3rd principal strains (Dowling, 1998).
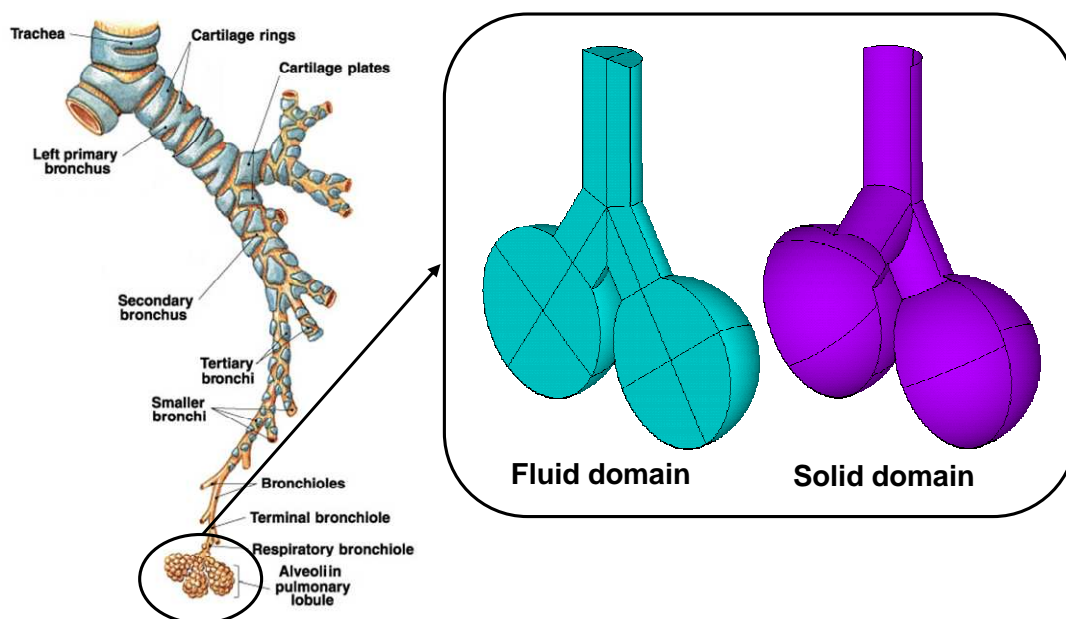
Figure 2.23   Geometric representations of the alveolar sac used for the analysis of airflow velocity, airway pressure, and airway strain.
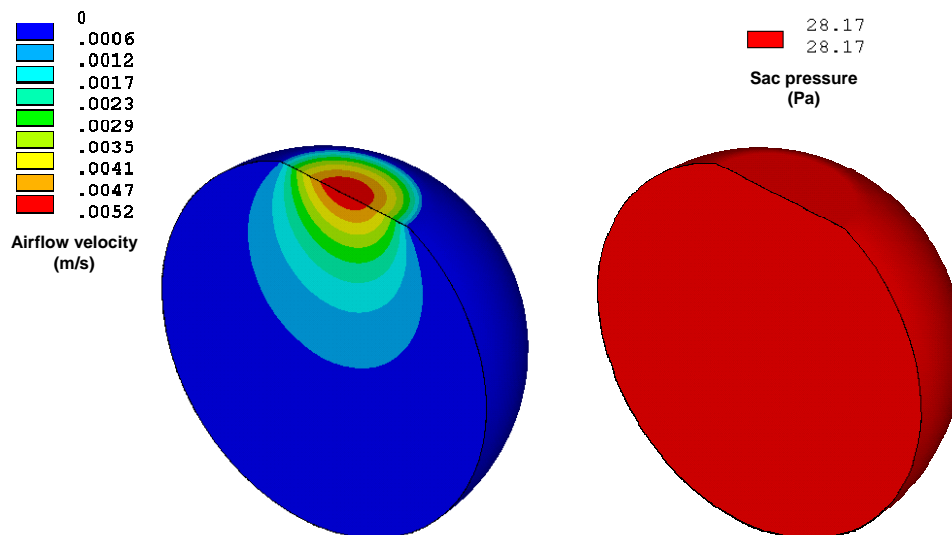
Figure 2.24   Airflow velocity (left) and airway pressure (right) in the alveolar sac at the end of inhalation for airflow rates of 60 l/min with a constant flow waveform
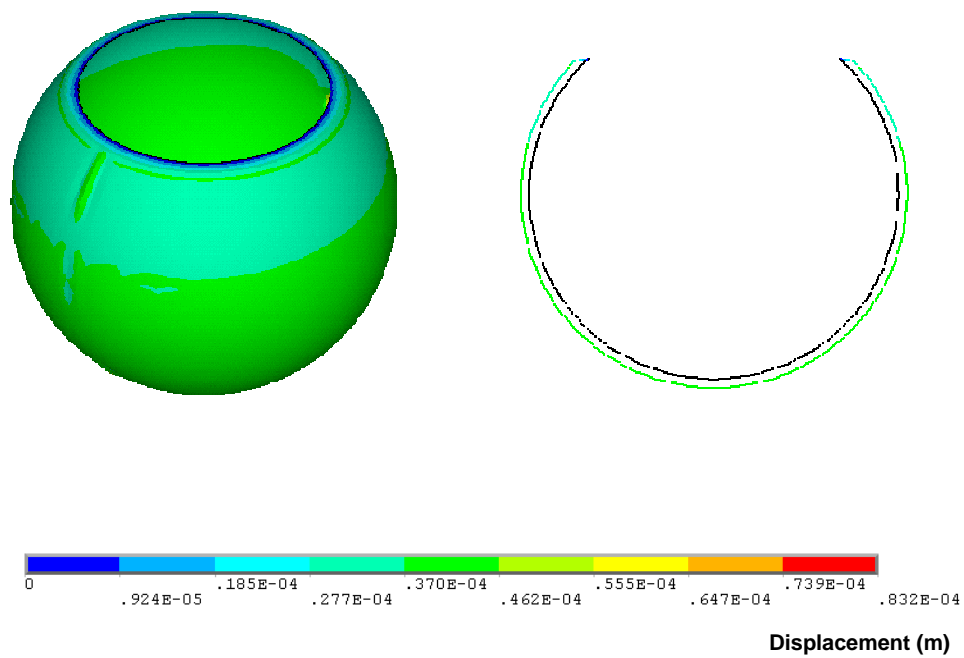
Figure 2.25   Displacement in the alveolar sac at the end of inhalation for airflow rates of 60 l/min with a constant flow waveform
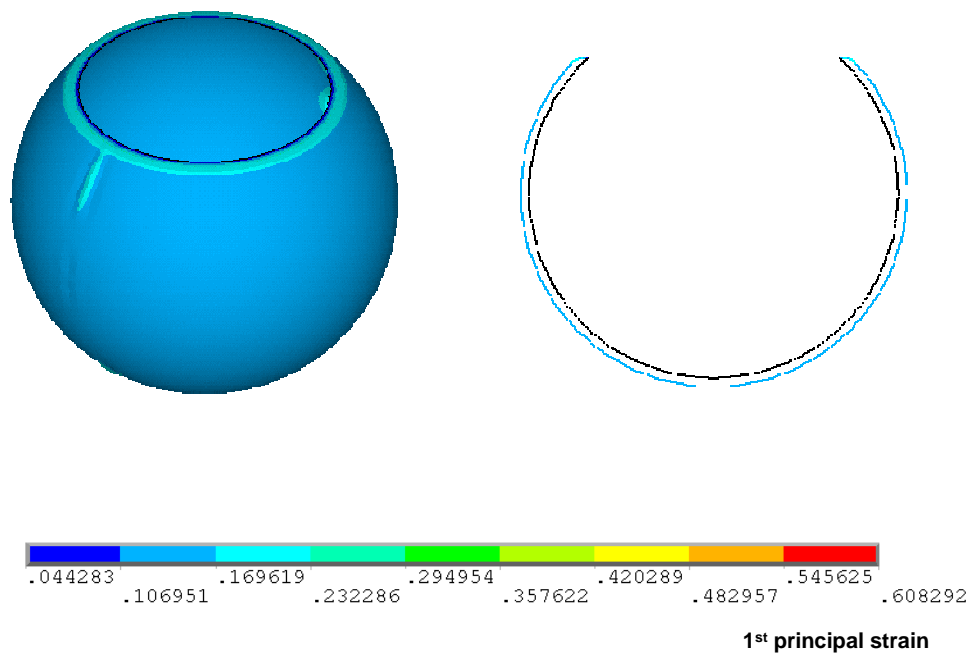
Figure 2.26   1st principal strain in the alveolar sac at the end of inhalation for airflow rates of 60 l/min with a constant flow waveform

| -.093591 | | -.006044 | | .081504 | | .169051 | | .256599 | |
| | -.049817 | | .03773 | | .125277 | | .212825 | | .300372 |

2nd principal strain
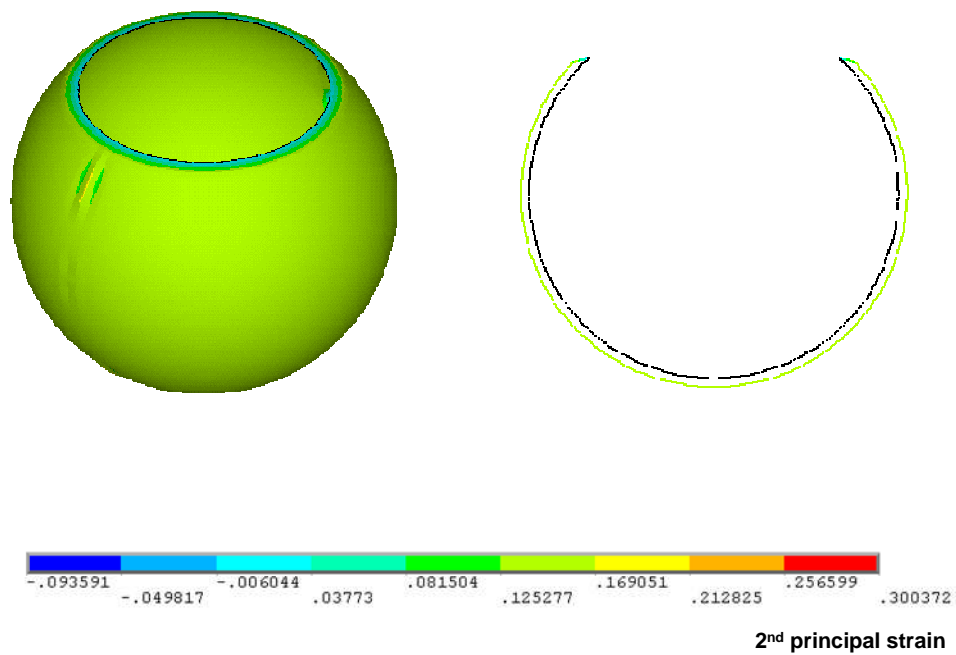
Figure 2.27   2nd principal strain in the alveolar sac at the end of inhalation for airflow rates of 60 l/min with a constant flow waveform

| -.615946 | | -.486863 | | -.357779 | | -.228696 | | -.099613 | |
| | -.551404 | | -.422321 | | -.293238 | | -.164154 | | -.035071 |

3rd principal strain
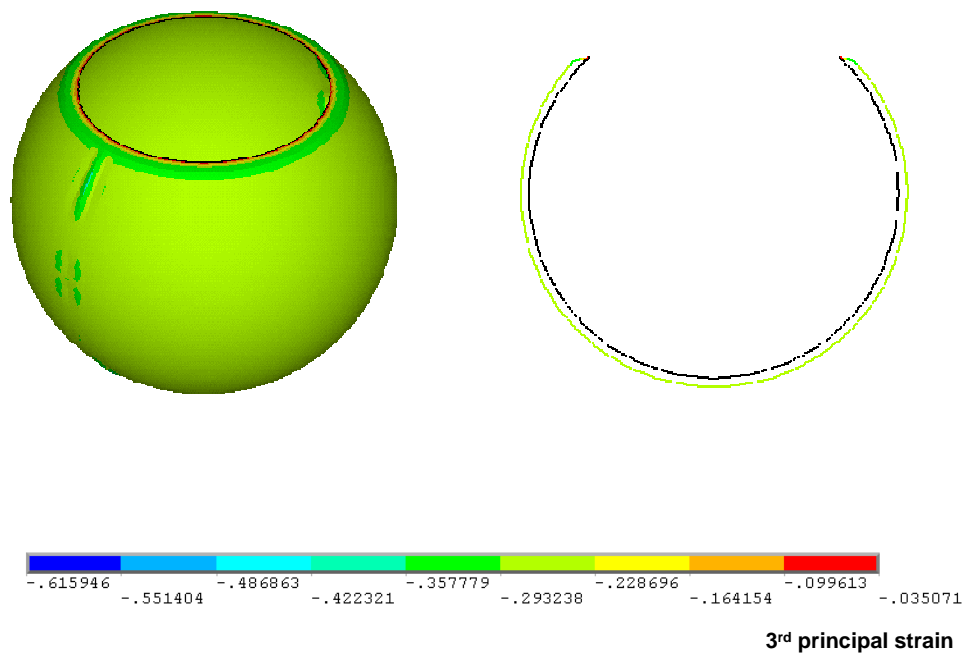
Figure 2.28   3rd principal strain in the alveolar sac at the end of inhalation for airflow rates of 60 l/min with a constant flow waveform
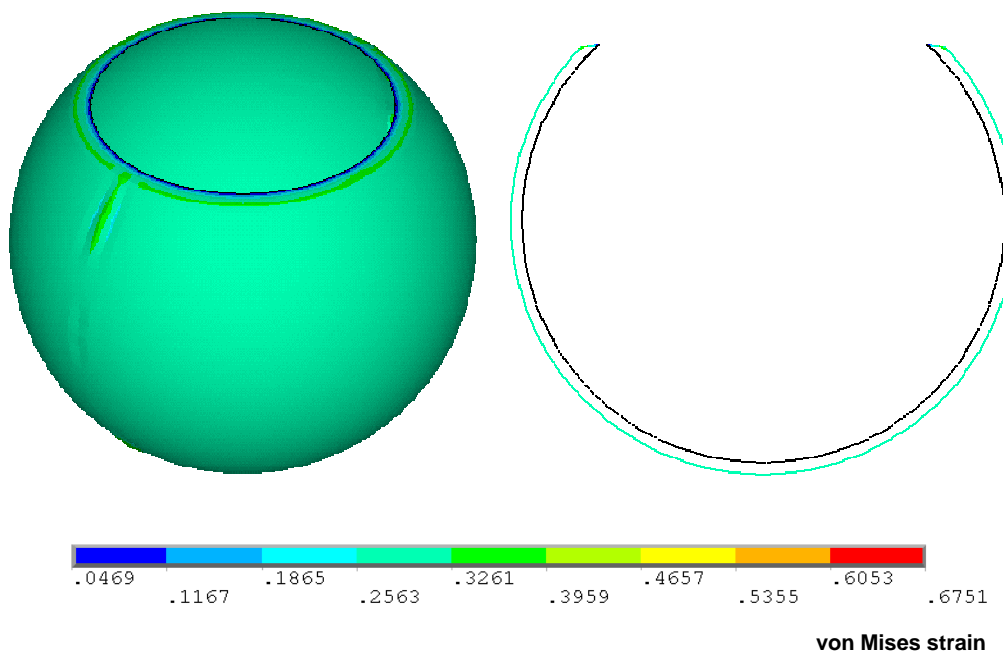
Figure 2.29   von Mises strain in the alveolar sac at the end of inhalation for airflow rates of 60 l/min with a constant flow waveform

Figure 2.30 shows an effect of tidal volume on airflow velocity, sac pressure, and sac strains. Tidal volume did not affect a maximum airflow velocity in the alveolar sac; however, it highly affected a maximum sac pressure and sac strain. The maximum sac pressure and sac strain increased two times when tidal volume increased from 700 cc to 1400 cc and the maximum sac pressure decreased two times when tidal volume decreased from 700 cc to 350 cc.
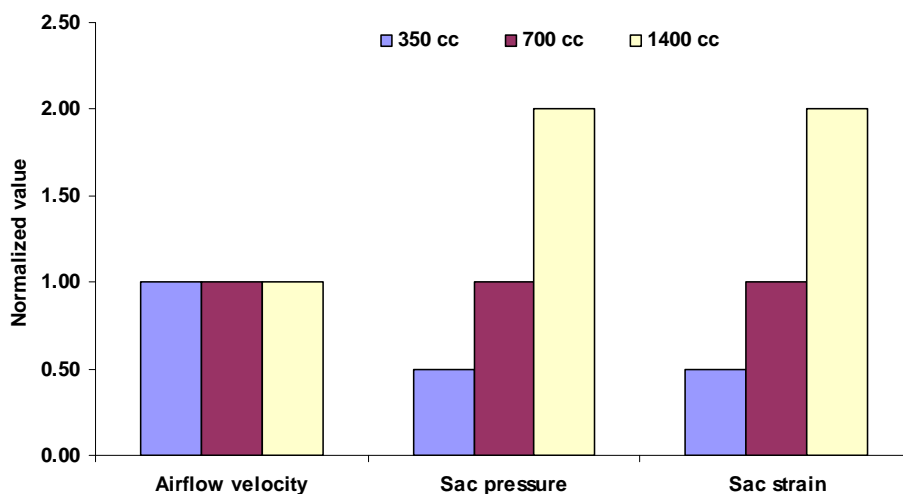
Figure 2.30   Effect of tidal volume on airflow velocity, sac pressure, and sac strain in the alveolar sac. The normalized values are based on 700-cc tidal volume.

2.8 Discussion

It would be difficult and potentially dangerous to perform experiments in patients to investigate an effect of mechanical ventilation parameters on airway pressure and airway strains during mechanical ventilation by attempting to directly measure these strains. A computational model of the respiratory airway based on FSI algorithm was constructed and used to predict the effect of each ventilation parameter on the airway pressure and airway strains during the mechanical ventilation.

Airway pressure increased with increasing airflow rate, tidal volume, and PEEP. It also increased in the asthmatic airway. Increase in airway pressure can trigger inflammatory mediators (Dhanireddy et al., 2006; Goldstein et al., 2001; Ranieri et al., 1999). The overproduction of cytokines can exacerbate lung injury and could lead to an

increased mortality of patient with ALI or ARDS. Pressures in the airways can be transmitted throughout the whole lung via the lung fiber system. If this transmitted pressure is very high, it can cause a mechanical rupture of the lung fiber network especially in diseased regions as may occur with emphysema. This high pressure at the airway walls also causes a mechanical rupture at alveolar ducts since the axial fibers run from the branching airways to the alveolar structures (Gattinoni et al., 2003).

For the airway bifurcation generations 3 to 5 considered, the airways expanded in both circumferential and longitudinal directions, even though the airway pressure only acts in the circumferential direction. The airways expanded more circumferentially rather than longitudinally during the active inhalation as expected and recently found experimentally in small intact animal models (Sinclair et al., 2007) which utilized microfocal X-ray imaging to obtain real-time bronchograms under various mechanical ventilation conditions. The strain levels from the organ-level model of the airway generation 3 to 5 were in good agreement the experiment in small intact animal models by Sinclair et al (2007). The airway strains increased with increasing airflow rate, tidal volume, and PEEP form mechanical ventilation. However, they decreased for the asthmatic airway. This decrease in the airway strains for the asthmatic airway was observed in many clinical studies (Brackel et al., 2000; Brown et al., 2007) because of the stiff asthmatic airway.

Results of the 1st and 2nd principal strains are very close and these strains may represent the diameter change of the sac. The 3rd principal strain may be related to thickness change. The values of the 1st and 2nd principal strains were in good agreement

with the change in the sac diameter calculated from the sac displacement and they also are in the same range as the previous experiment in small intact animal models by Sinclair et al (2007). These strain levels in the sac increased with increasing tidal volume.

High strain levels in the airway can induce inflammatory responses through releasing interleukin (IL)-8, the most powerful chemoattractant for neutrophils. A study by Belperio et al (2002) showed that high peak airway pressure and strain during mechanical ventilation increased CXC2 chemokine (a murine equivalent of IL-8) without cell injury. The increase in CXC2 chemokine was associated with neutrophil activation and lung injury. In addition, increase in airway strain from high tidal volume increased cytokine tumor necrosis factor-alpha (TNFα) level (Chiumello et al., 1999; Tremblay et al., 1997). The organ-level model developed in this chapter could provide useful information about how each mechanical ventilation parameters affects the strain levels in the airways and the alveolar sac so that physicians can adjust each parameter appropriately during mechanical ventilation.

2.9 Summary

The organ-level model that incorporates the interactions between airflow and the airway wall of the airway generation 3 to 5 was developed to study airflow velocity, airway pressure, airway displacement, and airway strains during mechanical ventilation. The effect of airflow rate, airflow waveform, tidal volume, PEEP, and airway constriction on each parameter was investigated. The simulation results showed that airflow velocity

increased with increasing airflow rate and airway constriction. Airway pressure increased with increasing airflow rate, tidal volume, and PEEP. Airway displacement and airway strains increased with increasing airflow rate, tidal volume, and PEEP form mechanical ventilation; however they decreased in airway constriction from asthma. Sine waveform provided the highest airflow velocity and airway pressure while descending waveform provided the lowest airway pressure, airway displacement and airway strains. The airway displacement from the organ-level model is transferred to the tissue-level model for studying strain distributions in each airway layer. Details of the tissue-level model will be discussed in the next chapter.

CHAPTER 3 Tissue-Level Models

3.1 Introduction

Airways are of heterogeneous material and composed of many layers, such as mucosa, submucosa, lamina propria, and adventitia (Bai et al., 1994). Stiffness in each airway layer also varies (Kamm, 1999). Many *in vitro* and *in vivo* models have been developed to study the effects of mechanical force or pressure on the airways. These models include the cultured airway epithelial cells which were in contact with the cultured fibroblasts via a soluble mediator (Swartz et al., 2001) or fibroblasts suspended in a collagen matrix and bronchial epithelial cells (Choe et al., 2003). However, there are some flaws in their models. First, the mechanical force they used did not represent the actual force during mechanical ventilation. Second, their model fails to describe the distributions of stresses and strains in each layer of the airway. Since it is very difficult to measure the distributions of stresses and strains in real tissue due to thickness of each layer in the airways is very thin, the computational model that incorporates the heterogeneity of the airways could be very helpful to understand how stresses and strains distribute in each airway layer during mechanical ventilation.

In this chapter, the continuum model that incorporates the heterogeneity of the airways is developed to study the effects of airway material properties on distributions of strain in each layer of the airway wall. The detailed geometry and the computational method for the tissue-level model are also discussed.

3.2 Airway Architecture

Based on a recent publication by Bai et al. (1994), airway can be divided into three major layers (mucosa, submucosa, and area outside submocosa) due to their distinct composition in each layer and mechanisms that each layer can be thickened. The mucosa consists of epithelium, basement membrane, and lamina propria. The submucosa begins at the outer border of the lamina propria and this region includes the smooth muscle tissue. The area outside the submucosa consists of cartilage-fibrous layer and adventitia. Adventitia is referred to the loose connective tissue that ties the airways to the surrounding environment. Figure 3.1 shows a schematic diagram of airway architecture along the thickness of the bronchial wall.
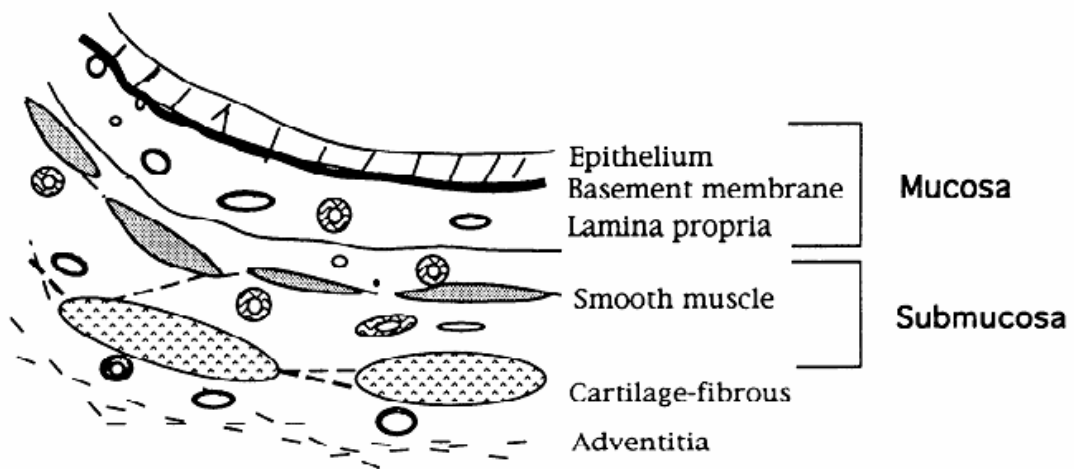
Figure 3.1   A schematic diagram of airway architecture along the thickness of the bronchial wall. Image is from Bai et al. (1994)

3.3 Governing Equations and Computational Method

The governing equations for strain distributions in each layer of the airway wall during mechanical ventilation are the steady state structural equations and are described below using Einstein's repeated index convention (Reddy, 1993).

Equation of motion

$$\frac{\partial \sigma_{ij}}{\partial x_j} + F_i = 0 \qquad\qquad (6)$$

Constitutive relations

$$\sigma_{ij} = C_{ijkl}\varepsilon_{kl} \qquad\qquad\qquad (7)$$

In the equation above, σ is the stress in each direction, F is the body force, ρ is density, C is the elasticity tensor, and ε is the strain in each direction. The finite element method is chosen to solve these governing equations employing the commercial finite element software, ANSYS.

3.4 Computational Models and Boundary Conditions

A tissue-level model of the airway wall is developed treating the airway wall as a composite material. Figure 3.2 shows airway architecture along the thickness of the bronchial wall and the corresponding computation domain. The computational domain of the airway tissue is constructed in the finite element software, ANSYS. Solid elements, BRICK45 (ANSYS, 2005), are used to represent each layer of the airway tissue. Each layer of the airway tissue is assumed to be perfectly bonded to other layers. The material properties for each layer are tabulated in Table 3.1. Thickness of each layer is obtained from the histological section of airway tissue (Benayoun et al., 2003) and it is 240, 115, and 55 μm for mucosa, smooth muscle, and cartilage layer, respectively.
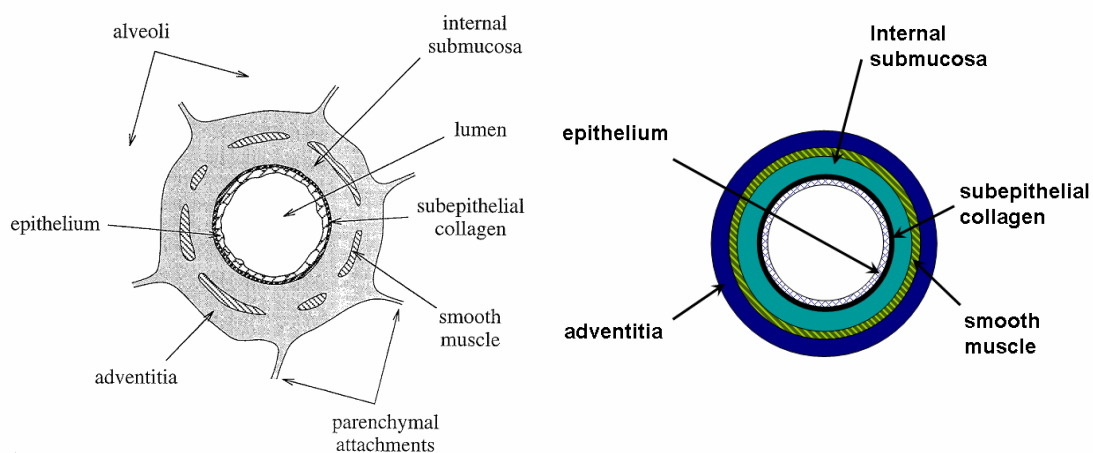
Figure 3.2   Image from Kamm (1999) showing different layers of the airway wall architecture (left) and the computational model of the airway wall for the tissue-level model (right)

Table 3.1   Material properties of each layer in the airway wall

Airway wall layer	Young's modulus (kPa)	
Mucosa (Yamada, 1970)	Circumferential	80
	Longitudinal	150
Smooth muscle with cartilage (Jiang and Stephens, 1990)	Circumferential	75
	Longitudinal	75

The boundary conditions for the tissue-level model are airway displacements at each location from the organ-level model. At least three elements are used in thickness direction of each layer to make sure that strain variations in thickness direction can be

captured. Figure 3.3 shows the computational domain of the tissue-level model and the

finite element model as well as all boundary conditions for the tissue-level model.
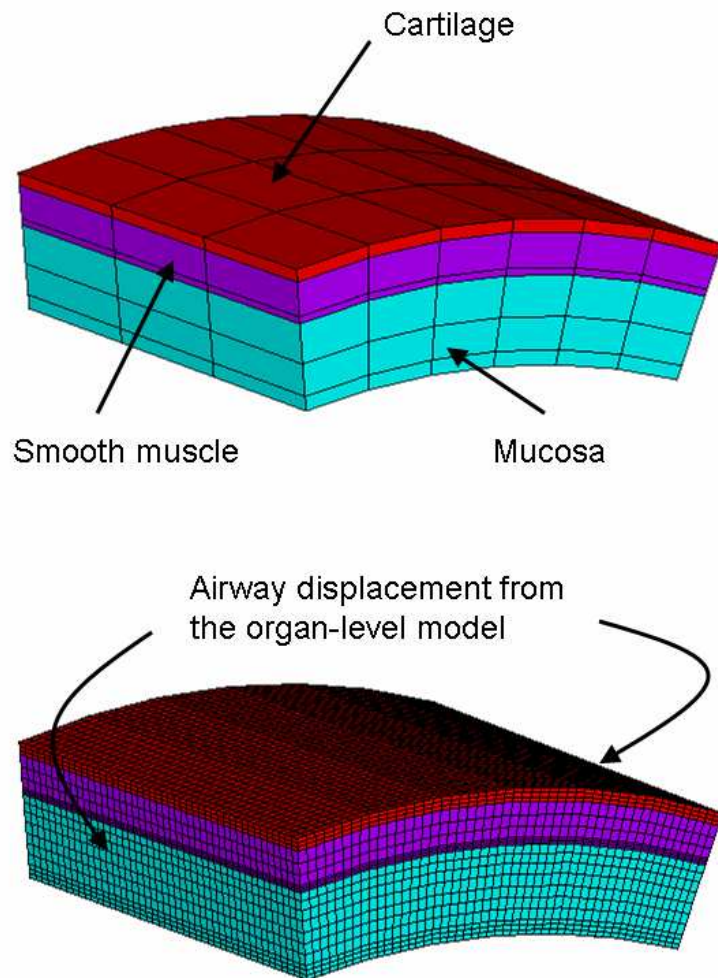
Figure 3.3   The computational model of the tissue-level model (top) and the finite
element model as well as all boundary conditions for the tissue-level model (bottom)

3.5 Model Validation

A review of the literature indicates that there is no information of strain distributions in each airway layer during mechanical ventilation. Therefore, a mesh-independence study is performed to confirm that a fine enough element had been used to represent the computational domain. Changes in displacement and von Mises strain are used as convergence criteria. A converged model is obtained when changes in those criteria are less than 5%.

3.6 Method of Analysis

The effect of material properties on the strain distributions in each layer was investigated using two material models: heterogeneous and homogeneous material model. The material properties of each layer in Table 3.1 were used for the heterogeneous material model. In contrast, the material properties from the organ-level model were used for all airway tissue layers in the homogeneous material model. The tissue geometry was obtained from the center of the airway generation 4. The displacements at the end of inhalation for 60-l/min constant flow waveform were chosen for the analysis (see Figure 3.4). The analysis was performed to study distributions of von Mises strain, normal strain, and shear strain in each airway layer. The von Mises strain is an average strain at any point. It is a combination of normal and shear strain in all directions (Dowling, 1998).

Organ-level model

Airway displacement = 2.77e-5 m

Tissue-level model

Airway displacement = 1.32e-5 m
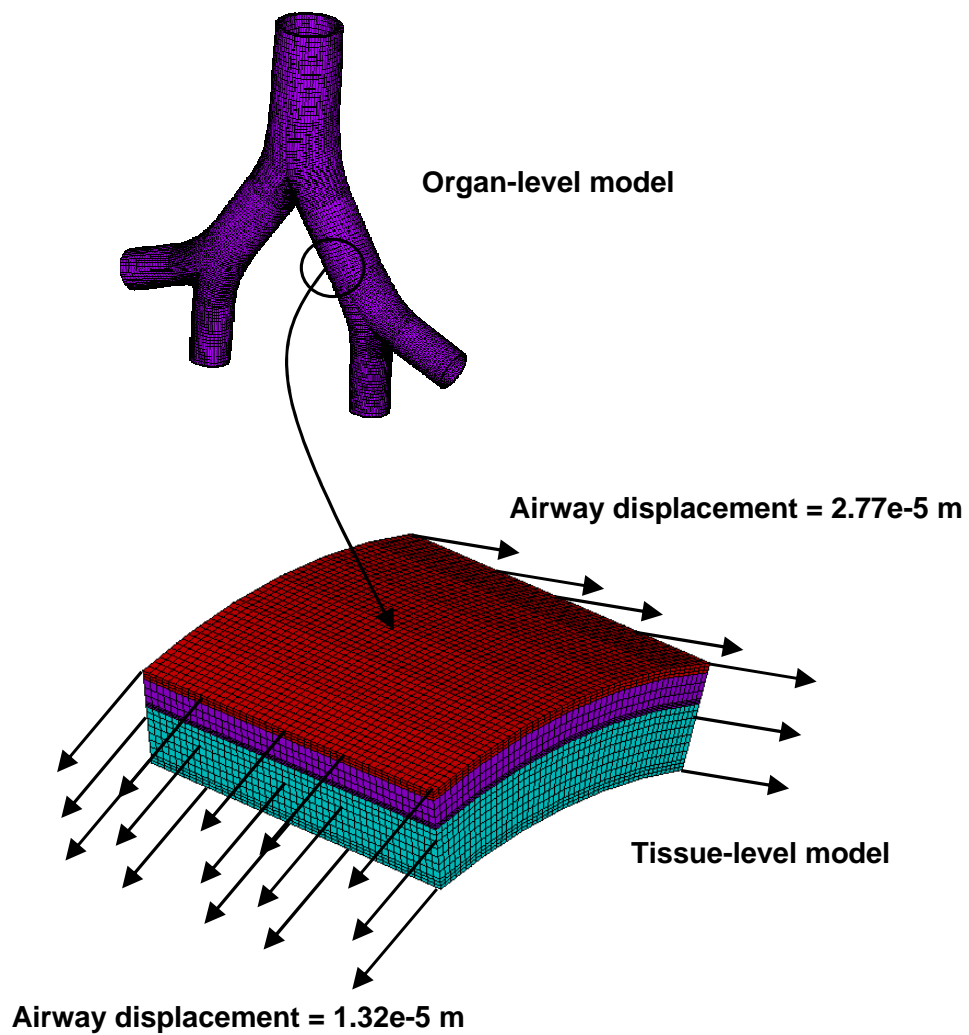
Figure 3.4   The finite element model of for the tissue-level model and boundary conditions that was used for the analysis. The airway displacements used in the analysis were from airway displacement at the organ-level at the end of inhalation with 60-l/min constant flow waveform.

3.7 Results

3.7.1 Derivation of Material Properties for the Organ-Level Model

Material properties of the homogeneous airway wall at the organ-level model can be calculated using material properties of each tissue layer and a composite-material theory (Barbero, 1999).

$$E = V_{mu\cos a} E_{mu\cos a} + V_{SM} E_{SM} + V_{cartilage} E_{cartilage} \qquad (8)$$

In the above equation, E is a Young's modulus of elasticity of the homogeneous airway wall, $E_{mu\cos a}$ is a Young's modulus of elasticity of the mucosa, E_{SM} is a Young's modulus of elasticity of the smooth muscle, $E_{cartilage}$ is a Young's modulus of elasticity of the cartilage, $V_{mu\cos a}$ is a volume fraction of the mucosa, V_{SM} is a volume fraction of the smooth muscle, and $V_{cartilage}$ is a volume fraction of the cartilage. The volume fraction of each layer is a ratio of the thickness in each layer to total thickness of the airway tissue.

Substituting values of the Young's modulus of elasticity and the volume fraction for each layer into (8), we obtain

In a circumferential direction

$$E = \frac{240}{410}(80) + \frac{115}{410}(75) + \frac{55}{410}(75) = 78 \quad kPa$$

In a longitudinal direction

$$E = \frac{240}{410}(150) + \frac{115}{410}(75) + \frac{55}{410}(75) = 120 \quad kPa$$

As can be seen, material properties calculated from the composite-material theory were in good agreement with material properties at the organ-level model calculated from the stress-strain curve of the whole airways.

3.7.2 Strain Distributions in Each Airway Layer

The effect of material properties on the strain distributions in each layer was investigated using two material models: heterogeneous and homogeneous. The von Mises strain distributions in the mucosa layer for both models are shown in Figure 3.5. As can be seen from this figure, the distributions of von Mises strain in the mucosa layer for both material models were different. High von Mises strain areas from the heterogeneous model were smaller than those from the homogeneous model. The maximum von Mises strain in the mucosa layer from the heterogeneous model was lower than that for the homogeneous model since the mucosa layer in the heterogeneous model is stiffer than that in the homogeneous model. This maximum was 1.8% and 2.0% for the heterogeneous model and homogeneous model, respectively.

Heterogeneous model

.0003
.0025
.0048
.007
.0092
.0115
.0137
.016
.0182
.0204

Mucosa strain
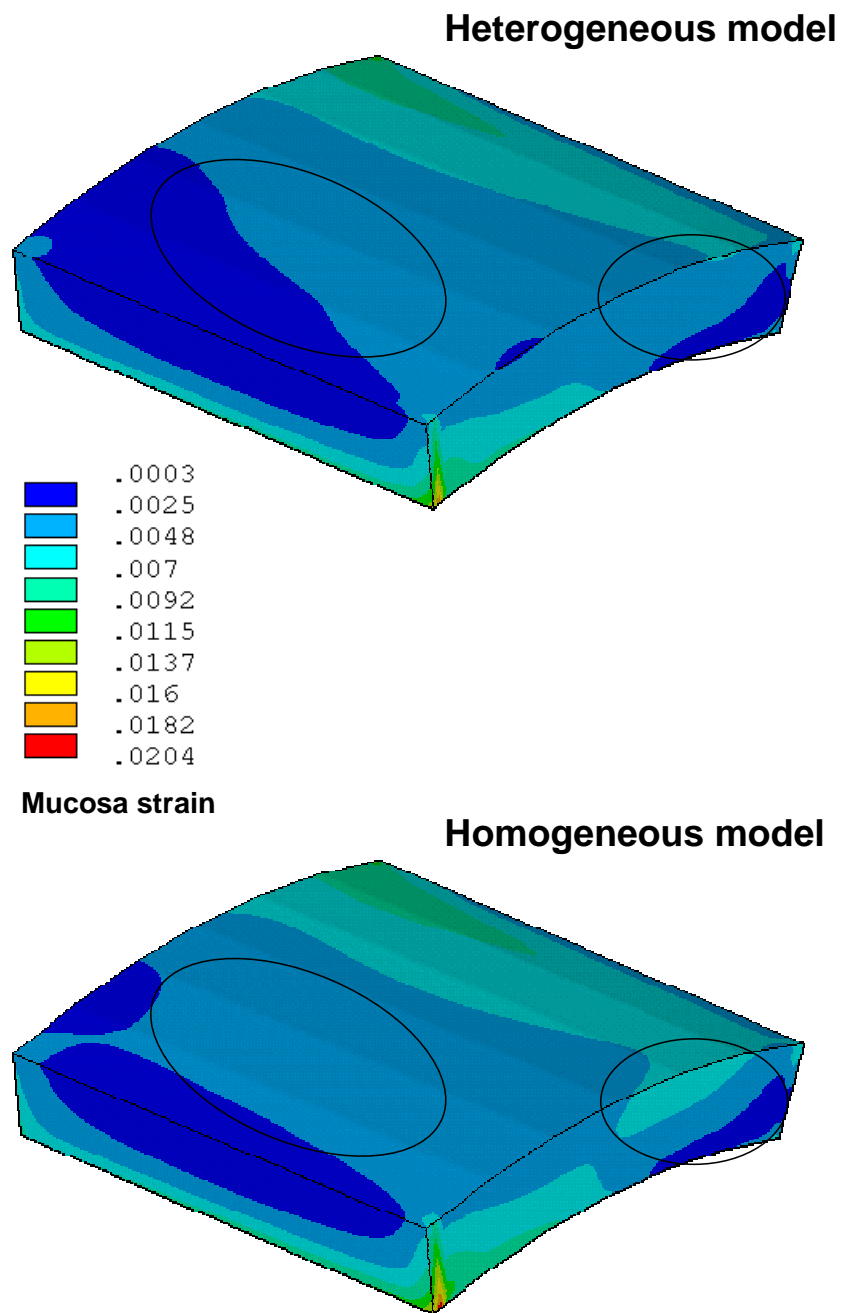
Homogeneous model

Figure 3.5   von Mises strain distributions in the mucosa layer for the heterogeneous model (top) and homogeneous model (bottom). Circles indicate the difference in the strain distributions.

The maximum von Mises strain in the smooth muscle layer from the heterogeneous model was greater than that for the homogeneous model since the smooth muscle layer in the heterogeneous model is less stiff than that in the homogeneous model. This maximum was 2.5% and 2.2% for the heterogeneous model and homogeneous model, respectively. The distributions of von Mises strain in the smooth muscle layer for both models were also different. High von Mises strain areas from the heterogeneous model were bigger than those from the homogeneous model (see Figure 3.6). The von Mises strain distributions in the cartilage layer for both models are shown in Figure 3.7. The maximum von Mises strain in the cartilage layer from the heterogeneous model was greater than that for the homogeneous model since the cartilage layer in the heterogeneous model is less stiff than that in the homogeneous model. This maximum was 3.7% and 3.1% for the heterogeneous model and homogeneous model, respectively. The distributions of von Mises strain in the cartilage layer from both models were also different. High von Mises strain areas from the heterogeneous model were bigger than those from the homogeneous model.

Heterogeneous model

.0002
.003
.0058
.0086
.0114
.0142
.017
.0198
.0226
.0254

Smooth muscle strain
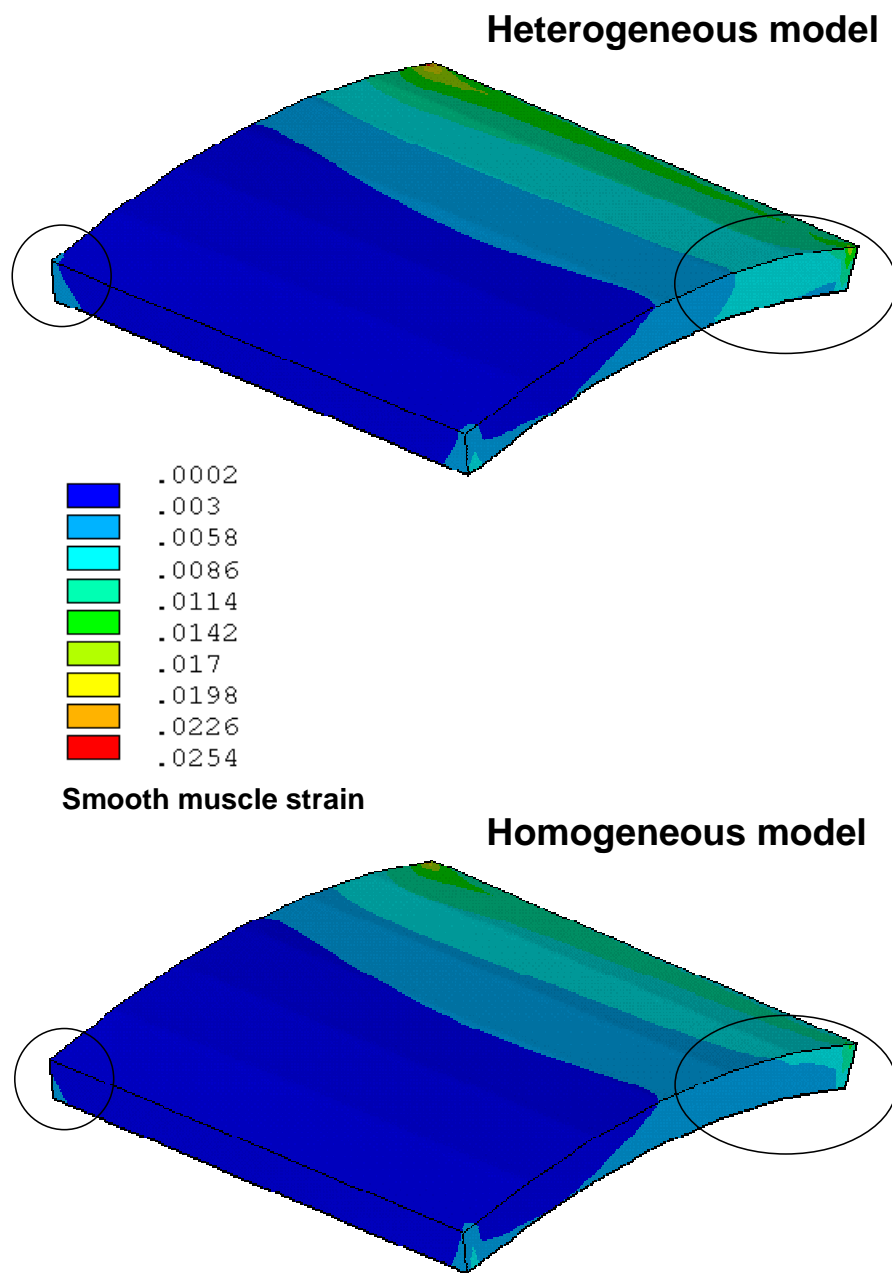
Homogeneous model

Figure 3.6   von Mises strain distributions in the smooth muscle layer for the heterogeneous model (top) and homogeneous model (bottom). Circle indicates the difference in the strain distributions.

Heterogeneous model

.0001
.0042
.0083
.0124
.0165
.0206
.0247
.0288
.0328
.0369

Cartilage strain
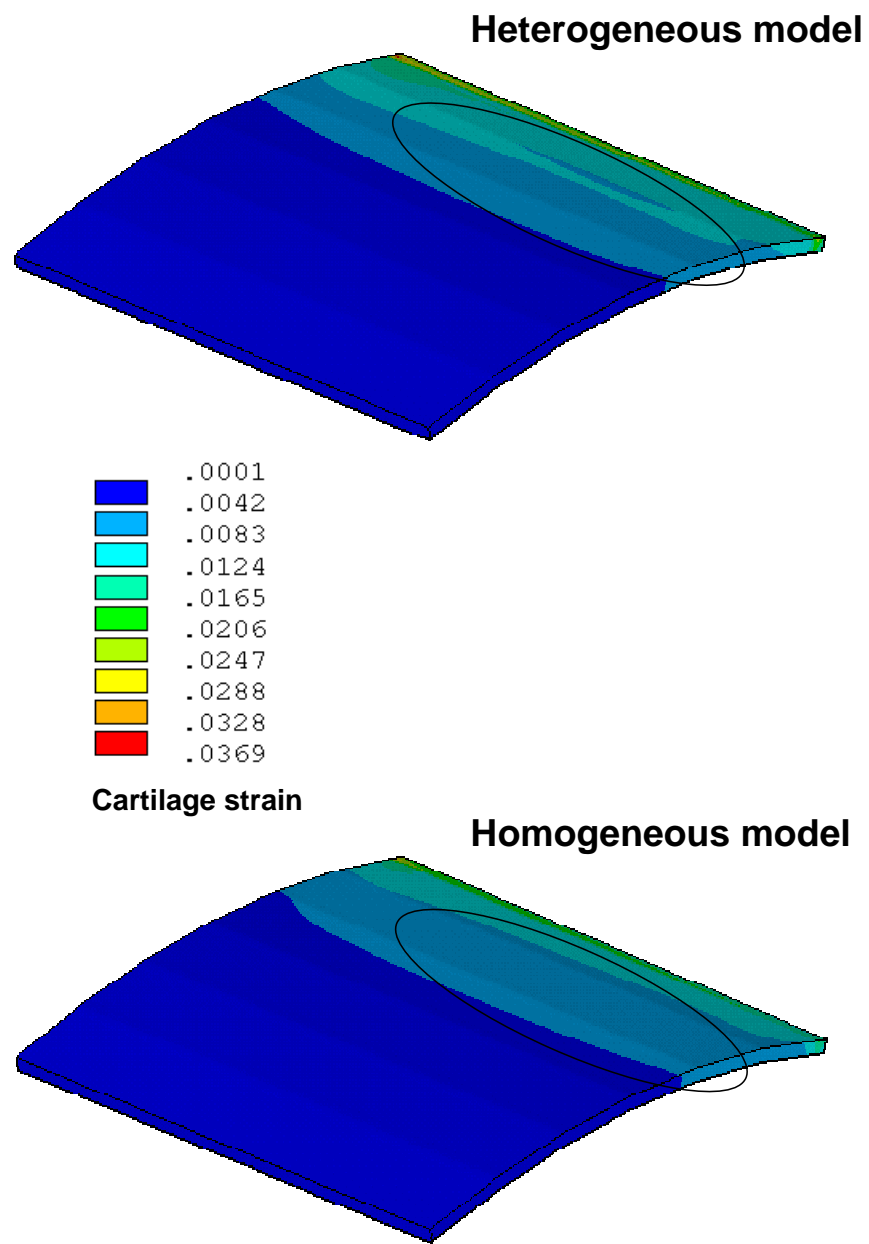
Homogeneous model

Figure 3.7   von Mises strain distributions in the cartilage layer for the heterogeneous model (top) and homogeneous model (bottom). Circle indicates the difference in the strain distributions.

The normal strain distributions in the mucosa layer for both models are shown in Figure 3.8. As can be seen from this figure, the distributions of normal strain in the mucosa layer for both material models were different. High normal strain areas from the heterogeneous model were smaller than those from the homogeneous model. The maximum normal strain in the mucosa layer from the heterogeneous model was higher than that for the homogeneous model. This maximum was 1.6% and 1.5% for the heterogeneous model and homogeneous model, respectively. The maximum normal strain in the smooth muscle layer from the heterogeneous model was lower than that for the homogeneous model. This maximum was 0.48% and 0.53% for the heterogeneous model and homogeneous model, respectively. The distributions of normal strain in the smooth muscle layer for both models were also different. High normal strain areas from the heterogeneous model were smaller than those from the homogeneous model (see Figure 3.9). The normal strain distributions in the cartilage layer for both models are shown in Figure 3.10. The maximum normal strain in the cartilage layer from the heterogeneous model was higher than that for the homogeneous model since the cartilage layer in the heterogeneous model is less stiff than that in the homogeneous model. This maximum was 1.10% and 0.99% for the heterogeneous model and homogeneous model, respectively. The distributions of normal strain in the cartilage layer from both models were also different. High normal strain areas from the heterogeneous model were smaller than those from the homogeneous model.

Heterogeneous model

-.001099
.834E-03
.002768
.004701
.006634
.008568
.010501
.012434
.014368
.016301

Mucosa normal strain
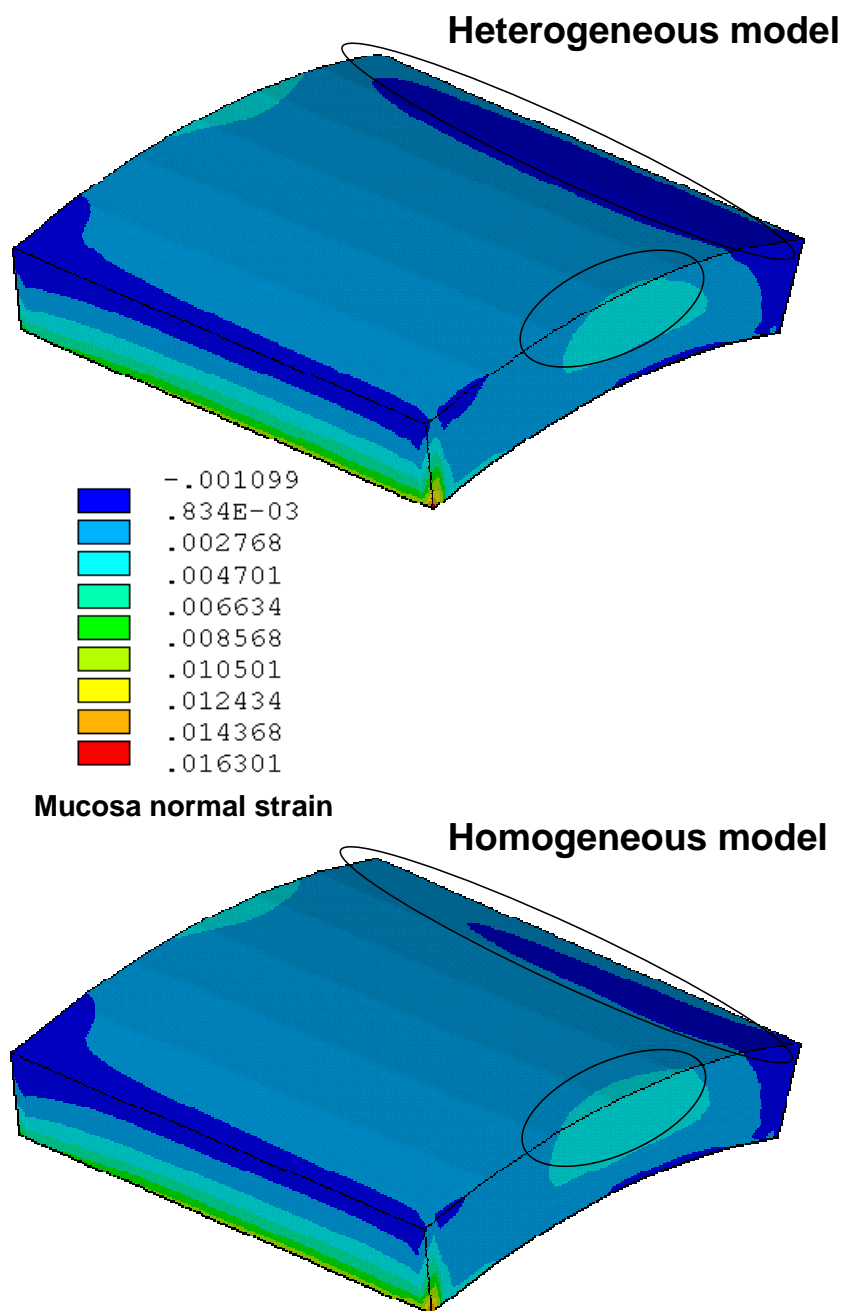
Homogeneous model

Figure 3.8   Normal strain distributions in the mucosa layer for the heterogeneous model (top) and homogeneous model (bottom). Circles indicate the difference in the strain distributions.

Heterogeneous model

Smooth muscle normal strain
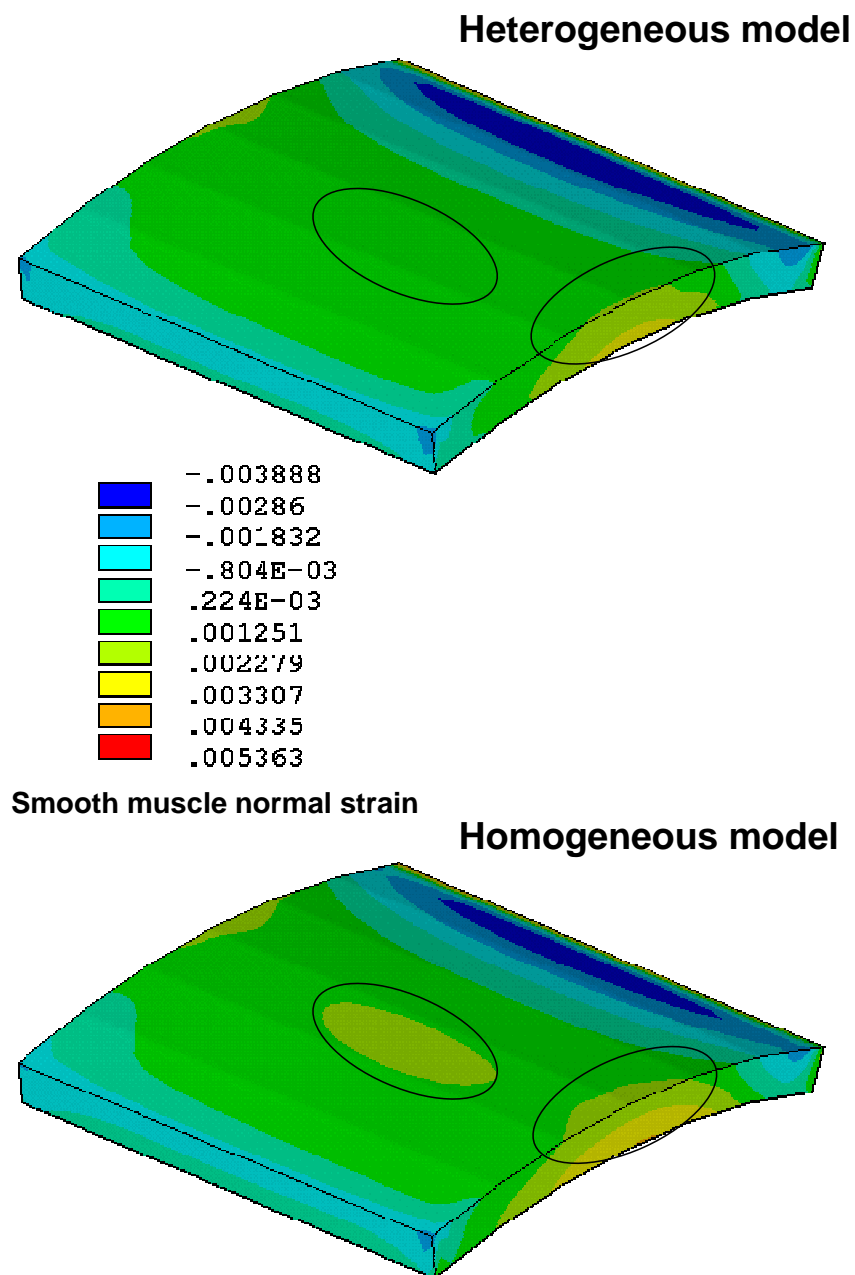
Homogeneous model

Figure 3.9   Normal strain distributions in the smooth muscle layer for the heterogeneous model (top) and homogeneous model (bottom). Circle indicates the difference in the strain distributions.

Heterogeneous model

	−.010603
	−.008349
	−.006095
	−.003841
	−.001587
	.667E−03
	.002921
	.005175
	.007429
	.009683

Cartilage normal strain
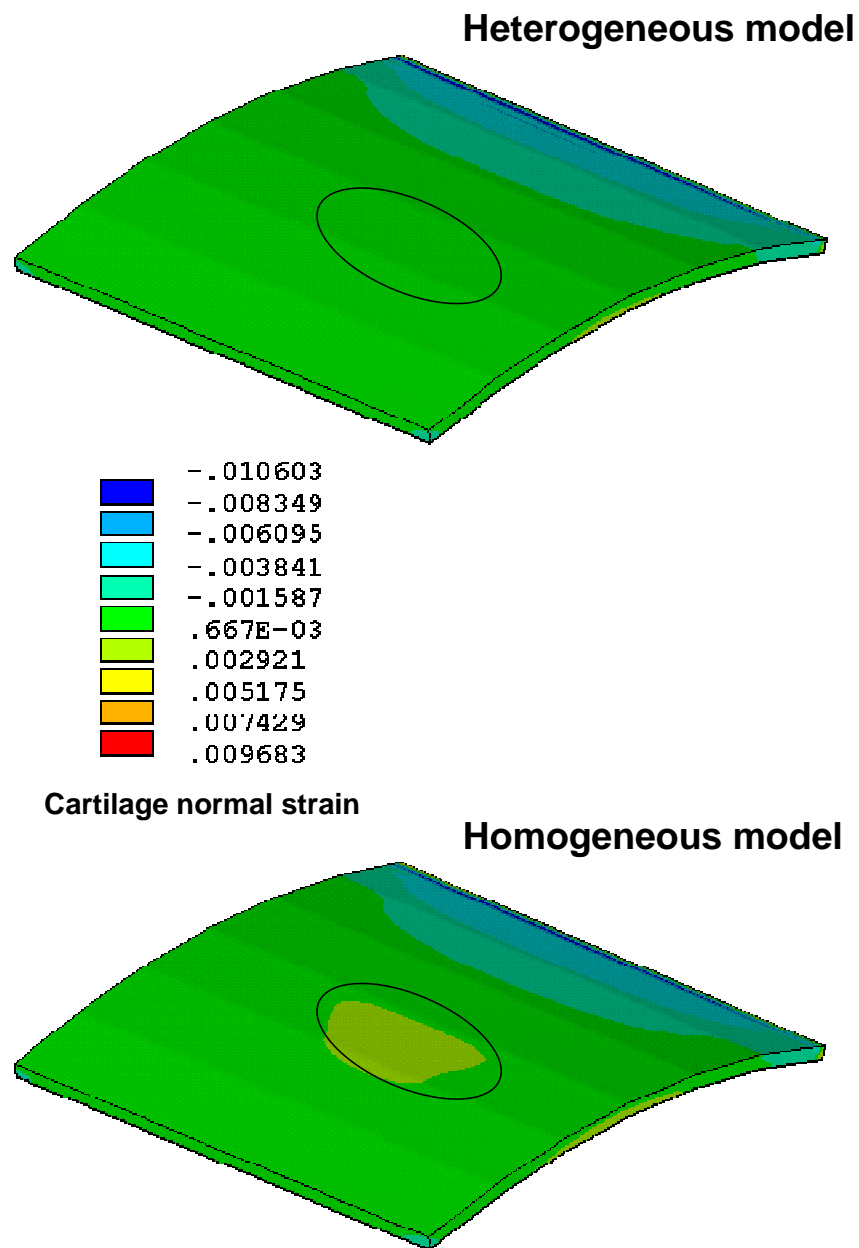
Homogeneous model

Figure 3.10   Normal strain distributions in the cartilage layer for the heterogeneous model (top) and homogeneous model (bottom). Circle indicates the difference in the strain distributions.

The shear strain distributions in the mucosa layer for both models are shown in Figure 3.11. As can be seen from this figure, the distributions of shear strain in the mucosa layer for both material models were different. High shear strain areas from the heterogeneous model were smaller than those from the homogeneous model. The maximum shear strain in the mucosa layer from the heterogeneous model was lower than that for the homogeneous model since the mucosa layer in the heterogeneous model is stiffer than that in the homogeneous model. This maximum was 2.1% and 2.3% for the heterogeneous model and homogeneous model, respectively. The maximum shear strain in the smooth muscle layer from the heterogeneous model was greater than that for the homogeneous model since the smooth muscle layer in the heterogeneous model is less stiff than that in the homogeneous model. This maximum was 1.9% and 1.8% for the heterogeneous model and homogeneous model, respectively. The distributions of shear strain in the smooth muscle layer for both models were also different. High shear strain areas from the heterogeneous model were bigger than those from the homogeneous model (see Figure 3.12). The shear strain distributions in the cartilage layer for both models are shown in Figure 3.13. The maximum shear strain in the cartilage layer from the heterogeneous model was greater than that for the homogeneous model since the cartilage layer in the heterogeneous model is less stiff than that in the homogeneous model. This maximum was 2.8% and 2.6% for the heterogeneous model and homogeneous model, respectively. The distributions of shear strain in the cartilage layer from both models were also different. High shear strain areas from the heterogeneous model were bigger than those from the homogeneous model.

Heterogeneous model

■ (blue)	$-.022994$
■	$-.019489$
■	$-.015985$
■	$-.01248$
■	$-.008976$
■ (green)	$-.005471$
■	$-.001967$
■ (yellow)	$.001538$
■ (orange)	$.005042$
■ (red)	$.008547$

Mucosa shear strain
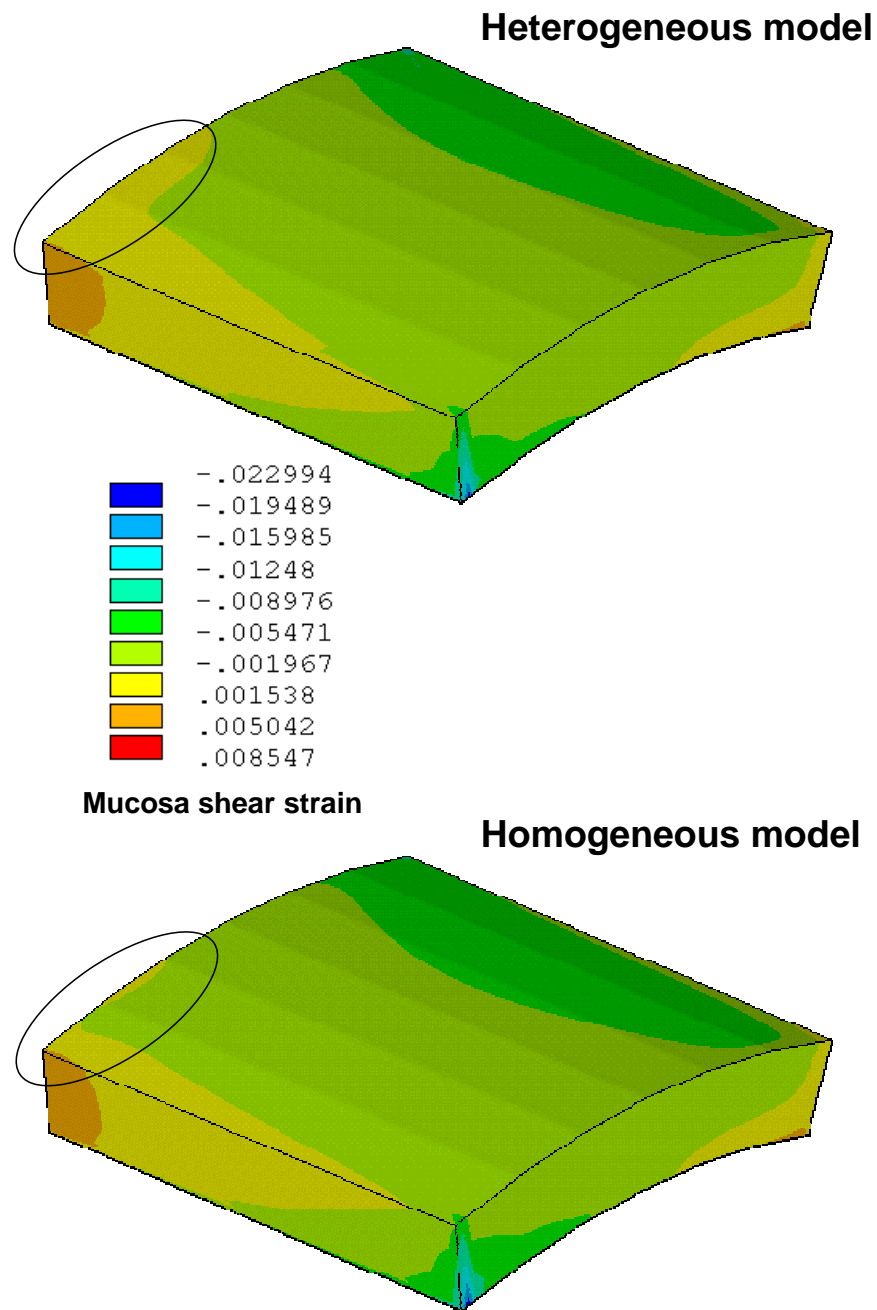
Homogeneous model

Figure 3.11   Shear strain distributions in the mucosa layer for the heterogeneous model (top) and homogeneous model (bottom). Circle indicates the difference in the strain distributions.

Heterogeneous model

	−.019028
	−.016602
	−.014175
	−.011749
	−.009323
	−.006896
	−.00447
	−.002044
	.383E−03
	.002809

Smooth muscle shear strain
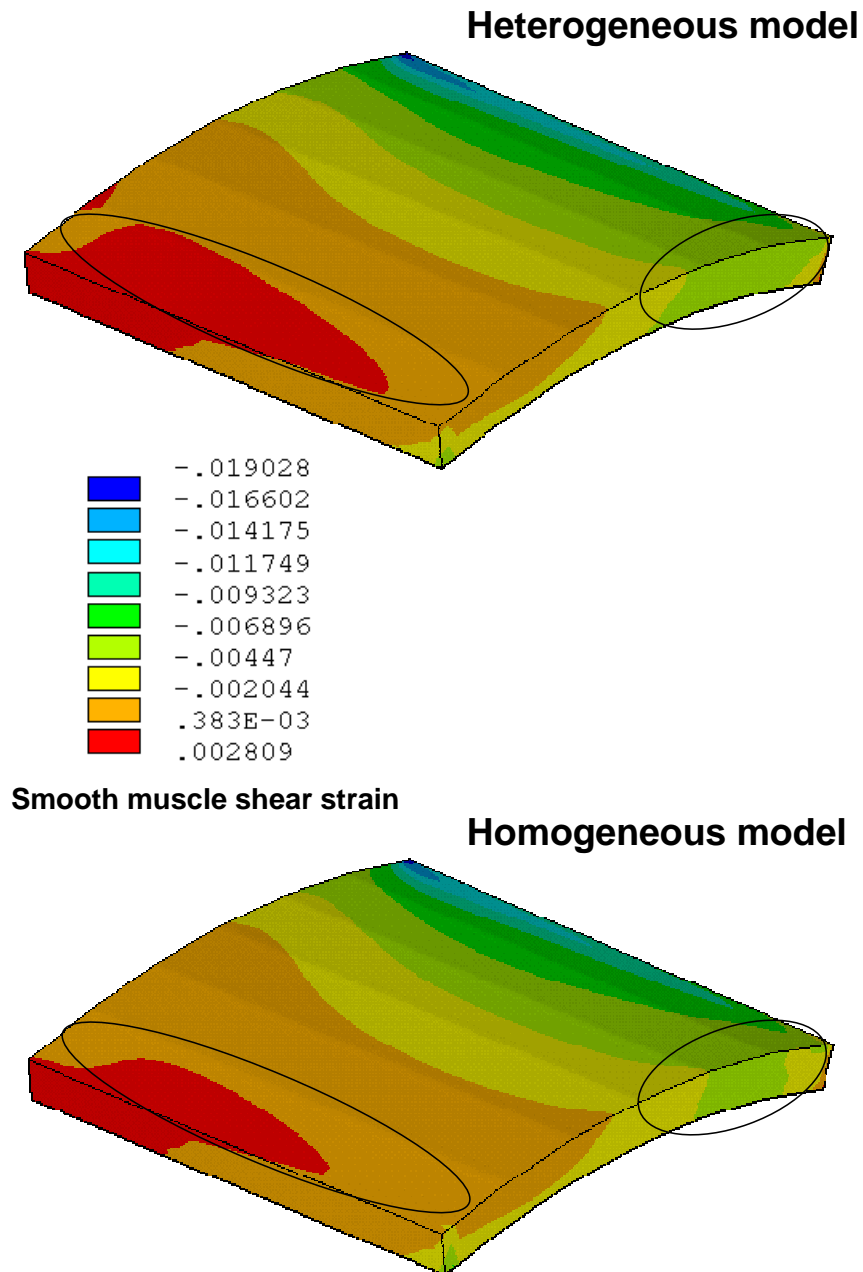
Homogeneous model

Figure 3.12   Shear strain distributions in the smooth muscle layer for the heterogeneous model (top) and homogeneous model (bottom). Circle indicates the difference in the strain distributions.

Heterogeneous model


```
      -.027968
      -.024559
      -.021151
      -.017742
      -.014333
      -.010925
      -.007516
      -.004107
      -.699E-03
       .00271
```

Cartilage shear strain
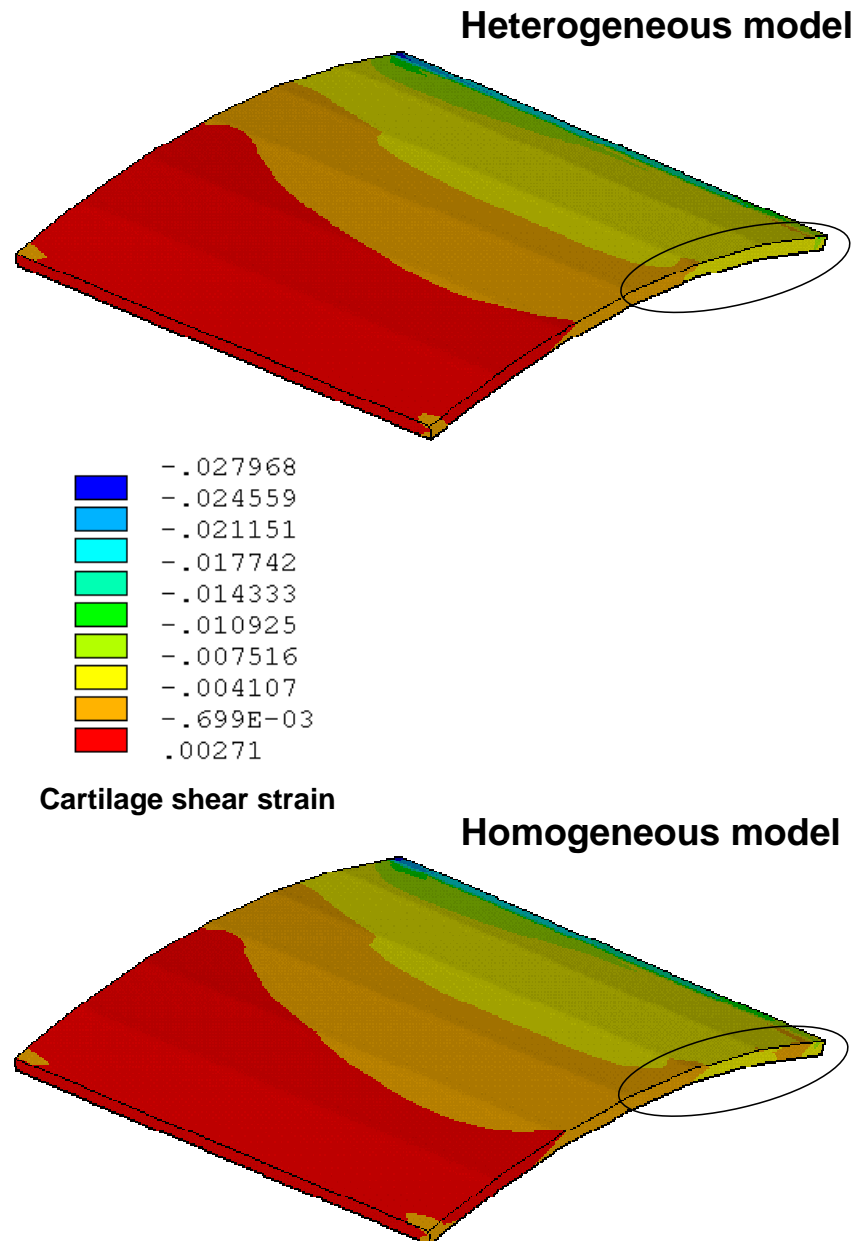
Homogeneous model

Figure 3.13 Shear strain distributions in the cartilage layer for the heterogeneous model (top) and homogeneous model (bottom). Circle indicates the difference in the strain distributions.

3.8 Discussion

The computational model that incorporates the heterogeneity of the airways was developed to study strain distributions in each airway layer since it is very difficult to measure the distributions of strains in real tissue due to thickness of each layer in the airways is very thin. The effect of the material model on strain distributions in each airway layer was investigated using heterogeneous and homogeneous material models. The simulation results showed that the material model highly affected a pattern of the strain distributions in the airway. The material model also affected the maximum strain in each airway layer. Overall, the homogeneous material model overestimated the maximum strain level in the mucosa layer about 11% and underestimated the maximum strain level about 12% and 16% in the smooth muscle and cartilage layer, respectively. It is very interesting to note that there were both normal and shear strain components in each layer although the airway displacement from the organ-level model was in the normal direction.

Strain level in the airway can activate neutrophils via release of interleukin (IL)-8 without cell injury. The experiment in alveolar epithelial cells showed that cells with 10-15% linear strain released IL-8 about 8-49% more than the normal cells (Vlahakis et al., 1999). Strain level also acted synergistically with activated eosinophils to induce upregulation of gene in airway remodeling in diseases such as asthma (Choe et al., 2003; Haseneen et al., 2002). In addition, strain caused cell injury (Tschumperlin and Margulies, 1998; Tschumperlin et al., 2000), apotosis (Hammerschmidt et al., 2004), and

necrosis (Hammerschmidt et al., 2004). Therefore, it is very important to incorporate the heterogeneity of the airway into the computational model at the tissue level so that the strain level in each airway layer can be accurately obtained.

3.9 Summary

The tissue-level model was developed to study the strain distributions in each layer of the airway tissue. The geometry and boundary conditions of the tissue-level model were obtained from the organ-level model. The finite element method was chosen to solve the continuum model used to describe the distributions of strain in the airway tissue. The effect of material properties on the strain distributions was investigated assuming that the airway tissue is either heterogeneous or homogeneous. The simulation results showed that the homogeneous model overestimated the maximum strain in the mucosa layer; however the homogeneous model underestimated the maximum strain in the smooth muscle and cartilage layers. Since the strain levels from the tissue-level model is transferred to the cellular-level model for studying inflammatory responses in cellular level, it is important to treat the airway tissue as a heterogeneous material when distributions of strain in each layer were considered.

CHAPTER 4 Cellular-Level Models

4.1 Introduction

Inflammation is complex responses of the organism to the pathogens, damage cells or irritants. It involves immune cells and various cells within the injured tissues. Without the inflammation, the harmful stimuli cannot be removed and the healing process cannot be occurred. However, an overexpression or underexpression of inflammatory responses can cause a problem. Patients with immunodeficiency diseases can have recurrent or overwhelming infections since one or more components of the immune system are defective. On the other hand, if the immune responses are too strong or occur in the absence of infection they can cause tissue damage, which can lead to autoimmune diseases. Many mathematical models have been developed to describe inflammatory responses to pathogens (Day et al., 2006; Hancioglu et al., 2007; Kumar et al., 2004; Reynolds et al., 2006). However, there is one big flaw in those models. The encounter of pathogens and immune cells was assumed to be occurred uniformly throughout the tissue. The encounter in real situation is not uniform for the whole tissue. Some parts of the tissue might have the encounter and some parts might not. The computational model that

takes this issue into account would help physicians or researchers better understand inflammatory responses in human body.

In this chapter, the discrete model that incorporates all biophysical processes during inflammatory responses is developed. The details of the discrete model for the cellular-level model are also discussed. The results from the model are validated against other computational models and the possible outcomes of the results are discussed.

4.2 Inflammatory Responses

The inflammation process in the airways begins by an encounter of the pathogens or damage cells with macrophages. The encounter will trigger macrophages to release proinflammatory cytokines, a protein that can cause vasodilation and increase the permeability of blood vessels. Vasodilation and increase blood vessel permeability induces responses that are collectively known as inflammation: heat, redness, pain, and swelling (Janeway et al., 1999). Cytokines also stimulate neighboring cells to secrete the chemoattractant of other inflammatory cells; e.g. macrophages and neutrophils. The activated inflammatory cells release cytotoxic mediators that can kill pathogen or damage cells. Not only can these cytotoxic mediators kill pathogen but it also can damage healthy epithelial cells. During mechanical ventilation, stresses and strains in the airways act synergistically with the inflammatory processes and increases inflammatory cell recruitment, neutrophils, through releasing of proinflammatory cytokines, e.g., interleukin (IL)-8 (Okada et al., 1998; Pugin et al., 1998; Pugin and Oudin, 2006;

Vlahakis et al., 1999). The cytotoxic mediators releasing by activated neutrophils can damage healthy epithelial cells. These damage cells can then induce more inflammation (Jaeschke and Smith, 1997).

4.3 Inflammatory Responses Models

4.3.1 Inflammatory Responses due to Pathogen

Although the coagulation and inflammatory responses are related, the inflammatory responses were only modeled in the research. The inflammatory responses model at the cellular level was developed implementing the cellular automata (CA) model. The CA model was composed of two species: epithelial cell and immune cell. The pathogen was not explicitly considered but it was modeled as spreading directly from one epithelial cell to another. The CA model was constructed on two-dimensional square lattice where each lattice site represented one epithelial cell (see Figure 4.1). The immune cell was mobile and can move from one lattice to another. Therefore, the square lattice was like the tissue of immobile epithelial cells which is patrolled by the mobile immune cells. The CA was updated synchronously based on specific rules. The boundary conditions for both epithelial and immune cells were periodic boundary, i.e., an immune cell moving off from one edge of the lattice was reintroduced at the opposite edge and an infectious epithelial cell at one edge can infect a healthy epithelial cell at the opposite edge. Finally, neighborhood of the lattice was defined as eight closest lattice sites, i.e.,

Moore neighborhood (see Figure 4.1). Details of the CA rules for each species were

derived from the inflammatory processes in human body and are described below.
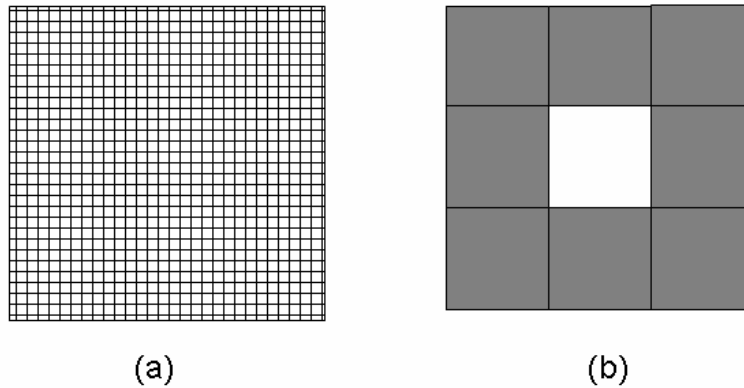
Figure 4.1   (a) Two-dimensional square lattice used for the inflammatory responses
model. (b) Moore neighborhood (dark) of each lattice site (white)

An epithelial cell can be in any of six states: healthy, containing, expressing,

infectious, damage, and dead (see Figure 4.2). Transition of each state occurs as follows:

- Rule 1: A healthy cell becomes a containing cell with probability P_I

$$P_I = 1 - \left(1 - P_{1I}\right)^{N_I}$$

where P_{1I} is a probability that one infectious cell can infect a healthy cell and N_I is a

number of an infectious cell in the neighborhood.

- Rule 2: An containing cell becomes an expressing cell after being infected for

    $T_{EXPRESS}$ time steps

- Rule 3: An expressing cell becomes an infectious cell after being infected for $T_{INFECTIOUS}$ time steps

- Rule 4: An infectious cell becomes a dead cell when it is older than its life span L_I

- Rule 5: A healthy cell becomes a dead cell when it is older than its life span L_H

- Rule 6: A dead cell becomes a healthy cell after $T_{DIVISION}$ time steps if there is at lease one healthy cell in the neighborhood

- Rule 7: A healthy cell becomes a damage cell if there are at least N_D immune cells in the neighborhood

- Rule 8: An expressing, infectious, and damage cell becomes a dead cell with probability

$$P_{PH} = 1 - (1 - P_{1PH})^{N_{AC}}$$

where P_{1PH} is a probability that one activated immune cell can phagocyte other cells and N_{AC} is a number of an activated immune cell in the neighborhood.
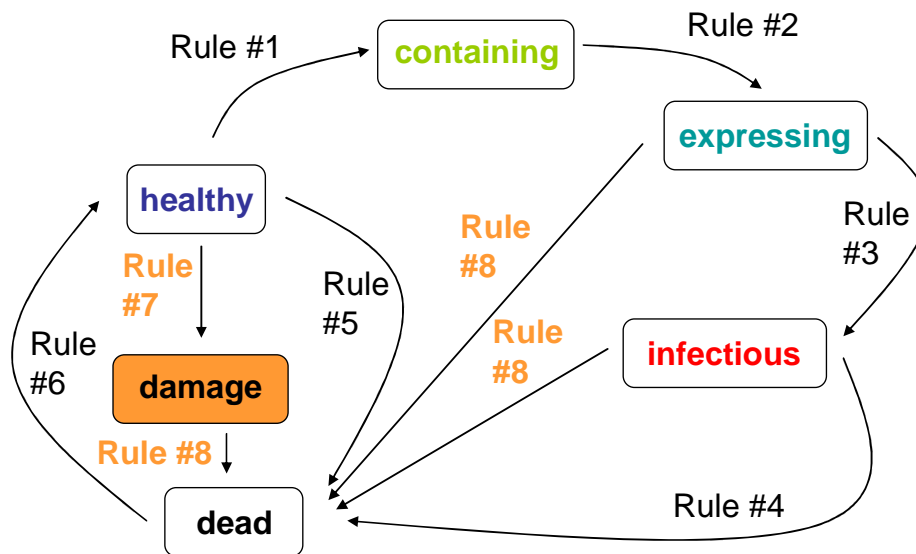
Figure 4.2 Possible states of an epithelial cell during inflammatory responses due to pathogen

An immune cell can be in any of three states: inactivated, activated, and dead (see Figure 4.3). An inactivated immune cell is an immune cell that has no specificity. An activated immune cell is an immune cell that has encountered an expressing, infectious, or damage cell or has been recruited by another activated immune cell. Transition of each state occurs as follows:

- Rule 9: An inactivated immune cell becomes an activated immune cell and start recruiting activated immune cells with the recruitment rates θ_R and T_{DELAY} when it is in the neighborhood of an expressing, infectious, or damage cell

- Rule 10: An activated immune cell becomes a dead immune cell when it is older than its lifespan L_{AC}

- Rule 11: An inactivated immune cell becomes a dead immune cell when it is older than its lifespan L_{INAC}
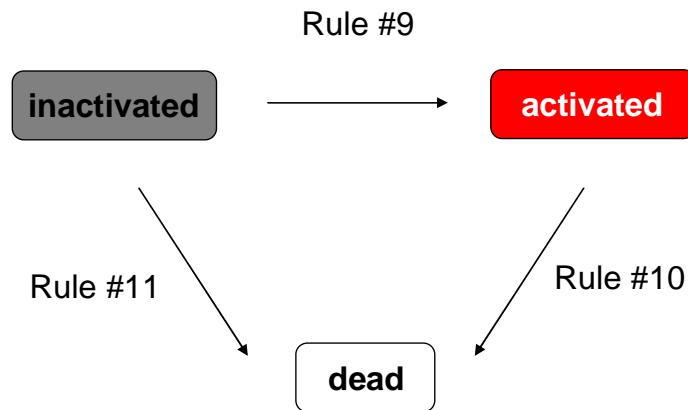
Figure 4.3   Possible states of an immune cell during inflammatory responses due to pathogen

4.3.2 Inflammatory Responses due to Strain Levels

The inflammatory responses due to strain levels during mechanical ventilation was developed implementing the cellular automata (CA) model. The CA model was composed of two species: epithelial cell and immune cell. The CA model was constructed on two-dimensional square lattice where each lattice site represented one epithelial cell (see Figure 4.1). The immune cell was mobile and can move from one lattice to another. Therefore, the square lattice was like the tissue of immobile epithelial cells which was patrolled by the mobile immune cells. The CA was updated synchronously based on specific rules. The boundary conditions for both epithelial and immune cells were periodic boundary, i.e., an immune cell moving off from one edge of the lattice was

reintroduced at the opposite edge. Finally, neighborhood of the lattice was defined as eight closest lattice sites, i.e., Moore neighborhood (see Figure 4.1). Details of the CA rules for each species experiencing strain levels during mechanical ventilation are described below.

An epithelial cell can be in any of three states: healthy, damage, and dead (see Figure 4.4). Transition of each state occurs as follows:

- Rule 1: A healthy cell becomes a dead cell when it is older than its life span L_H

- Rule 2: A dead cell becomes a healthy cell after $T_{DIVISION}$ time steps if there is at lease one healthy cell in the neighborhood

- Rule 3: A healthy cell becomes a damage cell if there are at least N_D immune cells in the neighborhood

- Rule 4: A damage cell becomes a dead cell with probability

$$P_{PH} = 1 - (1 - P_{1PH})^{N_{AC}}$$

where P_{1PH} is a probability that one activated immune cell can phagocyte other cells and N_{AC} is a number of an activated immune cell in the neighborhood.
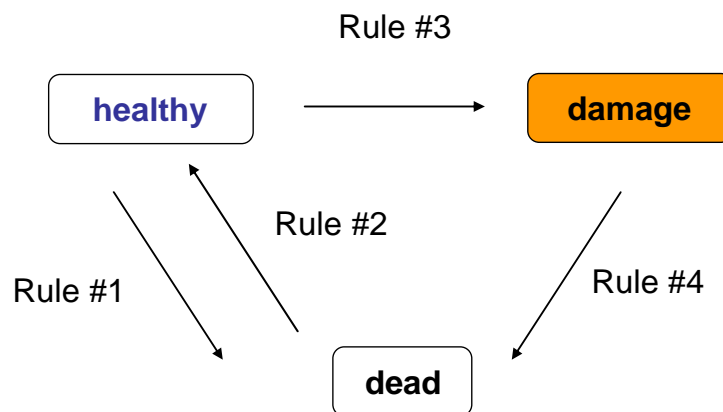
Figure 4.4   Possible states of an epithelial cell during inflammatory responses due to strain levels

An immune cell can be in any of three states: inactivated, activated, and dead (see Figure 4.5). An inactivated immune cell is an immune cell that has no specificity. An activated immune cell is an immune cell that has encountered a damage cell or has been recruited by another activated immune cell. Transition of each state occurs as follows:

- Rule 5: An inactivated immune cell becomes an activated immune cell and start recruiting activated immune cells with the recruitment rates θ_R and T_{DELAY} when it is in the neighborhood of a damage cell.

- Rule 6: An activated immune cell becomes a dead immune cell when it is older than its lifespan L_{AC}

- Rule 7: An inactivated immune cell becomes a dead immune cell when it is older than its lifespan L_{INAC}

Rule #5

inactivated → **activated**

Rule #7   Rule #6

dead
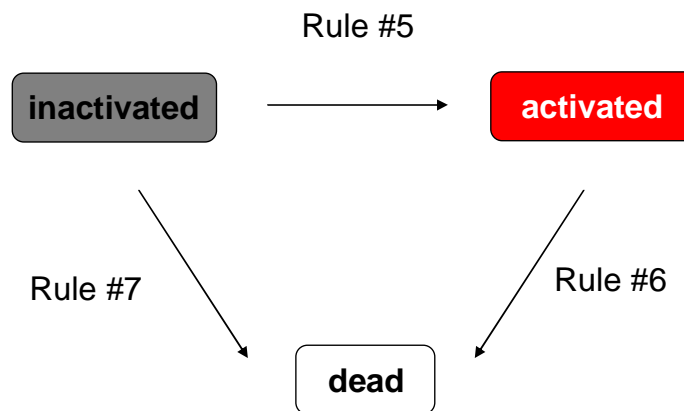
Figure 4.5   Possible states of an immune cell during inflammatory responses due to strain levels

4.4 Method of Analysis

4.4.1 Inflammatory Responses due to Pathogen

The CA rules described in the section 4.3.1 were implemented using MATLAB. The simulation was performed on a lattice of 100×100 sites which represented a tissue area of 2×2 mm^2 (Segovia-Juarez et al., 2004). The initial population of immune cells was 200 cells. This value represents the normal level of immune cells in our body (Segovia-Juarez et al., 2004). The periodic boundary conditions were used for the simulation. The initial conditions were one containing cell at the center of the lattice sites with randomly placed immune cells. Only one immune cell can occupy one lattice site. Each epithelial cell was randomly assigned its lifespan. The simulations were carried out with the following physiological assumptions: 1) only healthy epithelial cells are able to divine and 2) Immune cells cannot be infected.

The default parameters for the rules are tabulated in Table 4.1. As can be seen from this table, there is no values for P_{1I} and P_{1PH}. The parameter P_{1I} represents the possibility that pathogen can penetrate into the epithelial cell and it strongly depends on the pathogen type. The parameter P_{1PH} represents the possibility that an activated immune cell can phagocytose the pathogen and it strongly depends on the affinity to the pathogen strain. For this reason, the ratio of P_{1I} to P_{1PH} was varied in the analysis to see the effect of these two parameters on the outcome on inflammatory responses. One simulation time step corresponds to 4-h real time.

Table 4.1   Parameters for the CA model of inflammatory responses due to pathogen from Beauchemin et al (2005)

Parameters	Values	Description
$T_{EXPRESS}$	4 h	Delay from containing to express
$T_{INFECTIOUS}$	8 h	Delay from containing to infectious
$T_{DIVISION}$	12 h	Duration of an epithelial cell division
T_{DELAY}	8 h	Delay between recruitment call and adding new activated immune cells
L_H	380 h	A healthy epithelial cell lifespan
L_I	24 h	An infected epithelial cell lifespan
L_{AC}	168 h	An activated immune cell lifespan
L_{INAC}	2400 h	An inactivated immune cell lifespan
N_D	5	Number of immune cells that can damage a healthy epithelial
θ_R	25	Number of immune cells recruited after the encounter of pathogen and an immune cell

4.4.2 Inflammatory Responses due to Strain Levels

The CA rules described in the section 4.3.2 were implemented using MATLAB. The simulation was performed on a lattice of 100×100 sites which represented a tissue area of 2×2 mm^2 (Segovia-Juarez et al., 2004). The initial population of immune cells was 200 cells. This value represents the normal level of immune cells in our body

(Segovia-Juarez et al., 2004). The periodic boundary conditions were used for the simulation. The initial conditions were randomly placed immune cells. Only one immune cell can occupy one lattice site. Each epithelial cell was randomly assigned its lifespan. The simulations were carried out with the following physiological assumptions: 1) only healthy epithelial cells are able to divine and 2) Strain levels do not affect inactivated immune cells. The default parameters for the rules are tabulated in Table 4.2. One simulation time step corresponds to 4-h real time.

To investigate an effect of strain level on the outcome on inflammatory responses, the strain level was varied in the analysis within ranges of 0.5-66%. These ranges represented the strain level occurring in airway generation 3 to 5 and the alveoli sac. The effect of strain level from mechanical ventilation on increase in an activated immune cell (neutrophil) can be calculated as follows.

Relationship between increase in IL-8 and strain level (Vlahakis et al., 1999)

$$Increase\ in\ IL\text{-}8\ (\%) = 3.14 \times Strain\ level\ (\%)$$

Relationship between increase in activated immune cell (neutrophil) and increase in IL-8 (Nassif et al., 1997)

$$Increase\ in\ neutrophil\ (\%) = 0.13 \times Increase\ in\ IL\text{-}8\ (\%)$$

Table 4.2   Parameters for the CA model of inflammatory responses due to strain level from Beauchemin et al (2005)

Parameters	Values	Description
$T_{DIVISION}$	12 h	Duration of an epithelial cell division
T_{DELAY}	8 h	Delay between recruitment call and adding new activated immune cells
L_H	380 h	A healthy epithelial cell lifespan
L_{AC}	168 h	An activated immune cell lifespan
L_{INAC}	2400 h	An inactivated immune cell lifespan
N_D	5	Number of immune cells that can damage a healthy epithelial
θ_R	25	Number of immune cells recruited after the encounter of pathogen and an immune cell

4.5 Results

4.5.1 Inflammatory Responses due to Pathogen

For all results shown, at least 50 simulations have been carried out in order to give general results of the parameter set. There are four possible outcomes in response to the value of the parameter set. Each outcome corresponds to a clinical condition. Figure 4.6 shows results corresponding to a healthy response to the infection (first outcomes). As can be seen from this figure, the infected cell at the center lattice spread to other healthy

epithelial cells with increasing time step. The immune cells at this time step concentrated in the infection regions. As time steps progressed, the ring of the infection regions was broken into many small regions due to an infiltration of immune cells. The immune cells at this time step still concentrated in small infection areas. Once immune cells phagocytosed all pathogen, immune cells spread all over the entire lattice and returned to a normal value.

The number of healthy, infected, damage, dead, and immune cells as a function of time step is shown in Figure 4.7. Infected cells increased and reached a maximum level. At the same time, healthy cells decreased and reached a minimum level. Immune cells rapidly started increasing and reached a maximum level. The increase of the immune cells increased a probability that immune cells can phagocyte infected cells. For this reason, infected cells rapidly decreased and dead cells started increasing. As time steps increased, an infected and dead cell became zero as well as a healthy and immune cell returned to the original value. This outcome occurred when the ratio of P_{1I} to P_{1PH} was less than 1.2. In this case, the possibility that immune cells can phagocytose pathogen was higher that the possibility that pathogen can penetrate into epithelial cells.

Figure 4.6   Simulation results of the CA model corresponding to the healthy outcome after 1 (top left), 17 (top right), 29 (bottom left), and 100 (bottom right) time steps. White: immune; Blue: healthy; Turquoise: containing; Green: expressing; Red: infectious; Yellow: damage; Black: dead
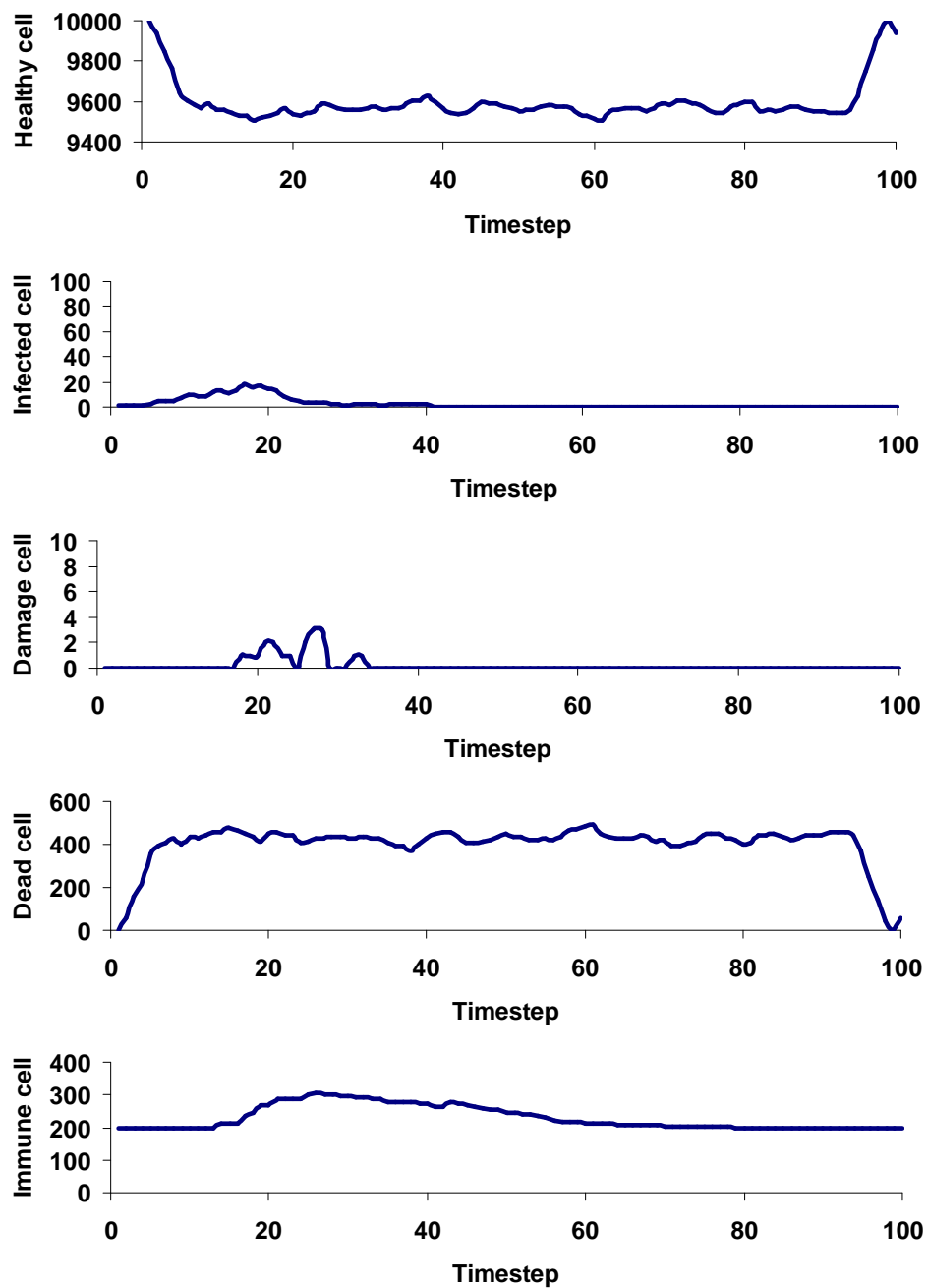
Figure 4.7   The number of healthy, infected, damage, dead, and immune cells as a function of time step corresponding to the healthy outcome

In a second case, the outcome is related to the state of persistent infectious inflammation, where the inflammatory responses is high but the pathogen still cannot be cleared. Figure 4.8 shows responses of this case a function of time. The infected cell at the center lattice spread to other healthy epithelial cells with increasing time step. The immune cells at this time step concentrated in the infection regions. As time steps progressed, the ring of the infection regions was broken into many small regions due to an infiltration of immune cells. The immune cells at this time step still concentrated in small infection areas. However, the immune cells cannot digest all pathogen. The number of infected cells increased with increasing time step. The number of healthy, infected, damage, dead, and immune cells as a function of time step is shown in Figure 4.9. Infected cells increased and reached a maximum level. At the same time, healthy cells decreased and reached a minimum level. Immune cells rapidly started increasing and reached a maximum level. The increase of the immune cells increased a probability that immune cells can phagocyte infected cells; however it was not enough to get rid of the pathogen. For this reason, infected cells decreased and dead cells started increasing. As time steps increased, infected, dead, and immune cells stayed at the high value and never returned to the original value. This outcome occurred when the ratio of P_{1I} to P_{1PH} was higher than 1.2 or the recruit rate θ_R was less than 25. In this case, the possibility that immune cells can phagocytose pathogen was lower that the possibility that pathogen can penetrate into epithelial cells due to a low affinity to pathogen strain of immune cells or weak inflammatory responses.

Figure 4.8 Simulation results of the CA model corresponding to the persistent infectious inflammation outcome after 1 (top left), 10 (top right), 30 (bottom left), and 100 (bottom right) time steps. White: immune; Blue: healthy; Turquoise: containing; Green: expressing; Red: infectious; Yellow: damage; Black: dead

Figure 4.9   The number of healthy, infected, damage, dead, and immune cells as a function of time step corresponding to the persistent infectious inflammation outcome

Figure 4.10 shows responses of the outcome when the pathogen is cleared but the immune cells remain elevated, persistent non-infectious inflammation. The infected cell at the center lattice spread to other healthy epithelial cells with increasing time step. The immune cells at this time step concentrated in the infection regions. As time steps progressed, the immune cells can digest the pathogen. However, the immune cells caused damage cells. These damage cells induced more immune cells and caused a concentration of immune cells in one area. The damage cells and immune cells increased with increasing time step. The number of healthy, infected, damage, dead, and immune cells as a function of time step is shown in Figure 4.11. Infected cells increased and reached a maximum level. At the same time, healthy cells decreased and reached a minimum level. Immune cells rapidly started increasing and reached a maximum level. The increase of the immune cells increased a probability that immune cells can phagocyte infected cells; however, it damaged healthy epithelial cells. For this reason, infected cells decreased and dead cells started increasing. As time steps increased, and immune cells stayed at the high value and never returned to the original value. This outcome occurred when the recruit rate θ_R was higher than 30. In this case, the possibility that immune cells can phagocytose pathogen was higher that the possibility that pathogen can penetrate into epithelial cells due to strong inflammatory responses.
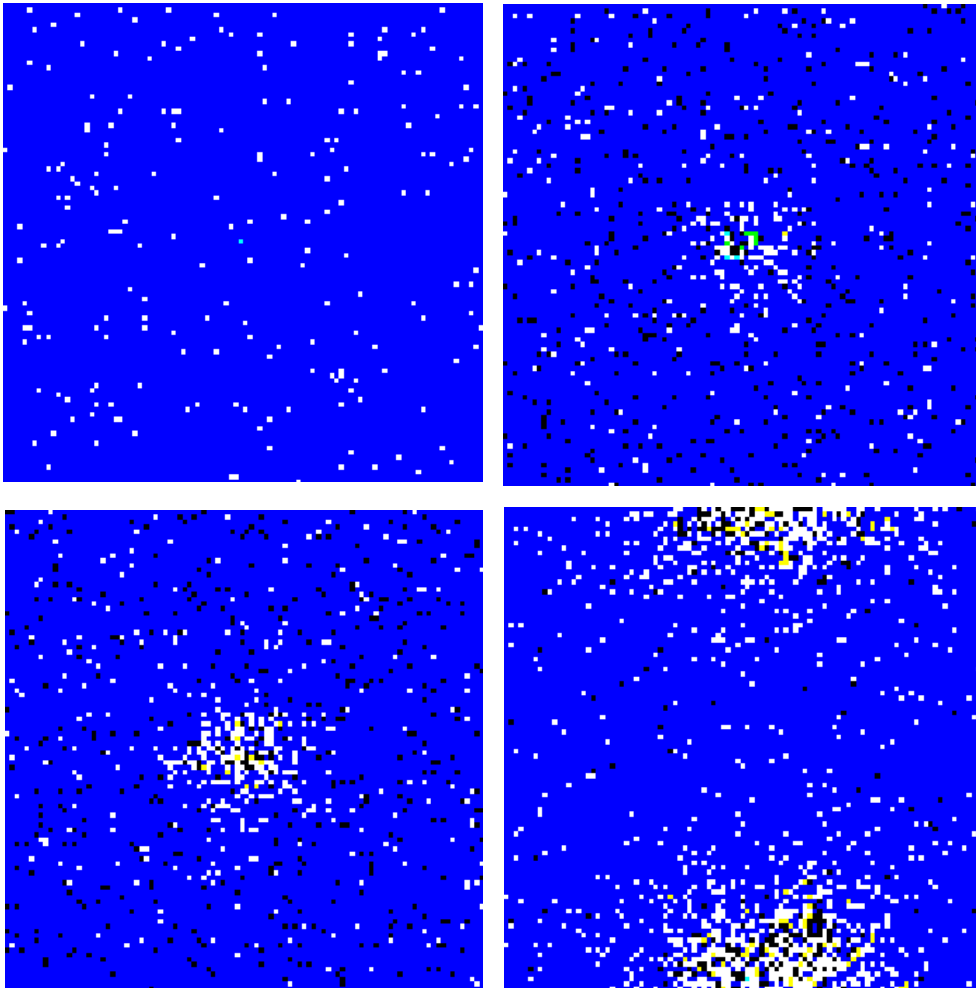
Figure 4.10 Simulation results of the CA model corresponding to the persistent non-infectious inflammation outcome after 1 (top left), 12 (top right), 20 (bottom left), and 100 (bottom right) time steps. White: immune; Blue: healthy; Turquoise: containing; Green: expressing; Red: infectious; Yellow: damage; Black: dead

Figure 4.11 The number of healthy, infected, damage, dead, and immune cells as a function of time step corresponding to the persistent non-infectious inflammation outcome

The last outcome represented the clinical state of immuno-deficiency, which has been observed in immuno-suppressed patient population such as HIV patients, the elderly, and patients with organ transplant (Schultz et al., 2001). The infected cell at the center lattice spread to other healthy epithelial cells with increasing time step; however, the immune cells remained low (see Figure 4.12). The number of healthy, infected, damage, dead, and immune cells as a function of time step is shown in Figure 4.13. Infected cells increased with increasing time step. Healthy cells decreased and immune cells remained at the low level with increasing time step. This outcome occurred when the recruit rate θ_R was lower than 10. In this case, the possibility that immune cells can phagocytose pathogen was lower that the possibility that pathogen can penetrate into epithelial cells due to weak inflammatory responses.
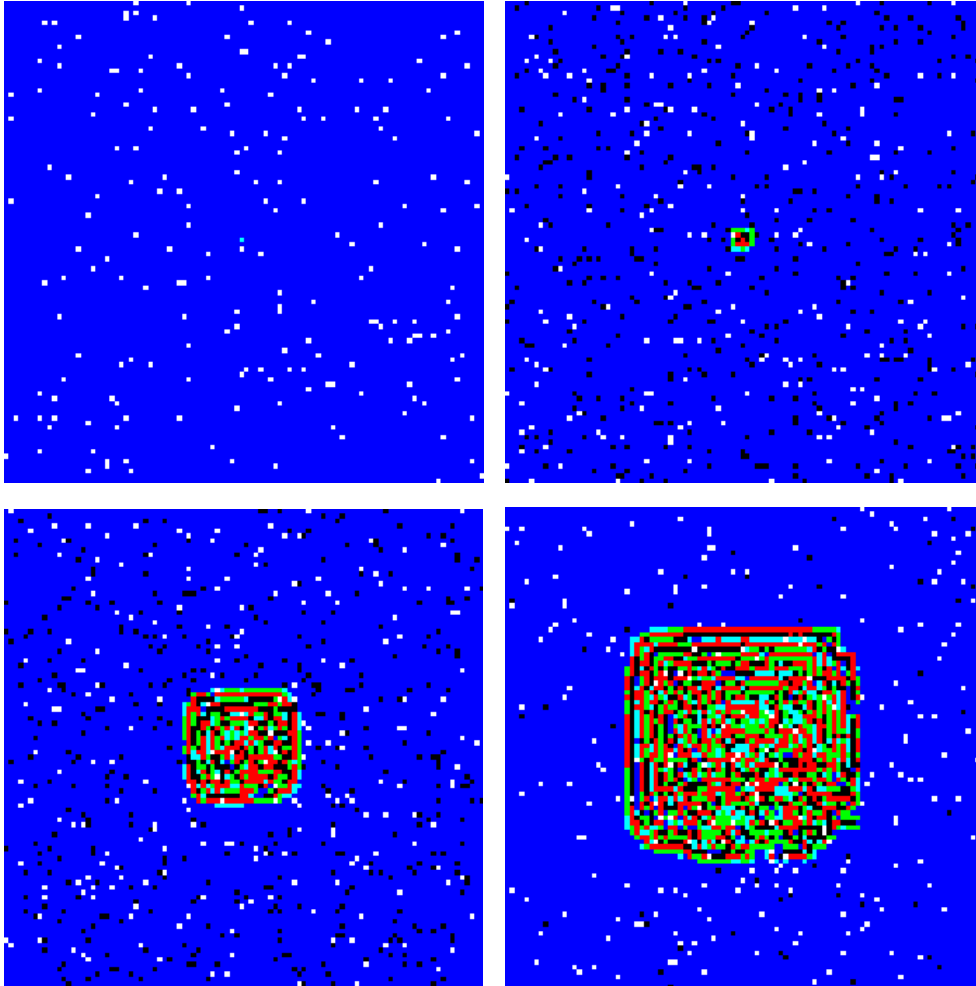
Figure 4.12 Simulation results of the CA model corresponding to the immuno-deficiency outcome after 1 (top left), 11 (top right), 50 (bottom left), and 100 (bottom right) time steps. White: immune; Blue: healthy; Turquoise: containing; Green: expressing; Red: infectious; Yellow: damage; Black: dead
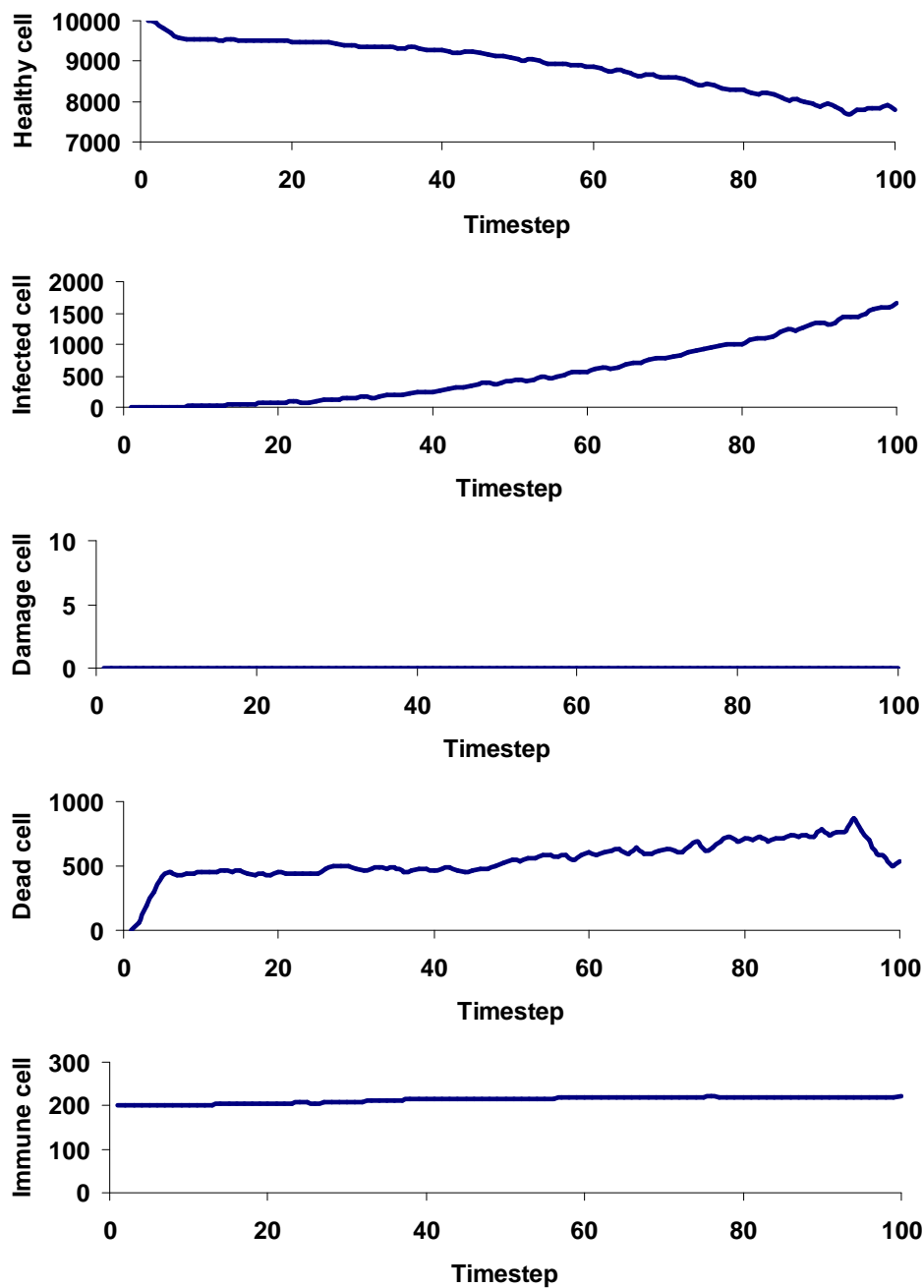
Figure 4.13 The number of healthy, infected, damage, dead, and immune cells as a function of time step corresponding to the immuno-deficiency outcome

4.5.2 <u>Inflammatory Responses due to Strain Levels</u>

For all results shown, at least 50 simulations have been carried out in order to give general results of the parameter set. The strain level was assumed to uniformly distribute throughout lattices. There are two possible outcomes in response to the value of the parameter set: healthy and tissue injury. In the healthy outcome, the immune cells distributed randomly over lattice space with increasing time step. There was no damage cell due to activated immune cells (see Figure 4.14). The number of healthy, damage, dead, and immune cells as a function of time step is shown in Figure 4.15. As can be seen from this figure, the number of immune cells increased, reached a maximum level, and stayed at that level, or remained constant with increasing time. No damage cell existed for the healthy outcome. This outcome occurred when the strain level was lower than 54%. In this case, the strain level was not high enough to recruit more activated immune cells to damage healthy cells.
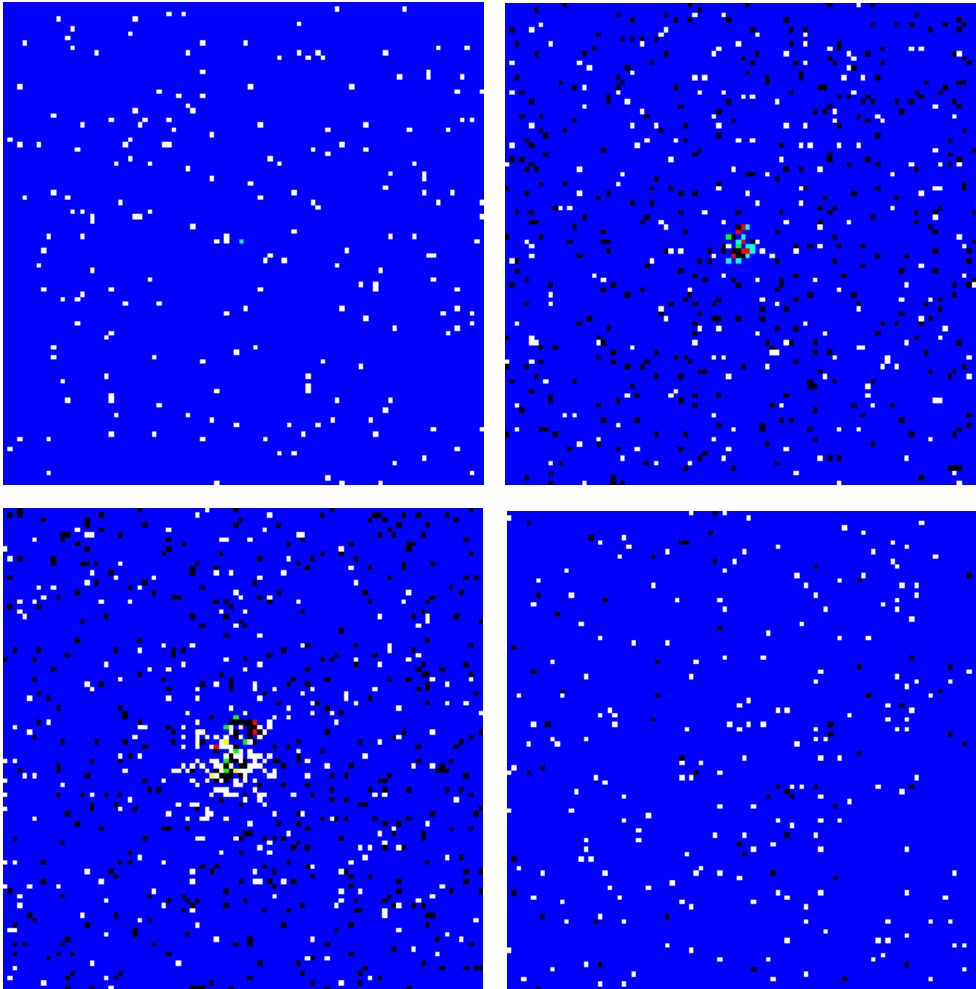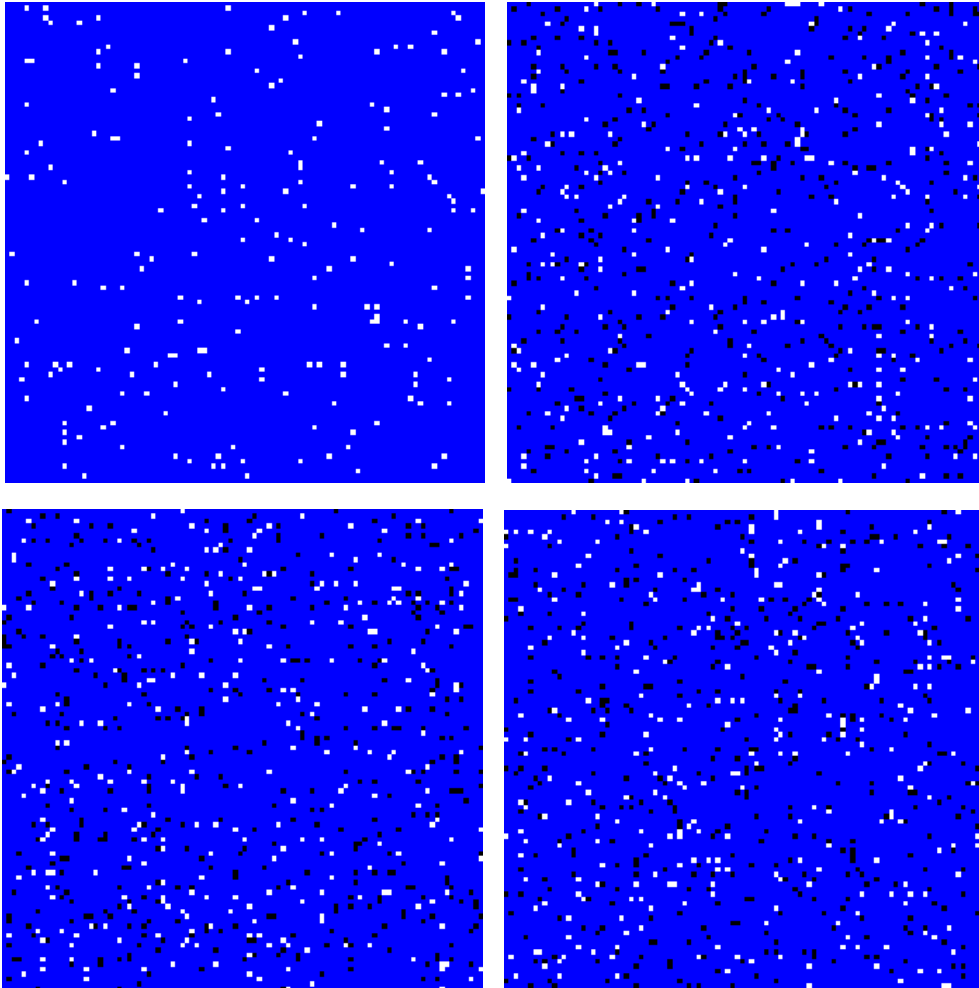
Figure 4.14 Simulation results of the CA model corresponding to the healthy outcome after 1 (top left), 60 (top right), 120 (bottom left), and 180 (bottom right) time steps. White: immune; Blue: healthy; Yellow: damage; Black: dead
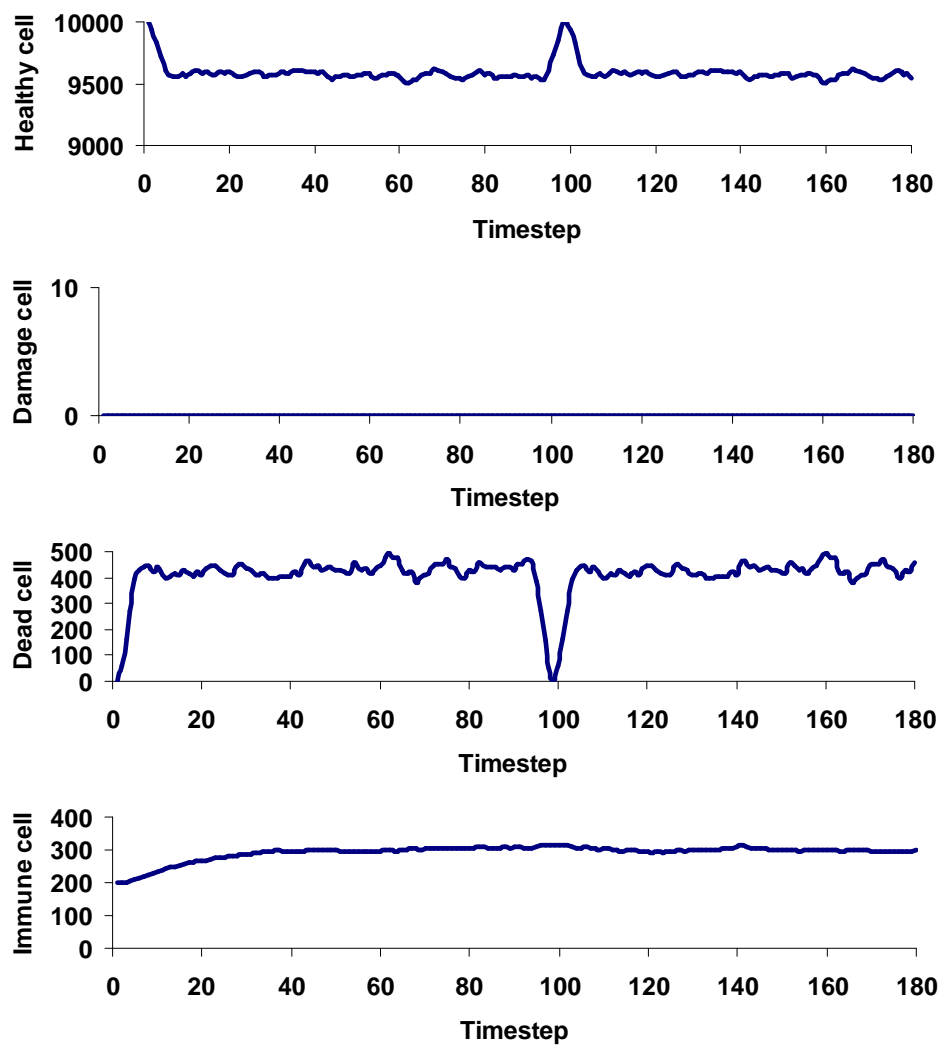
Figure 4.15 The number of healthy, damage, dead, and immune cells as a function of time step corresponding to the healthy outcome

Figure 4.16 shows response of the tissue injury outcome. The number of immune cells increased with increasing time step. This increase in activated immune cells damaged healthy cells. These damage cells in turn induced more activated immune cells. The number of healthy, damage, dead, and immune cells as a function of time step is shown in Figure 4.17. As can be seen from this figure, the number of immune cells increased, reached a maximum level, and stayed at that level. This increase in immune cells caused damage cells to dramatically increase. The tissue injury outcome occurred when the strain level was at least 54%.
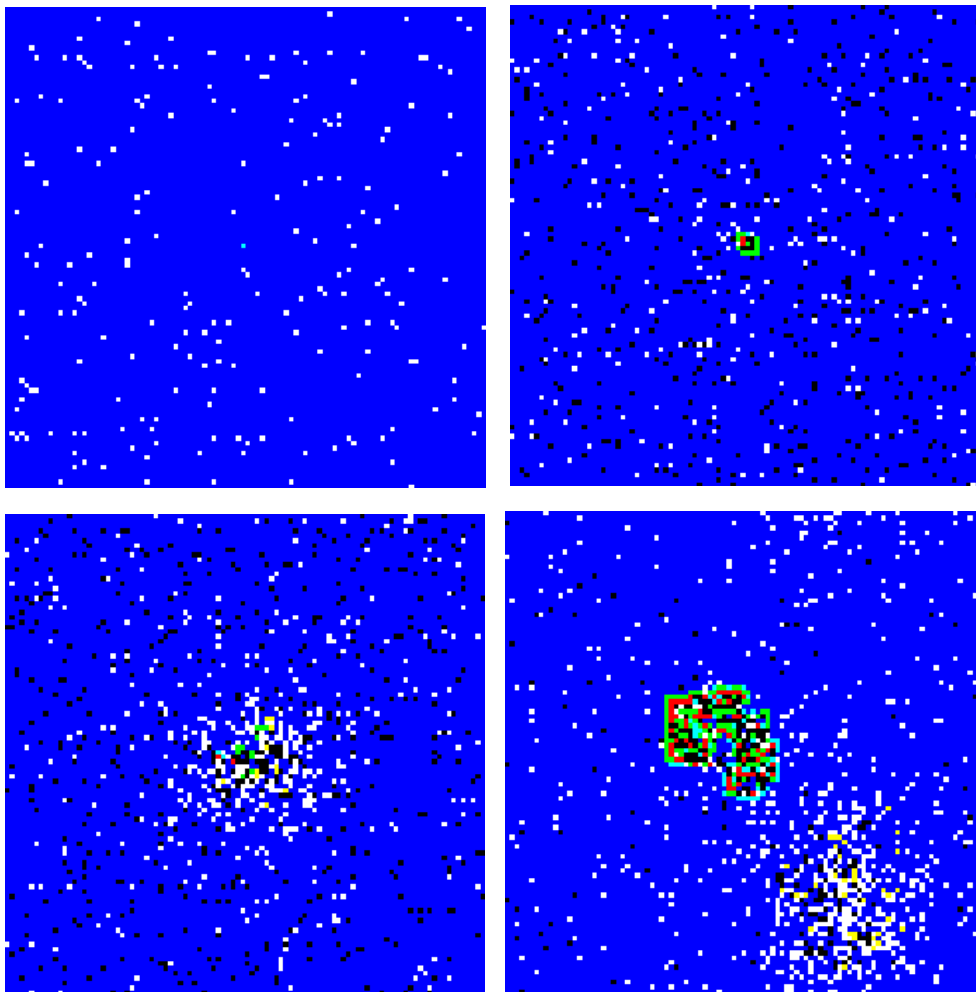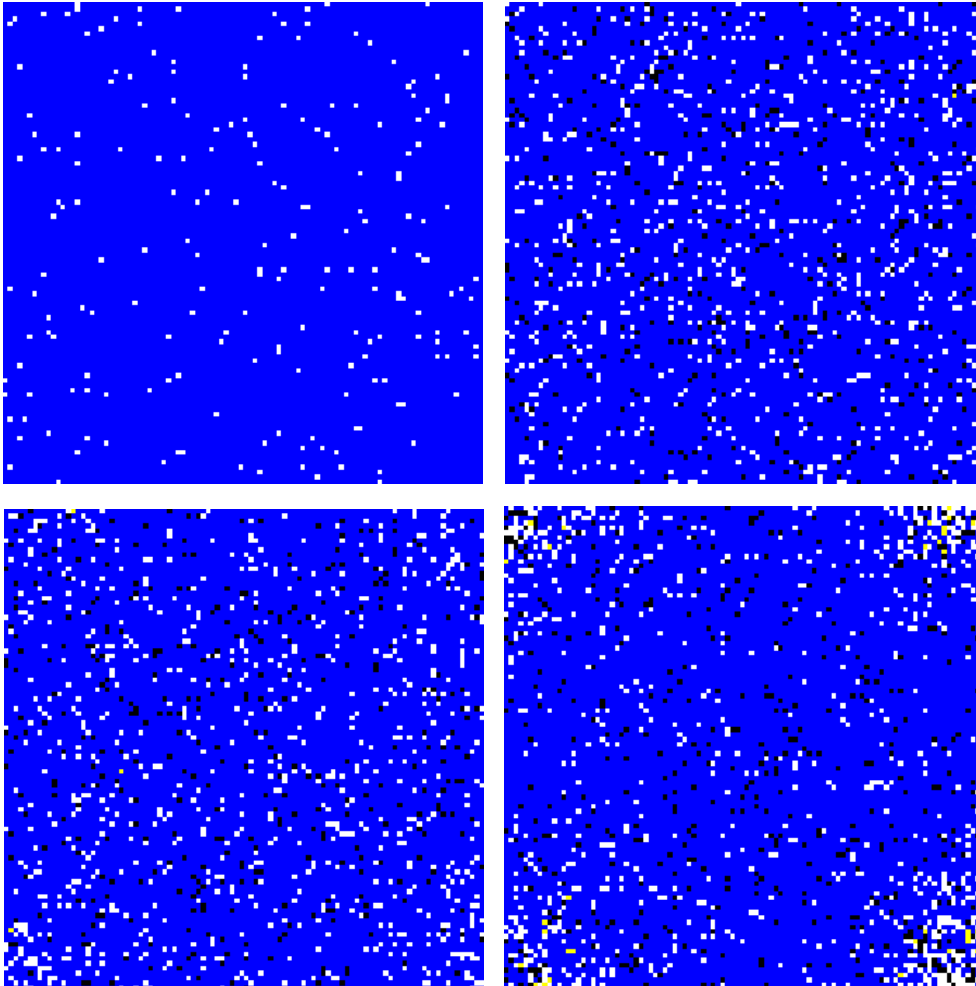
Figure 4.16 Simulation results of the CA model corresponding to the tissue injury outcome after 1 (top left), 60 (top right), 120 (bottom left), and 180 (bottom right) time steps. White: immune; Blue: healthy; Yellow: damage; Black: dead
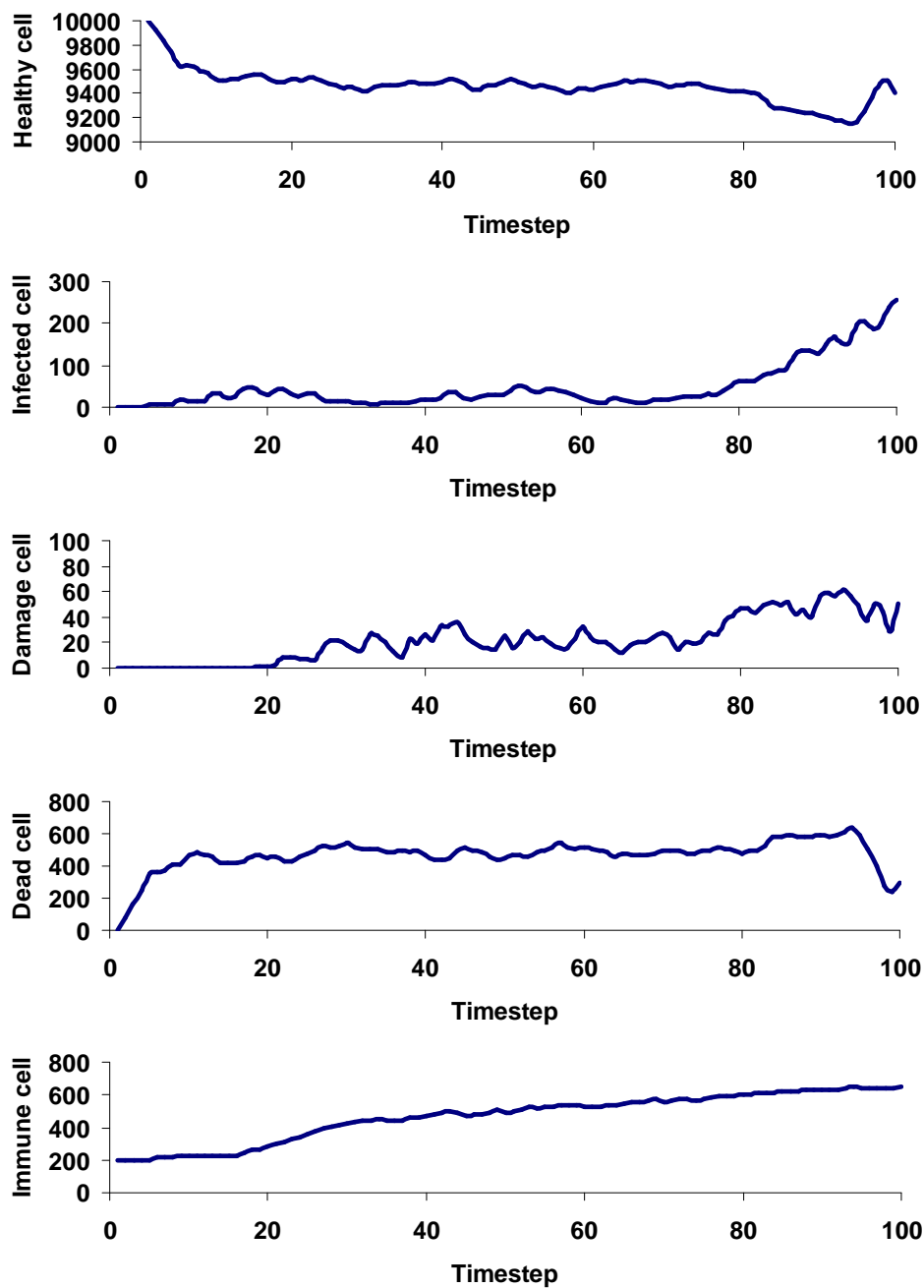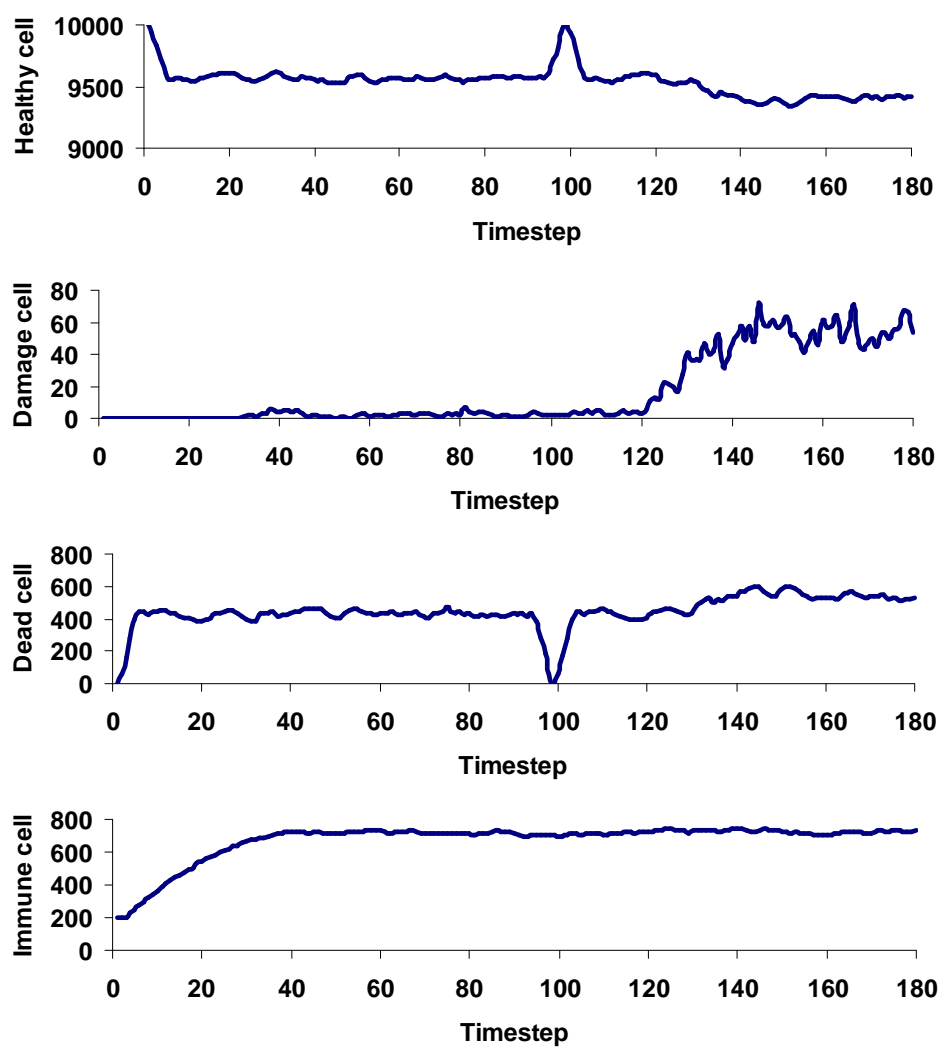
Figure 4.17 The number of healthy, damage, dead, and immune cells as a function of time step corresponding to the tissue injury outcome

The simulation has been performed to investigate the effect of strain level distributions on inflammatory responses. The strain level of 65% was applied on a square area of 40×40 cell^2, which was in the center of the lattice. There was no strain level on the rest of the lattices. The activated immune cells started concentrating in the area having the strain level with increasing time step. There was no concentration of the activated immune cells in the no-strain area. The concentration of the activated immune cells in the strain-level area caused more damage cells with increasing time step and eventually caused the tissue injury outcome (see Figure 4.18). The number of healthy, damage, dead, and immune cells as a function of time step is shown in Figure 4.19. As can be seen from this figure, the number of immune cells increased, reached a maximum level, and stayed at that level. This increase in immune cells caused damage cells to dramatically increase. However, the responses of this case was slower than the uniformly distribute case.
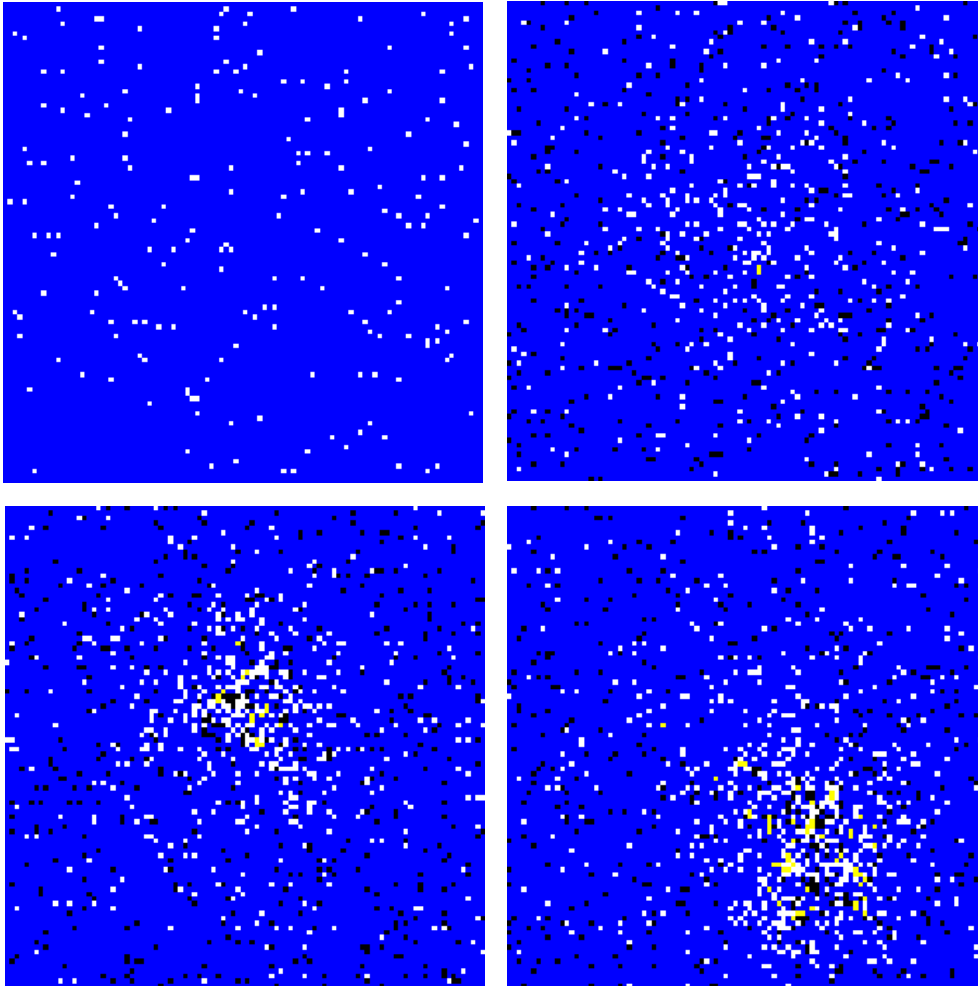
Figure 4.18 Simulation results of the CA model corresponding to the non-uniformly distributed strain level case after 1 (top left), 180 (top right), 230 (bottom left), and 300 (bottom right) time steps. White: immune; Blue: healthy; Yellow: damage; Black: dead

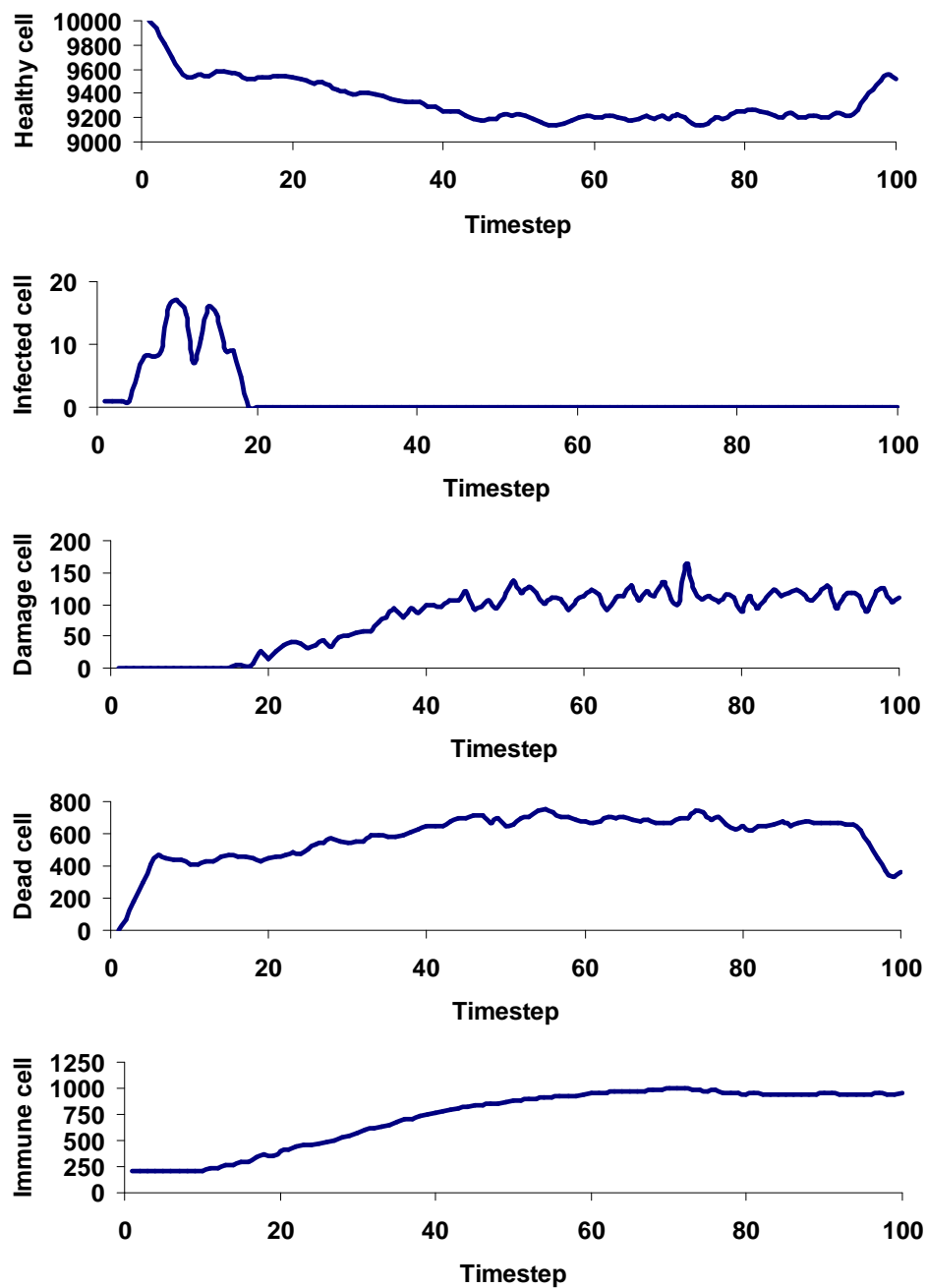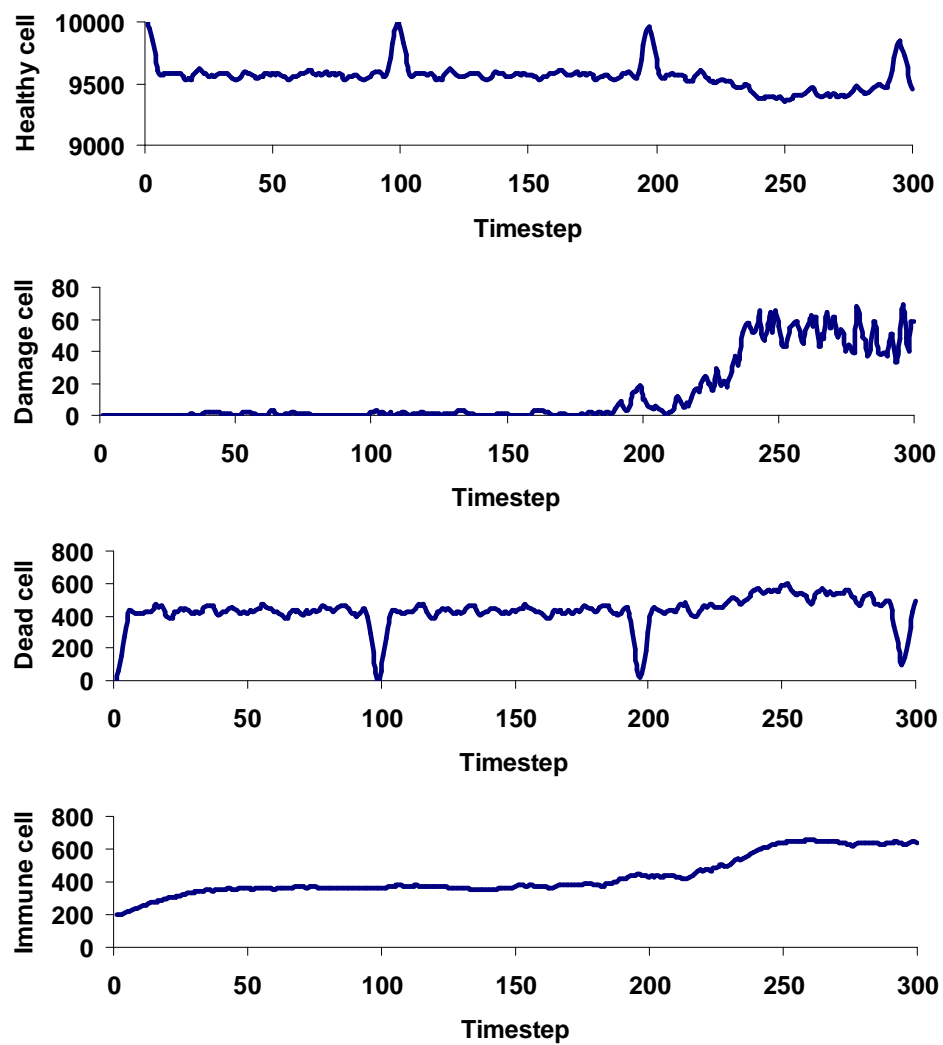Figure 4.19 The number of healthy, damage, dead, and immune cells as a function of time step corresponding to the non-uniformly distributed strain level case

4.5.3 <u>Effect of Strain Levels on Inflammatory Responses due to Pathogen</u>

Since the strain levels during mechanical ventilation can act synergistically with the inflammatory processes and increases inflammatory cell recruitment, neutrophils, through releasing of proinflammatory cytokines, e.g., interleukin (IL)-8 (Okada et al., 1998; Pugin et al., 1998; Pugin and Oudin, 2006; Vlahakis et al., 1999), the simulation has been carried out to investigate the effect of the strain levels on inflammatory responses due to pathogen. The strain levels of 0.5-66% were applied to the whole tissue and the ratio of P_{1I} to P_{1PH} was varied from 0.1-2.0. The possible outcomes are shown in Table 4.3. As can be seen from the table, high strain level caused the outcome to change from healthy to persistent non-infectious inflammation when the ratio of P_{1I} to P_{1PH} was lower than 1.2 and caused the outcome to change from persistent infectious inflammation to persistent non-infectious inflammation when the ratio of P_{1I} to P_{1PH} was higher than 1.2.

Table 4.3   The effect of strain levels from mechanical ventilation on inflammatory responses due to pathogen

P_{1I}/P_{1PH}	Strain levels	Outcome
	No strain	Healthy
Less than 1.2	Less than 52%	Healthy
	More than 52%	Persistent non-infectious inflammation
	No strain	Persistent infectious inflammation
More than 1.2	Less than 52%	Persistent infectious inflammation
	More than 52%	Persistent non-infectious inflammation

4.6 Discussion

The inflammatory responses are complex processes that include many immune cells and various cells within the injured tissues. Without the inflammation, the harmful stimuli cannot be removed and the healing process cannot be occurred. Many computational models based on ordinary differential equation (ODE) have been developed to better understand the inflammatory responses at the cellular level. However, when the inflammatory responses are described by ODE, the inflammatory responses are assumed to be homogeneous in space and the effect of spatial characteristics on inflammatory responses is neglected. In this chapter, the inflammatory responses at the cellular was developed using a discrete model, a cellular automata (CA). The inflammatory responses due to pathogen from the CA model were similar to those in

clinical situation and were qualitatively similar to those from the ODE model of the acute inflammation (Kumar et al., 2004) and the agent-based model of the acute inflammatory response (An, 2004) developed by other researchers.

The simulation results from the CA model for inflammatory responses due to strain levels confirmed the previous experiment that high strain levels from mechanical ventilation can cause tissue injury due to high concentration of activated immune cells that are attracted by increase in level of cytokine, IL-8 (Belperio et al., 2002). The simulation results also suggested the possible reason why there was no tissue injury at the upper airway and there was tissue injury at the lower airway and alveoli during mechanical ventilation in an animal model (Frank et al., 2002). The upper airway experienced low strain levels, which was not high enough to cause more inflammatory cells to migrate to the tissue. However, there were high strain levels at the lower airway generation. These high strain levels induced more inflammatory cells to migrate to the tissue. The cytotoxic mediators releasing by inflammatory cells can damage healthy epithelial cells and these damage epithelial cells in turn induced more inflammation (Jaeschke and Smith, 1997). The cellular-level model developed in this chapter could provide useful information about how strain levels from mechanical ventilation affects the inflammatory responses so that physicians can adjust each parameter appropriately during mechanical ventilation to prevent VALI.

4.7 Summary

The cellular-level model was developed in this chapter implementing the cellular automata (CA) model. Two species were considered: epithelial cell and immune cell. An epithelial cell was a stationary species and was represented by two-dimensional square lattice. An immune cell was a mobile species and can move throughout the lattice. The rules for the CA model were based on the previous experiments. The inflammatory responses due to pathogen and strain level were investigated using the CA model. The simulation results showed that the CA model can provide the outcome that have been seen in clinical practice and animal models. Healthy response due to pathogen can be obtained when the possibility that pathogen can penetrate into epithelial cells was very low. In contrast, persistent infectious inflammation responses occurred when the possibility that pathogen can penetrate into epithelial cells was very high. Persistent non-infectious inflammation responses occurred when the inflammatory responses were too strong and immuno-deficiency responses occurred when the inflammatory responses were too weak. High strain levels (more than 52%) can cause tissue injury without pathogen and can cause inflammatory responses due to pathogen to change from any condition to persistent non-infectious inflammation.

CHAPTER 5 Integration from Cells to Organ

5.1 Introduction

Inflammatory responses in the airway induced by mechanical ventilation are complex processes dealing with a length scale that ranges from ~ 1 nm for cytokine proteins to ~ 1 cm for the airway. Responses in one length scale highly depend on responses in another length scale. Airway displacements from the organ level affect the distributions of stresses and strains in the tissue level. These stresses and strains in the tissue level affect the level of proinflammatory cytokines (Pugin and Oudin, 2006) at the cellular level. The inflammatory responses at the cellular level, in turn, alter the mechanical properties of airway tissue in the tissue level; e.g., stiff smooth muscle layer in the asthma airway (Ma et al., 2002). The alteration of material properties of airway tissue leads to a change in material properties of the airway in the organ level. It is clear that no single model can cover a factor of 10^7 in a spatial scale. A practical approach is to develop many models that cover a limit range of the spatial scale and to develop a technique that links these models together to investigate airway inflammation induced by mechanical ventilation.

In this chapter the procedures for developing the multiscale model from the organ-level, tissue-level, and cellular-level models are described. Applications of the multiscale model of the airway for inflammatory responses during mechanical ventilation are demonstrated through case studies.

5.2 Multiscale Model of the Airways

The multiscale modeling framework developing in this research uses the organ-level model to drive inflammatory responses at the cellular level. The inflammatory responses from the cellular-level model, in turn, modulate changes in material properties at tissue and organ levels (see Figure 5.1). During each specific time step, the airway displacements at each location in the organ-level model are first determined by performing a finite element analysis with the FSI algorithm. The results of the airway displacements at each node of the organ-level model are then used to define the applied boundary conditions for the tissue-level model. Strains in each tissue layer are calculated employing the finite element analysis. These strains in each layer are then transferred to the cellular-level model. Change in the recruiting rate of the activated immune cells is associated with the transferred strains from the tissue-level model.

The number of healthy and damage cells from the cellular-level model, in turn, affects the material properties of the airway tissue at the tissue-level model. The changes in material properties at the tissue-level model are then transferred to the organ-level model. The airway displacements at each location in the organ-level model are then

determined using these new material properties. These procedures are repeated until the specific time period is reached.
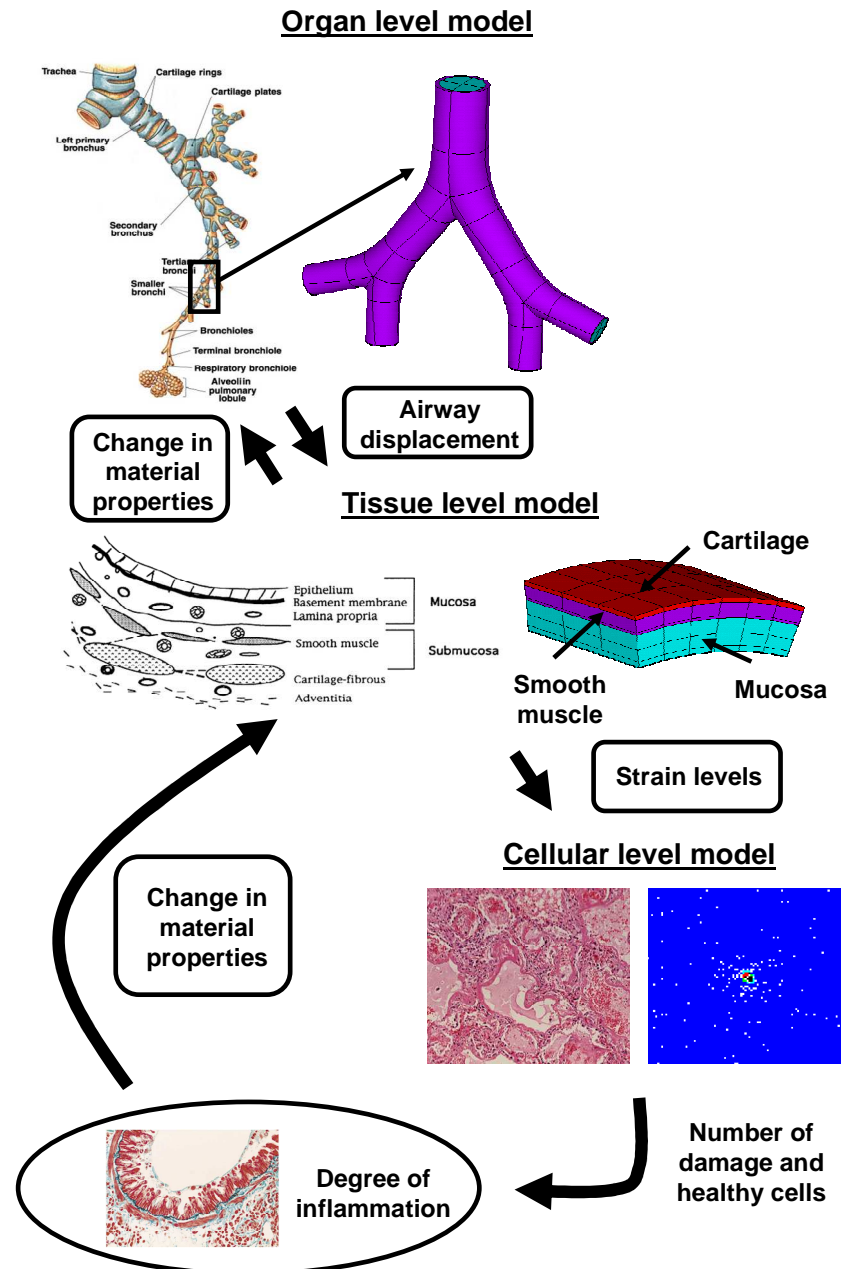
Figure 5.1   Multiscale modeling framework for airway inflammation induced by mechanical ventilation

5.3 Method of Analysis

The multiscale modeling framework described in the earlier section was employed to investigate inflammatory responses at the alveolar sac during mechanical ventilation. The simplified model of the alveolar sac illustrated in Chapter 2 was chosen for the analysis. The alveolar sac has a diameter of 500 μm (see Figure 5.2). The alveolar duct diameter was 200 μm and the entrance length was 100 μm (Dailey and Ghadiali, 2007). Thickness of the alveolar sac is 0.3 μm (Lumb, 2005). The alveolar sac was assumed to be homogeneous and isotropic material with the Young's modulus of 80 kPa (Yamada, 1970) and Poisson's ratio of 0.45 (Prakash and Hyatt, 1978). The alveolar sac is composed mainly of a single layer of an alveolar epithelium. For this reason, the tissue-level model for the alveolar sac consisted of only one layer of the alveolar epithelium. The Young's modulus of elasticity of the alveolar wall was 80 kPa (Yamada, 1970) and Poisson's ratio was 0.45 (Prakash and Hyatt, 1978). The boundary conditions at the tissue-level model were airway displacements at each location from the organ-level model. The strain levels in the epithelial layer from the tissue-level model are then used to study inflammatory responses at the cellular level. The cellular automata (CA) model for inflammatory responses due to strain levels were implemented using MATLAB. The simulation was performed on a lattice of 44×44 sites which represented a tissue area of 0.88×0.88 mm^2 (Segovia-Juarez et al., 2004), a total surface area of the simplified alveolar sac model. The initial population of immune cells was 40 cells. This value represents the normal level of immune cells in our body (Segovia-Juarez et al., 2004).

The periodic boundary conditions were used for the simulation. The initial conditions for the CA model were randomly placed immune cells. Only one immune cell can occupy one lattice site. Each epithelial cell was randomly assigned its lifespan. The simulations were carried out with the following physiological assumptions: 1) only healthy epithelial cells are able to divine and 2) Strain levels do not affect inactivated immune cells.

The ratio of the number of damage cells to healthy cells was obtained through the CA model of cellular inflammatory responses. This ratio, in turn, affected the change in the Young's modulus of elasticity of the alveolar sac tissue. The stiffness for the injured tissue was about 25% less than that of the normal tissue (Makhsous et al., 2006). The decrease in the stiffness of the injured tissue was assumed to be proportional to the ratio of the number of damage cells to healthy cells. The simulations were carried out to investigate the cellular inflammatory responses during mechanical ventilation. The time steps for the organ- and cellular-level models were 0.5 s and 4 h, respectively. The coupling time between the organ-level, tissue-level, and cellular-level models was 4 h. Figure 5.2 shows the computational domains and exchanging information between the organ-, tissue-, and cellular-level models for an investigation of inflammatory responses at the alveolar sac during mechanical ventilation.

Organ level model

{Interface #1}

Airway displacement

Change in material properties

Tissue level model

Alveolar epithelium

{Interface #2}

Strain levels

Cellular level model

Change in material properties

Number of damage and healthy cells

Degree of inflammation
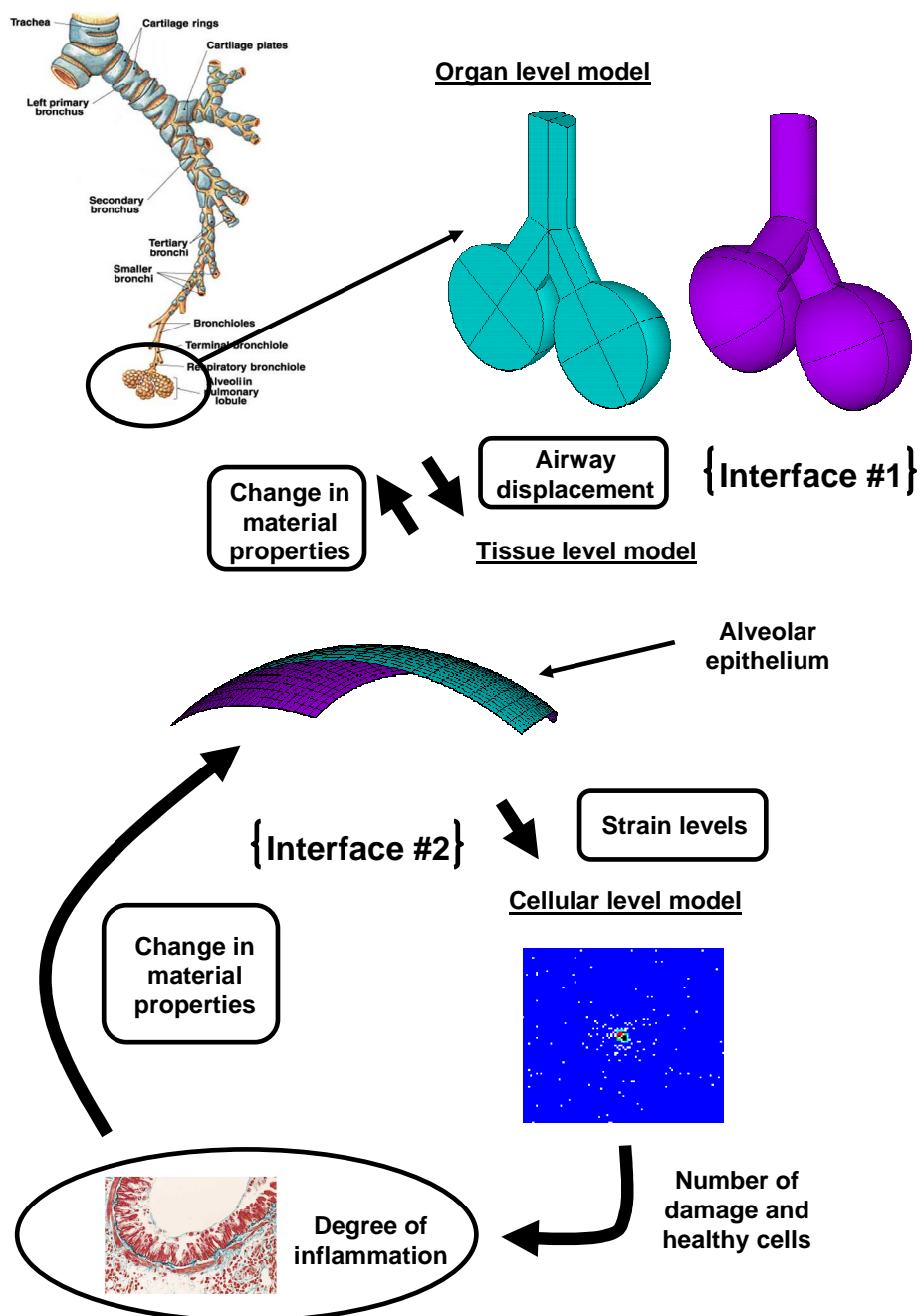
Figure 5.2   A schematic diagram of the multiscale model of inflammatory responses at the alveolar sac during mechanical ventilation based on the multiscale modeling framework

The simulations were carried out to investigate inflammatory responses at the alveolar sac during mechanical ventilation. Due to computational intensive, the simulations were performed until 100 iterations of coupling time, about 400-h real time. The flow waveform from mechanical ventilation was a constant flow waveform with flow rate of 60 l/min. Three different mechanical ventilation settings were chosen for the analyses. The first setting was 1400-cc tidal volume during mechanical ventilation (1400cc case). The second setting was 700-cc tidal volume during mechanical ventilation (700cc case). For the 1400- and 700-cc tidal volume settings, the simulations were performed until 100 iterations of coupling time with the constant tidal volume. The last setting was tidal volume of 1400 cc for 60 iterations of coupling time and then switched to 700-cc tidal volume for 40 iterations of coupling time (1400/700cc case). Figure 5.3 shows the different flow waveforms that were used for the analyses.
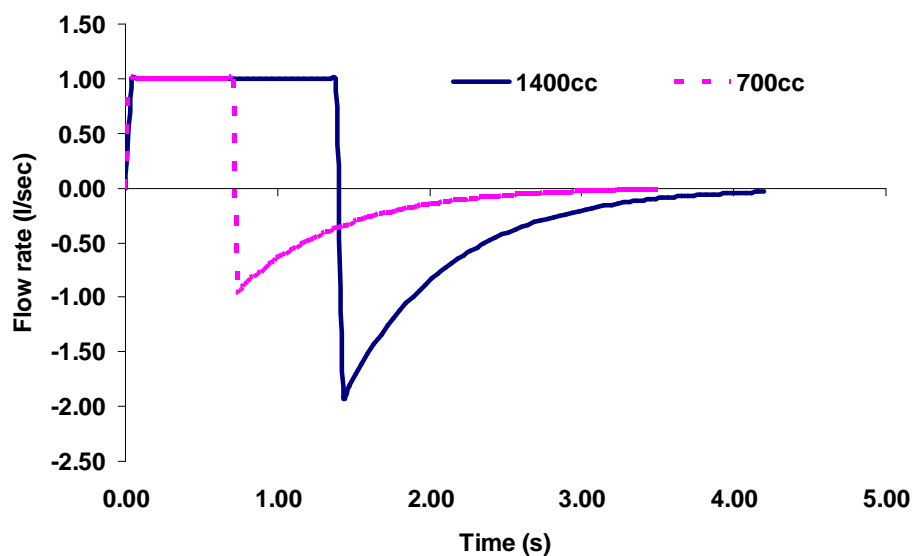
Figure 5.3   The flow waveforms that were used for the analyses of cellular inflammatory responses at the alveolar sac during mechanical ventilation through the multiscale modeling framework

5.4 Results

Figure 5.4 shows inflammatory responses at the alveolar sac during mechanical ventilation for the 1400cc case. The number of immune cells increased with increasing time step due to the strain levels from mechanical ventilation. This increase in activated immune cells damaged healthy cells. These damage cells in turn induced more activated immune cells and these activated immune cells caused more damage cells. The number of healthy, damage, dead, immune cells, and strain levels as a function of time step is shown in Figure 5.5. As can be seen from this figure, the number of immune cells increased with increasing time step. This increase in immune cells caused damage cells to dramatically

increase. This increase in damage cells increased the strain levels in the alveolar sac because the tissue was less stiff during the injury. The high strain levels, in turn, induced more activated immune cells.
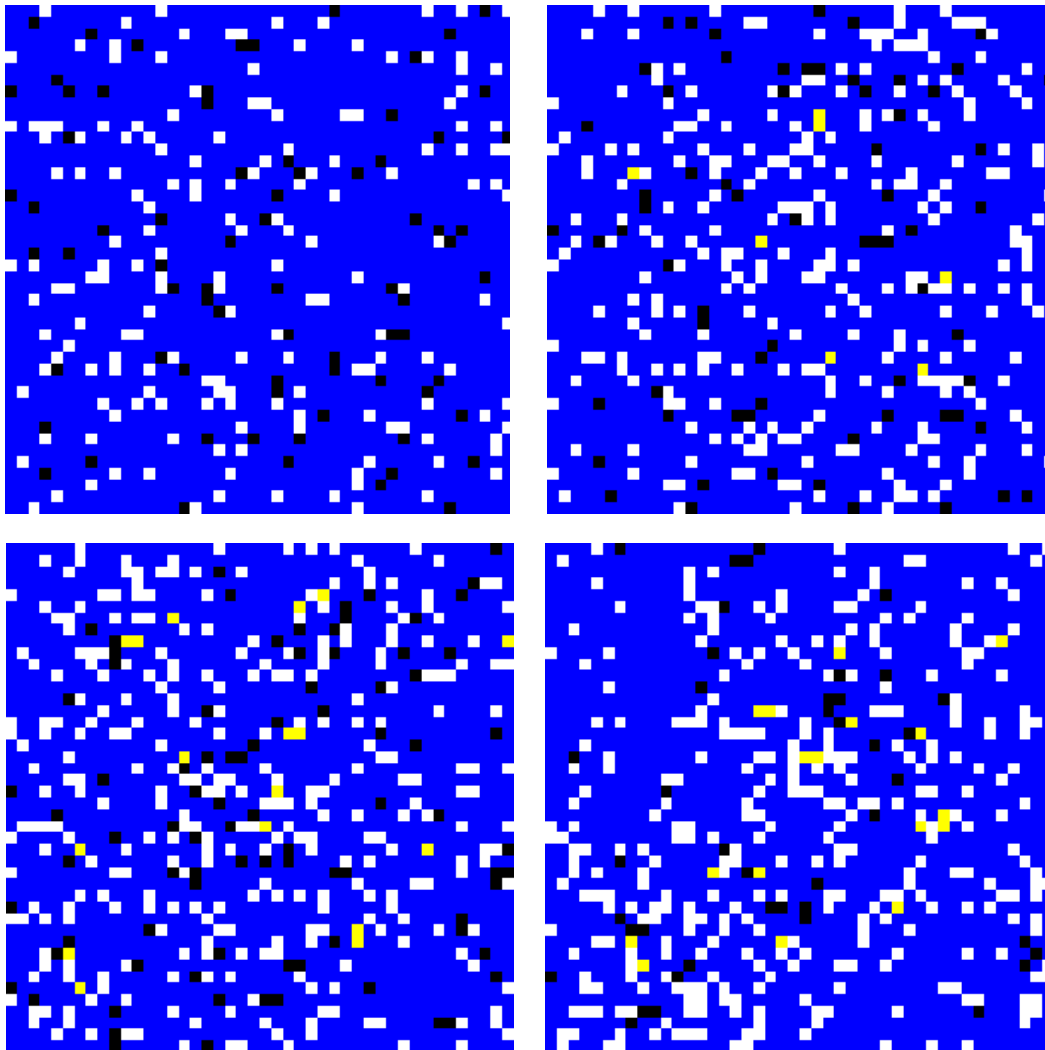
Figure 5.4   Simulation results of the cellular inflammatory responses at the alveolar sac during mechanical ventilation for the 1400cc case after 20 (top left), 50 (top right), 80 (bottom left), and 100 (bottom right) time steps. White: immune; Blue: healthy; Yellow: damage; Black: dead
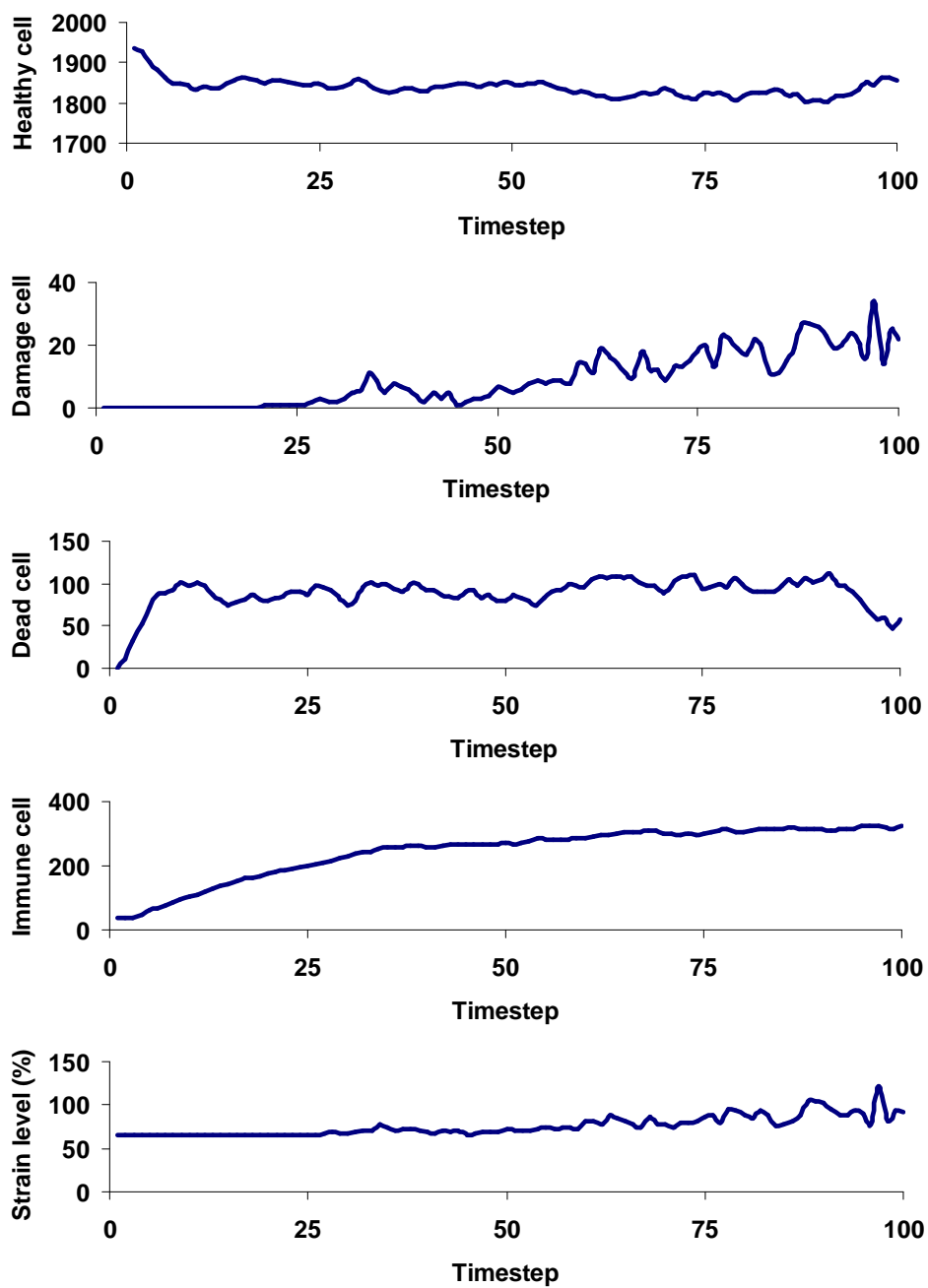
Figure 5.5   The number of healthy, damage, dead, immune cells, and strain levels as a function of time step for the 1400cc case

Figure 5.6 shows inflammatory responses at the alveolar sac during mechanical ventilation for the 700cc case. The number of immune cells increased with increasing time step due to the strain levels from mechanical ventilation. This increase in activated immune cells caused a small number of damage cells. As time step increased the immune cells can digest all damage cells and the tissue returned to the healthy state. The number of healthy, damage, dead, immune cells, and strain levels as a function of time step is shown in Figure 5.7. As can be seen from this figure, the number of immune cells increased, reached a maximum value, and stayed at that level with increasing time step. The maximum level of the immune cells for this case was about two times less than that of the 1400cc case. This maximum level of immune cells was not high enough to cause a high number of damage cells. As the time step increased, there was no damaged cell in the tissue. In contrast to the 1400cc case, the strain levels insignificantly increased during mechanical ventilation.
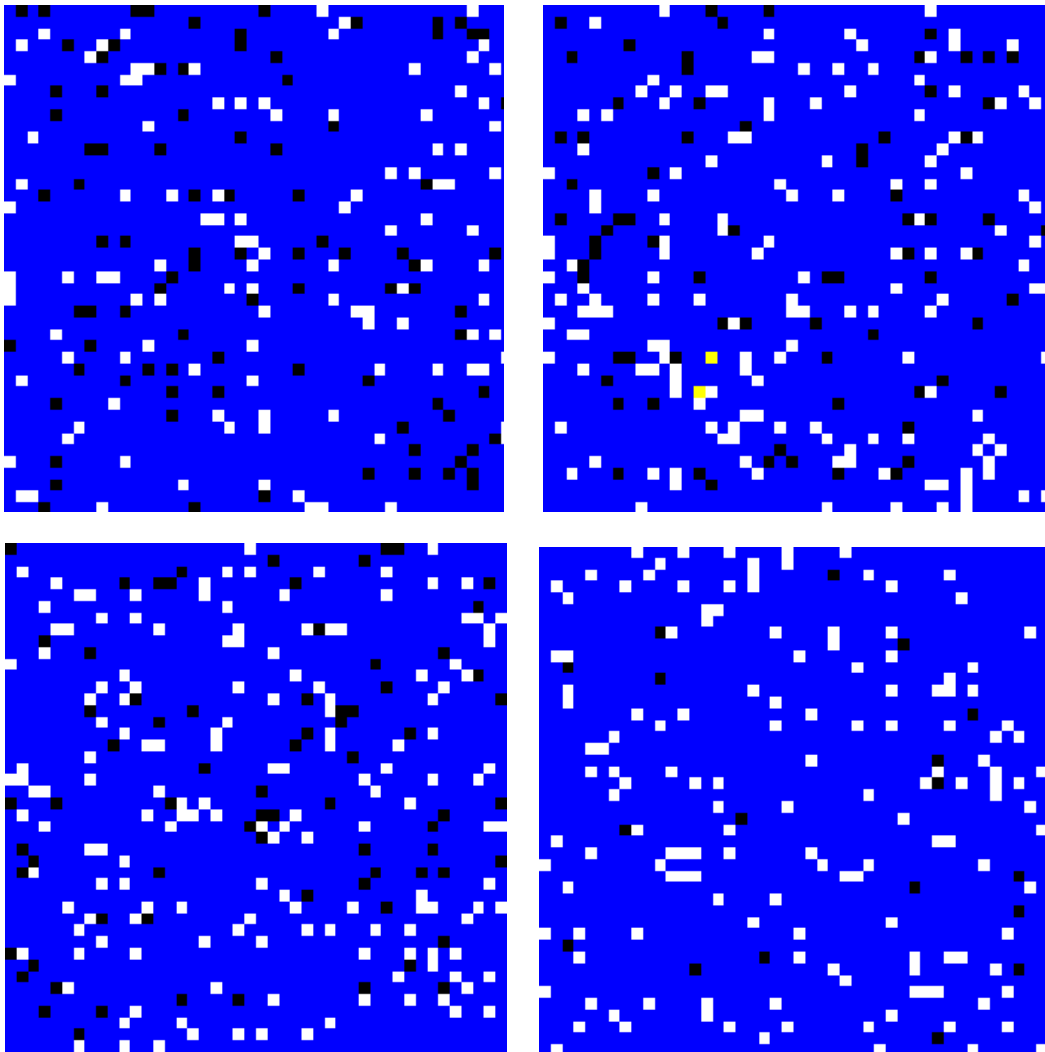
Figure 5.6   Simulation results of the cellular inflammatory responses at the alveolar sac during mechanical ventilation for the 700cc case after 20 (top left), 50 (top right), 80 (bottom left), and 100 (bottom right) time steps. White: immune; Blue: healthy; Yellow: damage; Black: dead
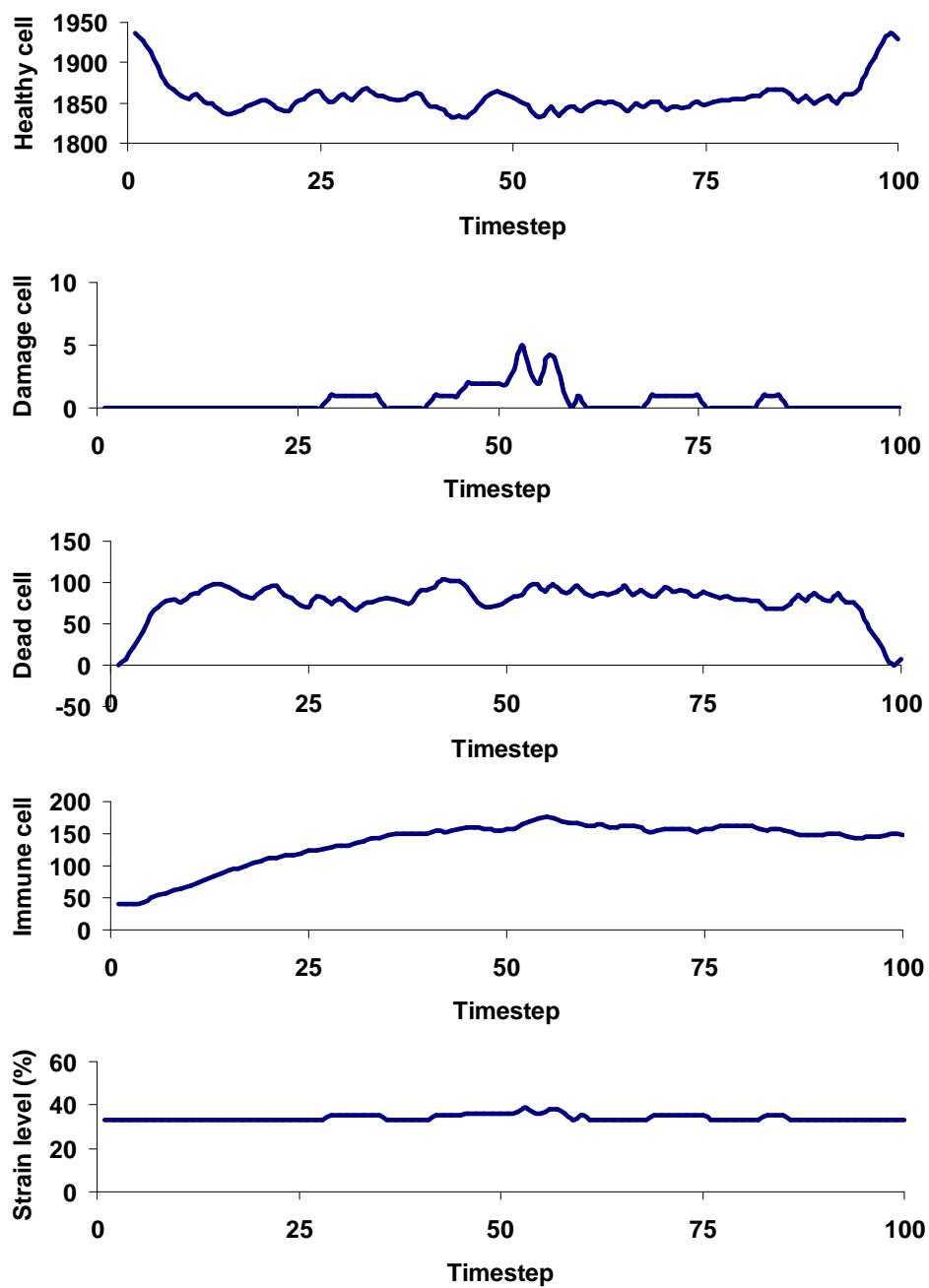
Figure 5.7   The number of healthy, damage, dead, immune cells, and strain levels as a function of time step for the 700cc case

Figure 5.8 shows inflammatory responses at the alveolar sac during mechanical ventilation for the 1400/700cc case. The number of immune cells increased with increasing time step due to the strain levels from mechanical ventilation until the 60th time step. This increase in activated immune cells caused more damage cells. As the time step were greater than 61, the strain levels from mechanical ventilation decreased. For this reason, the number of the activated immune cells in the tissue decreased. As time step increased, the immune cells can digest all damage cells and the tissue returned to the healthy state. The number of healthy, damage, dead, immune cells, and strain levels as a function of time step is shown in Figure 5.9. As can be seen from this figure, the number of immune cells increased with increasing time step until the 60th time step. This increase in immune cells caused damage cells to dramatically increase. However, when the time step was greater than 61, the number of immune cell started decreasing. This reduced the number of damage cells. As the time step increased, there was no damaged cell in the tissue. This result was similar to the 700 cc case. However, there are two different levels of the strain levels for this case. Table 5.1 shows summary of the simulation results of the case studies for two different mechanical ventilation settings.
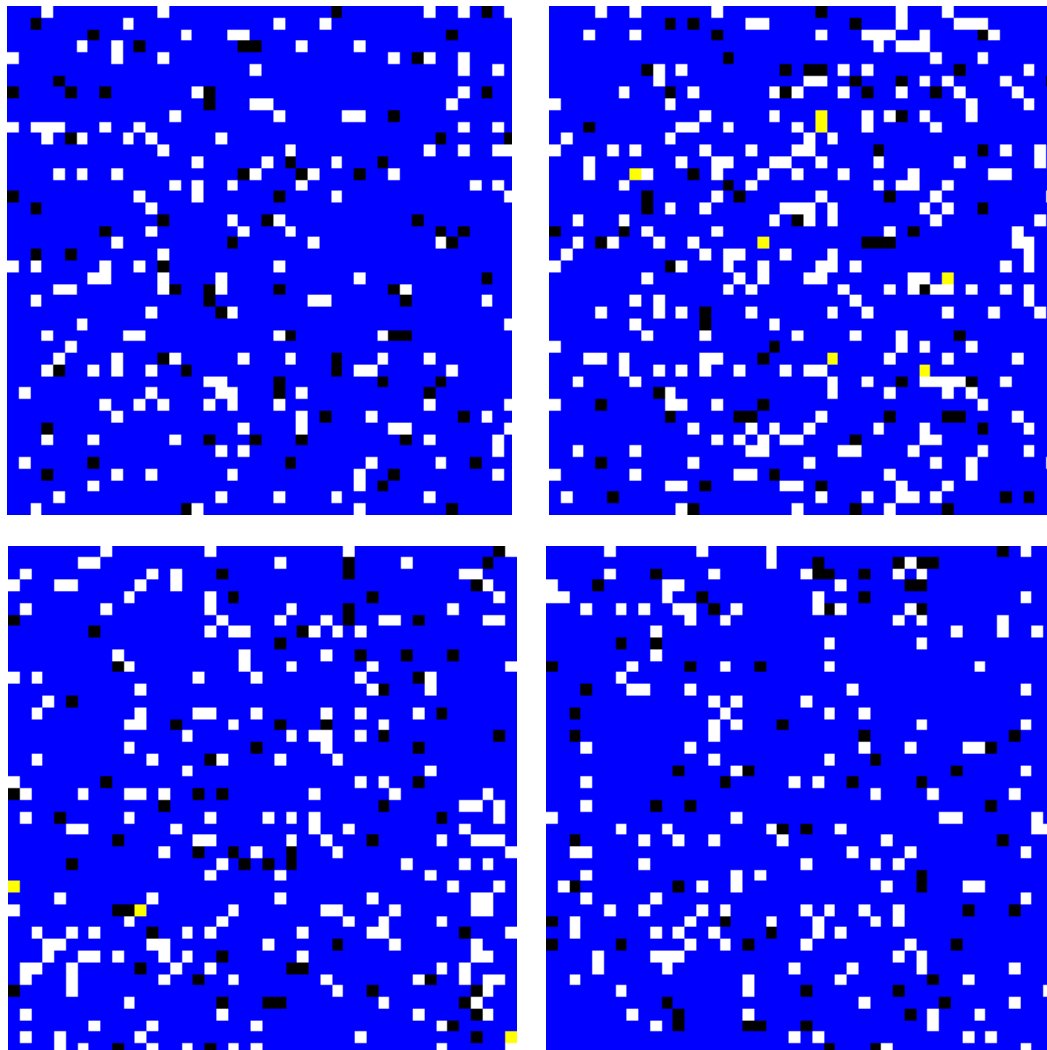
Figure 5.8   Simulation results of the cellular inflammatory responses at the alveolar sac during mechanical ventilation for the 1400/700cc case after 20 (top left), 50 (top right), 80 (bottom left), and 100 (bottom right) time steps. White: immune; Blue: healthy; Yellow: damage; Black: dead
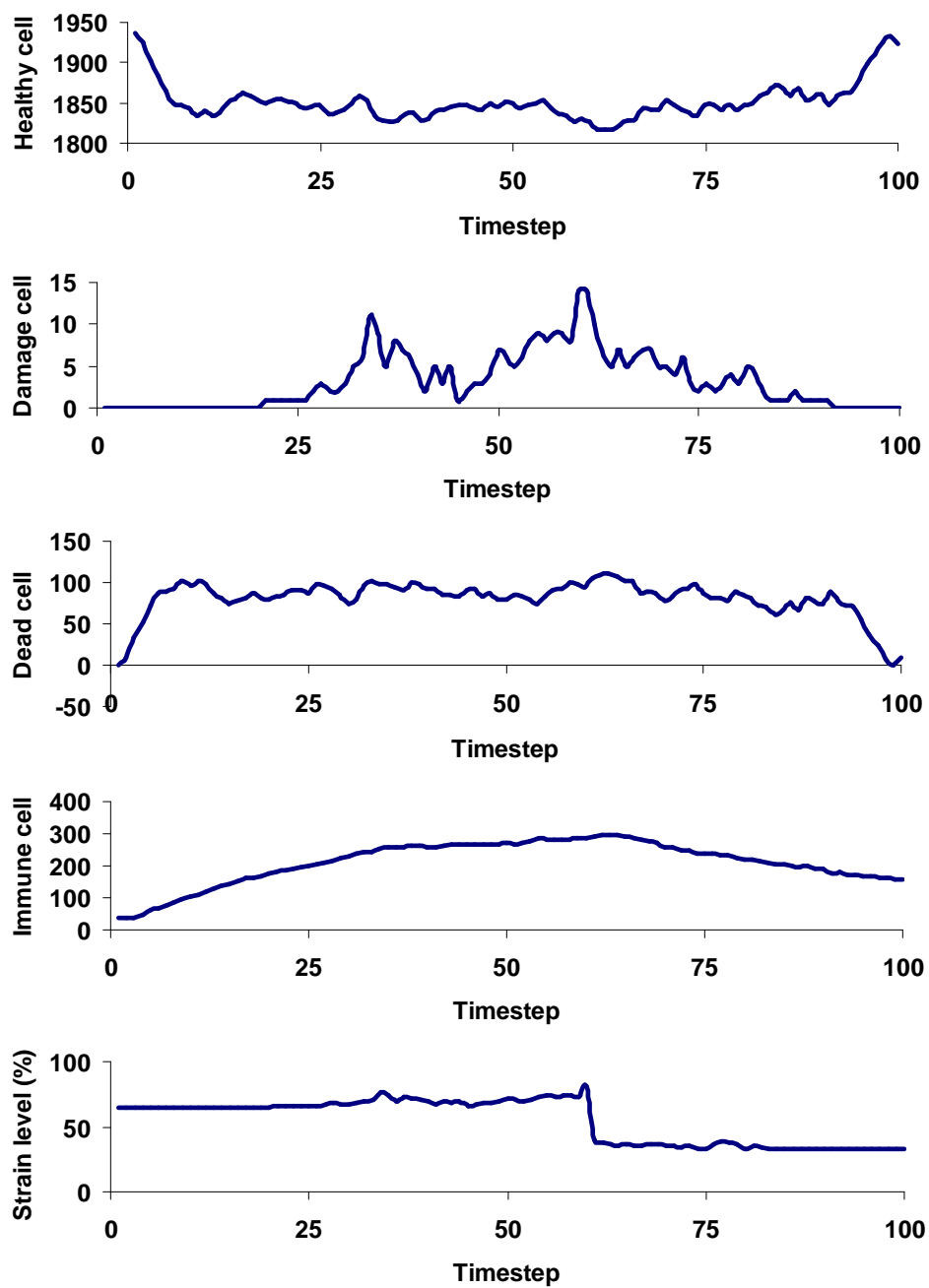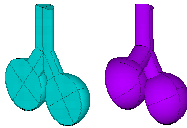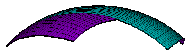
Figure 5.9   The number of healthy, damage, dead, and immune cells as a function of time step for the 1400/700cc case

Table 5.1   Summary of the simulation results from the multiscale model of the airway inflammation induced by mechanical ventilation for different mechanical ventilation settings

Level	Input	Output	Significance	Remarks
Organ	Case 1: airflow rate of 60 l/min with 1400-cc tidal volume	55% maximum von Mises strain, 21% maximum 1st principal strain, 25% maximum 2nd principal strain, 45% 3rd principal strain, and 20% change in sac diameter; Previous studies by Sinclair et al (2007) in the airway diameter of 200-2500 μm showed that maximum circumferential strains were in the ranges of 15-65%	Might cause tissue injury due to high strain levels (see cellular level)	Specific to this geometry, in general this might be different when the whole alveoli is considered (need further studies)
	Case 2: airflow rate of 60 l/min with 700-cc tidal volume	27% maximum von Mises strain, 10% maximum 1st principal strain, 12% maximum 2nd principal strain, 22% 3rd principal strain and 10% change in sac diameter	Not expected to cause tissue injury (see cellular level)	

Level	Input	Output	Significance	Remarks
Tissue	Case 1: airway displacement from the organ level and material properties of each layer from previous experiments	55% maximum von Mises strain in the epithelial layer	Might cause tissue injury/damage (see cellular level)	Further studies on the effect of geometry and viscoelasticity property are needed
	Case 2: airway displacement from the organ level and material properties of each layer from previous experiments	27% maximum von Mises strain in the epithelial layer	Not expected to cause tissue injury (see cellular level)	
Cellular	Case 1: strain levels from the tissue level and CA rules based on previous experiments	Ratio of damage to healthy cells was about 0.6-1.8%	Might cause tissue injury due to high concentration of activate immune cells	Need to correlate the strain level with degree of inflammation and tissue properties
	Case 2: strain levels from the tissue level and CA rules based on previous experiments	Ratio of damage to healthy cells was about 0.05-0.22%	Not expected to cause tissue injury	

5.5 Discussion

The multiscale modeling framework was developed in this chapter. The airway displacements from the organ-level model were transferred to the tissue-level model for

strain distributions in each airway layer. The strain levels in the epithelial layer from the tissue-level model were then transferred to the cellular-level model for inflammatory responses due to strain levels. The injury at the cellular level, in turn, modulated change in material properties of the tissue at the tissue and organ levels. This multiscale modeling framework was employed to study cellular inflammatory responses at the alveolar sac during mechanical ventilation. The simplified model of the alveolar sac was chosen for the study. Three different mechanical ventilation settings were employed to investigate the effect of tidal volume on inflammatory responses at the alveolar sac. The simulation results supported the clinical practice that high tidal volume can cause ventilator-associated lung injury (VALI) at the alveolar sac due to high level of activated immune cells (Belperio et al., 2002; Chiumello et al., 1999). Low tidal volume can prevent VALI and VALI can also be prevented by switching from high tidal volume to low tidal volume ventilation. Not only did high tidal volume cause VALI due to high level of activated immune cells, it might also cause rupture of the tissue since its strength is about 40% less than the healthy tissue (Cleak and Eston, 1992; Howell et al., 1993; Ito et al., 2005). The mutiscale model of the airway developed in this chapter can be used to study the effect of other mechanical ventilation settings on the cellular inflammatory responses at other locations in the respiratory airway. Clinicians can use this information to appropriately determine the parameters during mechanical ventilation to prevent or mitigate VALI.

5.6 Summary

The framework for developing a multiscale model of the airway was described. The multiscale model of the airway consists of the organ-level, tissue-level, and cellular-level models. This multiscale model of the airway was employed to study inflammatory responses at the alveolar sac during mechanical ventilation. The simplified model of the alveolar sac was chosen for the analysis. Three different mechanical ventilation settings were employed as case studies. The airway displacements from the organ-level model were transferred to the tissue-level model for distributions of strain levels. The strain levels in the epithelial layer from the tissue-level model were then transferred to the cellular-level model for inflammatory responses due to strain levels. The injury at the cellular level, in turn, modulated change in material properties of the tissue at the tissue and organ levels. The simulation results showed that high tidal volume (1400 cc) during mechanical ventilation can cause tissue injury due to high concentration of activated immune cells and low tidal volume during mechanical ventilation (700 cc) can prevent tissue injury during mechanical ventilation and can mitigate tissue injury from the high tidal volume ventilation. The information obtained from this multiscale model could provide useful information on VALI and the new ventilation strategy could be developed to prevent VALI.

CHAPTER 6 Conclusions and Recommendations

6.1 Conclusions

6.1.1 Organ-Level Models

- Airflow velocity increases with increasing airflow rate from mechanical ventilation and airway constriction due to airway diseases
- Airway pressure increases with increasing airflow rate, tidal volume, and PEEP from mechanical ventilation
- Airway strains increase with increasing airflow rate, tidal volume, and PEEP form mechanical ventilation; however, they decrease in airway constriction from asthma.
- Sine waveform provides the highest airflow velocity and airway pressure while descending waveform provides the lowest airway pressure and airway strains

6.1.2 Tissue-Level Models

- The homogeneous material model overestimates the maximum strain in the mucosa layer about 11%; however the homogeneous material model underestimates the maximum strain in the smooth muscle and cartilage layers about 12% and 16%, respectively

6.1.3 Cellular-Level Models

- Healthy response due to pathogen can be obtained when the possibility that pathogen can penetrate into epithelial cells is very low

- Persistent infectious inflammation response occurs when the possibility that pathogen can penetrate into epithelial cells is very high

- Persistent non-infectious inflammation response occurs when the inflammatory responses due to pathogen are too strong

- Immuno-deficiency response occurs when the inflammatory responses due to pathogen are too weak

- High strain levels (more than 52%) can cause tissue injury without pathogen and can cause inflammatory responses due to pathogen to change from any condition to persistent non-infectious inflammation

6.1.4 Integration from Cells to Organ

- High tidal volume (1400 cc) during mechanical ventilation can cause tissue injury at the alveolar sac due to high concentration of activated immune cells

- Low tidal volume during mechanical ventilation (700 cc) can prevent tissue injury at the alveolar sac during mechanical ventilation

- Low tidal volume during mechanical ventilation (700 cc) can mitigate tissue injury occurring from the high tidal volume (1400 cc).

6.2 Scientific Contributions

This research indicates the beginning of the new field in mechanical ventilation by combining advances in engineering simulation techniques with clinical applications. The information from the research will bridge a gap between engineering and clinical applications. Physicians will better understand which factors affect inflammatory responses during mechanical ventilation and can provide appropriate ventilation parameters to prevent ventilator-associated lung injury (VALI) and reduce mortality rates in patients with acute respiratory distress syndrome (ARDS) or other airway diseases during mechanical ventilation.

The research is a state-of-the-art since there has never been a study of fluid characteristics (airflow velocity, airway pressure, and wall shear stress) and strain levels in human respiratory airways during mechanical ventilation through fluid-structure interaction (FSI) algorithm. The organ-level model that incorporates the interactions

between airflow and the airway wall will provide a computational framework for other studies of fluid characteristics in human respiratory airways. The patterns of flow field in the airways are very useful for studying particle deposition in the airways for many applications ranging from aerosol drug therapy to inhalation toxicology. In addition, the tissue-level model can illustrate how strain levels from mechanical ventilation distribute in each layer of the airway and demonstrate the important of material models on the distributions of strain levels. The computational model for other tissue can be developed implementing the same technique for the tissue-level model developed in this research. Lastly, the cellular inflammatory responses due to strain levels also provide other researchers better understanding the inflammatory responses in the airway tissue and effects of strains on the inflammatory responses. The clinicians can use this useful information to appropriately adjust mechanical ventilation parameters to prevent VALI.

The multiscale model can also be used to study the inflammatory responses in the airways from particle deposition (see Figure 6.1). The organ-level model is solved to obtain locations of particle deposition in the airways. The flow waveforms for the organ-level model can be breathing patterns during sedentary/light/heavy activity or those during employing an inhaler. The locations and concentrations of the particle are then transferred to the cellular-level model. The inflammatory parameters in the cellular-level model can be based on the concentrations and types of the particle.
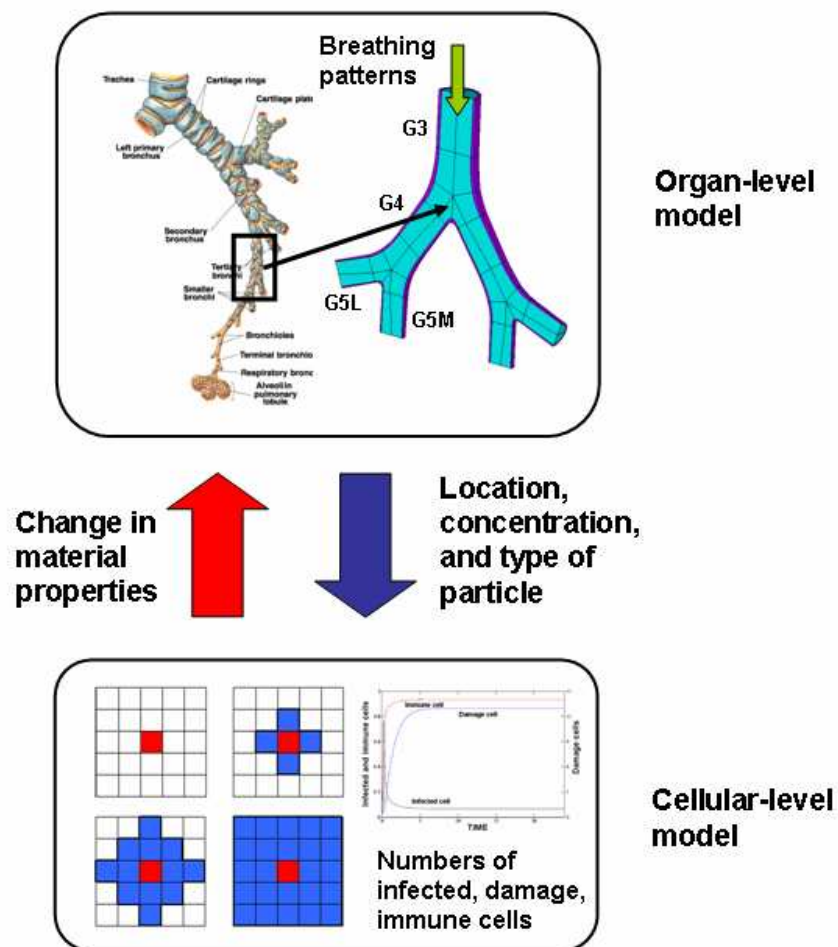
Figure 6.1   Procedures for using the developed multiscale modeling framework for airway inflammation induced by paticle deposition

6.3 Recommendations

The multiscale modeling framework developed in this research shows the feasibility of the method for an investigation of inflammatory responses during mechanical ventilation. However, the computational models for the organ, tissue, and

cellular levels were developed with some assumptions. To increase an accuracy of the multiscale of the airway for inflammatory responses during mechanical ventilation, the further studies are need. The recommended future work is as follows.

- The geometry of the organ- and tissue-level models was based on idealized models of the airway and alveolar sac. The more realistic model is recommended in order to obtain more accurate fluid characteristics and airway strains during mechanical ventilation

- The Young's moduli of elasticity for the organ- and tissue-level models were assumed to be linear. Further study is needed to investigate the effect of nonlinear material properties on fluid characteristics and airway strains during mechanical ventilation

- Due to a limitation of the software that cannot account for large deformation, the simulation results of the alveolar sac at the organ level were obtained through one way fluid-structure interaction (FSI). The effect of the type of the FSI algorithm on the results of the alveolar sac is needed to further investigate.

- During mechanical ventilation, physicians must balance between a gas exchange process and tidal volume to prevent VALI. To develop a better strategy to mechanically ventilate patients, the gas exchange process should be incorporated into the multiscale model of the airway.

List of References

List of References

An G, 2004. *In silico* experiments of existing and hypothetical cytokine-directed clinical trials using agent-based modeling. Critical Care Medicine 32, 2050-2060.

ANSYS 2005 *ANSYS 10.0 User Guide* ANSYS Inc., Canonsburg, PA

Bai A, Eidelman D H, Hogg J C, James A L, Lambert R K, Ludwig M S, Martin J, Mcdonald D M, Mitzner W A, Okazawa M, Pack R J, Pare P D, Schellenberg R R, Tiddens H A W M, Wagner E M, and Yager D, 1994. Proposed Nomenclature for Quantifying Subdivisions of the Bronchial Wall. Journal of Applied Physiology 77, 1011-1014.

Barbero E J 1999 *Introduction to Composite Materials Design* Taylor & Francis, Inc., Philadelphia, PA

Beauchemin C, Samuel J, and Tuszynski J, 2005. A simple cellular automaton model for influenza A viral infections. Journal of Theoretical Biology 232, 223-234.

Behrendt C E, 2000. Acute respiratory failure in the United States: Incidence and 31-day survival. Chest 118, 1100-1105.

Belperio J A, Keane M P, Burdick M D, Londhe V, Xue Y Y, Li K, Phillips R J, and Strieter R M, 2002. Critical role for CXCR2 and CXCR2 ligands during the pathogenesis of ventilator-induced lung injury. Journal of Clinical Investigation 110, 1703-1716.

Benayoun L, Druilhe A, Dombret M, Aubier M, and Pretolani M, 2003. Airway Structural Alterations Selectively Associated with Severe Asthma. American Journal of Respiratory and Critical Care Medicine 167, 1360-1368.

Brackel H J L, Pedersen O F, Mulder P G H, Overbeek S E, Kerrebijn K F, and Bogaard J M, 2000. Central Airways Behave More Stiffly during Forced Expiration in Patients with Asthma. American Journal of Respiratory and Critical Care Medicine 162, 896-904.

Brouns M, Jayaraju S T, Lacor C, Mey J D, Noppen M, Vincken W, and Verbanck S, 2007. Tracheal Stenosis: A Flow Dynamics Study. Journal of Applied Physiology 102, 1178-1184.

Brown N J, Salome C M, Berend N, Thorpe C W, and King G G, 2007. Airway Distensibility in Adults with Asthma and Healthy Adults, Measured by Forced Oscillation Technique. American Journal of Respiratory and Critical Care Medicine 176, 129-137.

Chiumello D, Pristine G, and Slutsky A S, 1999. Mechanical Ventilation Affects Local and Systemic Cytokines in an Animal Model of Acute Respiratory Distress Syndrome. American Journal of Respiratory and Critical Care Medicine 160, 109-116.

Choe M M, Sporn P H S, and Swartz M A, 2003. An in vitro airway wall model of remodeling. American Journal of Physiology: Lung Cellular and Molecular Physiology 285, L427-L433.

Cleak M J and Eston R G, 1992. Muscle soreness, swelling, stiffness and strength loss after intense eccentric exercise. British Journal of Sports Medicine 26, 267-272.

Croteau J R and Cook C D, 1961. Volume-pressure and Length-tension Measurements in Human Tracheal and Bronchial Segments. Journal of Applied Physiology 16, 170-172.

Dailey H L and Ghadiali S N, 2007. Fluid-structure analysis of microparticle transport in deformable pulmonary alveoli. Journal of Aerosol Science 38, 269 – 288.

Day J, Rubin J, Vodovotz Y, Chow C C, Reynolds A, and Clermont G, 2006. A Reduced Mathematical Model of the Acute Inflammatory Response II. Capturing Scenarios of Repeated Endotoxin Administration. Journal of Theoretical Biology 237-256.

Dhanireddy S, Altemeier W A, Matute-Bello G, O'Mahony D S, Glenny R W, Martin T R, and Liles W C, 2006. Mechanical Ventilation Induces Inflammation, Lung injury, and Extra-pulmonary Organ Dysfunction in Experimental Pneumonia. Laboratory Investigation 86, 790-799.

Dowling N E 1998 *Mechanical Behavior of Materials* 2 edn Prentice Hall, Upper Saddle River, NJ

Fan E, Needham D M, and Stewart T E, 2005. Ventilatory Management of Acute Lung Injury and Acute Respiratory Distress Syndrome. JAMA 294, 2889-2896.

Flaatten H, Gjerde S, Guttormsen A B, Haugen O, Høivik T, Onarheim H, and Aardal S, 2003. Outcome after acute respiratory failure is more dependent on dysfunction in other vital organs than on the severity of the respiratory failure. Critical Care 7, R72-R77.

Frank J A, Gutierrez J A, Jones K D, Allen L, Dobbs L, and Matthay M A, 2002. Low tidal volume reduces epithelial and endothelial injury in acid-injured rat lungs. American Journal of Respiratory and Critical Care Medicine 165, 242-249.

Gattinoni L, Carlesso E, Cadringher P, Valenza F, Vagginelli F, and Chiumello D, 2003. Physical and Biological Triggers of Ventilator-induced Lung Injury and its Prevention. European Respiratory Journal 47 (suppl.), 15S-25S.

Goldstein I, Bughalo M T, Marquette C H, Lenaour G, Lu Q, and Rouby J J, 2001. Mechanical Ventilation-induced Air-space Enlargement during Experimental Pneumonia in Piglets. American Journal of Respiratory and Critical Care Medicine 163, 958-964.

Guan X, Segal R A, Shearer M, and Martonen T B, 2000. Mathematical Model of Airflow in the Lungs of Children II: Effects of Ventilatory Parameters. Computational and Mathematical Methods in Medicine 3, 51-62.

Habib R H, Chalker R B, Suki B, and Jackson A C, 1994. Airway Geometry and Wall Mechanical Properties Estimated from Subglottal Input Impedance in Humans. Journal of Applied Physiology 77, 441-451.

Halbertsma F J J, Vaneker M, Scheffer G J, and Hoeven J G v d, 2005. Cytokines and Biotrauma in Ventilator-induced Lung Injury: A Critical Review of the Literature. The Netherlands Journal of Medicine 63, 382-392.

Hammerschmidt S, Kuhn H, Grasenack T, Gessner C, and Wirtz H, 2004. Apoptosis and Necrosis Induced by Cyclic Mechanical Stretching in Alveolar Type II Cells. American Journal of Respiratory Cell And Molecular Biology 30, 396-402.

Hancioglu B, Swigon D, and Clermont G, 2007. A Dynamical Model of Human Immune Response to Influenza A Virus Infection. Journal of Theoretical Biology 246, 70-86.

Haseneen N A, Vaday G G, Zucker S, and Foda H D, 2002. Mechanical Stretch Induces MMP-2 Release and Activation in Lung Endothelium: Role of EMMPRIN. American Journal of Physiology: Lung Cellular and Molecular Physiology 284, L541-L547.

Heistracher T and Hofmann W, 1995. Physiologically Realistic Models of Bronchial Airway Bifurcations. Journal of Aerosol Science 26, 497-509.

Hlastala M P and Berger A J 2001 *Physiology of Respiration* Oxford University Press, New York, NY

Horsfield K and Cumming G, 1967. Angles of Branching and Diameters of Branches in the Human Bronchial Tree. Bull Math Biophys 29, 245-259.

Howell J N, Chleboun G, and Conatser R, 1993. Muscle stiffness, strength loss, swelling and soreness following exercise-induced injury in humans. Journal of Physiology 464, 183-196.

ICRP 1994 *Human Respiratory Tract Model for Radiological Protection* Elsevier Science Ltd., New York, NY

Imai Y and Slutsky A S, 2006. Systemic Effects of Mechanical Ventilation. In: Dreyfuss D, Saumon G, and Hubmayr R D (eds), *Ventilator-Induced Lung Injury.* Taylor & Francis Group, New York, NY, pp. 267-285.

Ito S, Ingenito E P, Brewer K K, Black L D, Parameswaran H, Lutchen K R, and Suki B, 2005. Mechanics, nonlinearity, and failure strength of lung tissue in a mouse model of emphysema: possible role of collagen remodeling. Journal of Applied Physiology 98, 503-511.

Jaeschke H and Smith C W, 1997. Mechanisms of neutrophil-induced parenchymal cell injury. Journal of Leukocyte Biology 61, 647-653.

Janeway C A, Travers P, Walport M, and Capra J D 1999 *Immunobiology* 4 edn Garland Publishing, New York, NY

Jiang H and Stephens N L, 1990. Contractile properties of bronchial smooth muscle with and without cartilage. Journal of Applied Physiology 69, 120-126.

Kamm R D, 1999. Airway wall mechanics. Annual Review of Biomedical Engineering 1, 47-72.

Khadaroo R G and Marshall J C, 2002. ARDS and the multiple organ dysfunction syndrome: Common mechanisms of a common systemic process. Critical Care Clinics 18, 127-141.

Khilnani G C, Banga A, and Sharma S K, 2004. Predictors of mortality of patients with acute respiratory failure secondary to chronic obstructive pulmonary disease

admitted to an intensive care unit: A one year study. BMC Pulmonary Medicine 4, doi:10.1186/1471-2466-4-12,

Kleinstreuer C and Zhang Z, 2003. Targeted Drug Aerosol Deposition Analysis for a Four-Generation Lung Airway Model with Hemispherical Tumors. Journal of Biomechanical Engineering 125, 197-206.

Kumar R, Clermont G, Vodovotz Y, and Chow C C, 2004. The Dynamics of Acute Inflammation. Journal of Theoretical Biology 230, 145-155.

Longest P W and Kleinstreuer C, 2005. Computational Models for Simulating Multicomponent Aerosol Evaporation in the Upper Respiratory Airways. Aerosol Science and Technology 39, 124-138.

Longest P W, Vinchuarkar S, and Martonen T B, 2006. Transport and Deposition of Respiratory Aerosols in Models of Childhood Asthma. Journal of Aerosol Science 37, 1234-1257.

Longest P W and Vinchurkar S, 2007. Effects of Mesh Style and Grid Convergence on Particle Deposition in Bifurcating Airway Models with Comparisons to Experimental Data. Medical Engineering and Physics 29, 350-366.

Lumb A B 2005 *Nunn's Applied Respiratory Physiology* 6 edn Butterworth Heinemann, Italy

Luo H Y, Liu Y, and Yang X L, 2007. Particle Deposition in Obstructed Airways. Journal of Biomechanics 40, 3096-3104.

Ma X, Cheng Z, Kong H, Wang Y, Unruh H, Stephens N L, and Laviolette M, 2002. Changes in Biophysical and Biochemical Properties of Single Bronchial Smooth Muscle Cells from Asthmatic Subjects. Am J Physiol Lung Cell Mol Physiol 283, L1181-L1189.

Makhsous M, Venkatasubramanian G, Chawla A, Pathak Y, Priebe M, Rymer W Z, and Lin F, 2006. Investigation of Soft-Tissue Stiffness Alteration in Denervated Human Tissue Using an Ultrasound Indentation System. The Journal of Spinal Cord Medicine 31, 88-96.

Martonen T B and Guan X, 2001a. Effects of Tumors on Inhaled Pharmacologic Drugs I: Flow Patterns. Cell Biochemistry and Biophysics 35, 233-243.

Martonen T B and Guan X, 2001b. Effects of Tumors on Inhaled Pharmacologic Drugs II: Particle Motion. Cell Biochemistry and Biophysics 35, 245-253.

Martonen T B, Yang Y, and Xue Z Q, 1994. Effects of Carinal Ridge Shapes on Lung Airstreams. Aerosol Science and Technology 21, 119-136.

Nassif P S, Simpson S Q, Izzo A A, and Nicklaus P J, 1997. Interleukin-8 concentration predicts the neutrophil count in middle ear effusion. Laryngoscope 107, 1223-1227.

Okada M, Matsumori A, Ono K, Furukawa Y, Shioi T, Iwasaki A, Matsushima K, and Sasayama S, 1998. Cyclic Stretch Upregulates Production of Interleukin-8 and Monocyte Chemotactic and Activating Factor/Monocyte Chemoattractant Protein-1 in Human Endothelial Cells. Arteriosclerosis, Thrombosis, and Vascular Biology 18, 894-901.

Plopper C G, Nishio S J, and Schelegle E S, 2003. Tethering Tracheobronchial Airways within the Lungs. American Journal of Respiratory and Critical Care Medicine 167, 2-3.

Prakash U B S and Hyatt R E, 1978. Static Mechanical Properties of Bronchi in Normal Excised Human Lungs. Journal of Applied Physiology 45, 45-50.

Pugin J, Dunn I, Jolliet P, Tassaux D, Magnenat J-L, Nicod L P, and Chevrolet J-C, 1998. Activation of human macrophages by mechanical ventilation in vitro. American Journal of Physiology: Lung Cellular and Molecular Physiology 275, L1040-L1050.

Pugin J and Oudin S, 2006. Cellular and molecular basis for ventilator-induced lung injury. In: Dreyfuss D, Saumon G, and Hubmayr R D (eds), *Ventilator-induced lung injury.* Taylor & Francis Group, New York, NY.

Ranieri V M, Suter P M, Tortorella C, Tullio R D, Dayer J M, Brienza A, Bruno F, and Slutsky A S, 1999. Effect of Mechanical Ventilation on Inflammatory Mediators in Patients with Acute Respiratory Distress Syndrome. JAMA 281, 54-61.

Reddy J N 1993 *An Introduction to the Finite Element Method* 2 edn McGraw-Hill, New York, NY

Reitz B, Gayou O, Parda D S, and Miften M, 2008. Monitoring tumor motion with on-line mega-voltage cone-beam computed tomography imaging in a cine mode. Physics in Medicine and Biology 53, 823-836.

Reynolds A, Rubin J, Clermont G, Day J, Vodovotz Y, and Ermentrout G B, 2006. A Reduced Mathematical Model of the Acute Inflammatory Response: I. Derivation of Model and Analysis of Anti-inflammation. Journal of Theoretical Biology 242, 220-236.

Reynolds H N, McCunn M, Borg U, Habashi N, Cottingham C, and Bar-Lavi Y, 1998. Acute respiratory distress syndrome: estimated incidence and mortality rate in a 5 million-person population base. Critical Care 2, 29-34.

Ruffini E, Parola A, Papalia E, Filosso P L, Mancuso M, Oliaro A, Actis-Dato G, and Maggi G, 2001. Frequency and mortality of acute lung injury and acute respiratory distress syndrome after pulmonary resection for bronchogenic carcinoma. European Journal of Cardio-thoracic Surgery 20, 30-37.

Sather J E and Schuur J D, 2007. Epidemiology of acute respiratory failure and mechanical ventilation in u.s. emergency departments, 1993-2004. Annals of Emergency Medicine 50, S110.

Schultz M, Sanchez R O, Hernandez N E, and Hernandez J M, 2001. Nosocomial infection among immunosuppressed patients in the intensive care unit. Critical Care Nursing Quarterly 24, 55-63.

Segal R A, Guan X, Shearer M, and Martonen T B, 2000. Mathematical Model of Airflow in the Lungs of Children I: Effects of Tumor Sizes and Location. Computational and Mathematical Methods in Medicine 2, 199-213.

Segovia-Juarez J L, Ganguli S, and Kirschner D, 2004. Identifying control mechanisms of granuloma formation during *M. tuberculosis* infection using an agent-based model. Journal of Theoretical Biology 231, 357-376.

Sera T, Satoh S, Horinouchi H, Kobayashi K, and Tanishita K, 2003. Respiratory Flow in a Realistic Tracheostenosis Model. Journal of Biomechanical Engineering 125, 461-471.

Sinclair S E, Molthen R C, Haworth S T, Dawson C A, and Waters C M, 2007. Airway Strain during Mechanical Ventilation in an Intact Animal Model. American Journal of Respiratory and Critical Care Medicine 176, 786-794.

Swartz M A, Tschumperlin D J, Kamm R D, and Drazen J M, 2001. Mechanical Stress is Communicated between Different Cell Types to Elicit Matrix Remodeling. PNAS 98, 6180-6185.

Tobin M J, 2001. Advances in Mechanical Ventilation. The New England Journal of Medicine 344, 1986-1996.

Tremblay L, Valenza F, Ribeiro S P, Li J, and Slutsky A S, 1997. Injurious Ventilatory Strategies Increase Cytokines and c-fos m-RNA Expression in an Isolated Rat Lung Model. Journal of Clinical Investigation 99, 944-952.

Tschumperlin D J and Drazen J M, 2006. Chronic effects of mechanical force on airways. Annual Review of Physiology 68, 563-583.

Tschumperlin D J and Margulies S S, 1998. Equibiaxial deformation-induced injury of alveolar epithelial cells in vitro. American Journal of Physiology: Lung Cellular and Molecular Physiology 275, L1173-L1183.

Tschumperlin D J, Oswari J, and Margulies S S, 2000. Deformation-induced injury of alveolar epithelial cells. Effect of frequency, duration, and amplitude. American Journal of Respiratory and Critical Care Medicine 162, 357-362.

Vasilyev S, Schaap R N, and Mortensen J D, 1995. Hospital survival rates of patients with acute respiratory failure in modern respiratory intensive care units: an international, multicenter, prospective survey. Chest 107, 1083-1088.

Vassiliou M P, Petri L, Amygdalou A, Patrani M, Psarakis C, Nikolaki D, Georgiadis G, and Behrakis P K, 2000. Linear and nonlinear analysis of pressure and flow during mechanical ventilation. Intensive Care Medicine 26, 1057-1064.

Vinchurkar S and Longest P W, 2008. Evaluation of Hexahedral, Prismatic and Hybrid Mesh Styles for Simulating Respiratory Aerosol Dynamics. Computers and Fluids 37, 317-331.

Vlahakis N E, Schroeder M A, Limper A H, and Hubmayr R D, 1999. Stretch Induces Cytokine Release by Alveolar Epithelial Cells In Vitro. American Journal of Physiology: Lung Cellular and Molecular Physiology 277, L167-L173.

Weibel E R 1963 *Morphometry of the Human Lung* Academic Press, New York

Weisenhorn A L, Khorsandi M, Kasas S, Gotzos V, and Butt H-J, 1993. Deformation and height anomaly of soft surfaces studied with an AFM. Nanotechnology 4, 106-113.

Yamada H, 1970. Mechanical Properties of Respiratory and Digestive Organs and Tissues. In: Evans F G (ed.), *Strength of Biological Materials.* Williams & Wilkins, Baltimore, MD, p. 145.

Yang X L, Liu Y, and Luo H Y, 2006. Respiratory Flow in Obstructed Airways. Journal of Biomechanics 39, 2743-2751.

Zhang Y and Finlay W H, 2005. Measurement of the Effect of Cartilaginous Rings on Particle Deposition in a Proximal Lung Bifurcation Model. Aerosol Science and Technology 39, 394-399.

Zhao Y and Lieber B B, 1994. Steady Inspiratory Flow in a Model Symmetric Bifurcation. Journal of Biomechanical Engineering 116, 488-496.

VITA

PERSONAL INFORMATION

Date of Birth: August 18, 1980

Birthplace: Bangkok, Thailand

Nationality: Thai

EDUCATION

2005–Present   **Virginia Commonwealth University**, Richmond, VA
                     Ph.D. in Engineering
                     Field of study: Mechanical Engineering
                     Current GPA: 4.00/4.00
                     Dissertation topic: "Multiscale Modeling of Airway Inflammation
                     Induced by Mechanical Ventilation"
                     Expected graduation: August 2009

2003–2005   **Purdue School of Engineering and Technology, IUPUI**,
                     Indianapolis, IN
                     Master of Science in Mechanical Engineering
                     Field of study: Solid Mechanics
                     GPA: 4.00/4.00
                     Thesis topic: "An Investigation of Stress Distributions around a
                     Root Tooth using Finite Element Analysis"

1997–2001   **Chulalongkorn University**, Bangkok, Thailand
                     Bachelor of Engineering

Field of study: Mechanical Engineering
Specialty: Heating, Ventilation, and Air Conditioning
GPA: 3.02/4.00, Rank 10/75

HONORS AND AWARDS

- Highest GPA among PhD candidates and most published papers in Mechanical Engineering

- Golden Key International Honour Society

- The Gene Newman award for excellence in modeling and simulation research (Virginia Modeling, Analysis, and Simulation Center, Old Dominion University)

- VCU School of Engineering Teaching Assistantship

- VCU Graduate School Fellowship

TEACHING EXPERIENCE

Spring 2009   Department of Mechanical Engineering, Virginia Commonwealth University
Teaching Assistant for Energy Conversion System class

Spring 2009   Department of Mechanical Engineering, Virginia Commonwealth University
Guest lecturer for CAE Analysis class

Fall 2008   Department of Mechanical Engineering, Virginia Commonwealth University
Guest lecturer for Advance Solid Mechanics class

Fall 2007   Department of Mechanical Engineering, Virginia Commonwealth University
Guest lecturer for Design Optimization class

Fall 2007, 2008	Department of Mechanical Engineering, Virginia Commonwealth University Teaching Assistant for CAE Design class
Spring 2007, 2008	Department of Mechanical Engineering, Virginia Commonwealth University Teaching Assistant for CAE Analysis class
Fall 2006	Department of Mechanical Engineering, Virginia Commonwealth University Teaching Assistant for Dynamics class

RESEARCH EXPERIENCE

2005–Present	Department of Mechanical Engineering, Virginia Commonwealth University Graduate Research Assistant for Prof. Ramana Pidaparti
2004–2005	Department of Mechanical Engineering, Purdue School of Engineering and Technology, IUPUI Graduate Research Assistant for Prof. Jie Chen

WORK EXPERIENCE

2001–2003	Installation Section, Worachak International Company Limited; Thailand sole agent for Mitsubishi elevators and escalators Project control engineer for the first subway project in Thailand

PRESENTATIONS

- K. Koombua, R. M. Pidaparti, P. W. Longest, and G. M. Atkinson, "An Investigation of Fluid Characteristics in a Novel Microfluidic Device for Space Applications," AIAA Region I-MA Student Conference, University of Maryland, College Park, MD, April 2008.

- K. Koombua and R. M. Pidaparti, "Computational Modeling of Flow Patterns and Stresses in Human Respiratory Airway during Normal Gravity and Weightlessness Environment," presented at AIAA Region I Young Professional, Student and Education Conference (YPSE-07), Applied Physics Laboratory, Laurel, MD, November 2007.

- K. Koombua, R. M. Pidaparti, and G. Tepper, "A Novel Method for Drug Delivery System: Nanotube Implant," presented at the Virginia Nanotech 2006, Newport News, VA, June 2006.

CONFERENCE PUBLICATIONS

- K. Koombua and R. M. Pidaparti, "Design Simulations of a Micropump with Multiple Actuating Mechanisms," 2009 Nanotech Conference & Expo, Houston, TX, USA (2009)

- C. P. Cartin, K. Koombua, R. M. Pidaparti, and G. M. Atkinson, "Fabrication and Simulation of PDMS Valveless Micropump," ICMEMS 2009 - International Conference on MEMS, Chennai, India (2009)

- K. Koombua, R. M. Pidaparti, P. W. Longest, and G. M. Atkinson, "Micropump with Six Vibrating Membranes: Design Analysis," Proceedings of the ASME 2008 International Design Engineering Technical Conferences & Computers and Information in Engineering Conference, New York City, NY, USA (2008)

- K. Koombua, R. M. Pidaparti, P. W. Longest, and G. M. Atkinson, "Microfluidic Simulations of Micropump with Multiple Vibrating Membranes," Proceedings of the 11th International Conference on Modeling and Simulation of Microsystems, Boston, MA, USA (2008)

- K. Koombua and R. M. Pidaparti, "Modeling and Simulation of Fluid Dynamic Characteristics and Stresses during Inhalation," The 2008 Modeling, Simulation, & Gaming Student Capstone Conference, Old Dominion University, Norfolk, VA, April (2008), 1st place winner of the Gene Newman award

- K. Koombua, R. M. Pidaparti, and G. C. Tepper, "A Drug Delivery System Based on Polymer Nanotubes," Proceedings of 2nd IEEE International Conference on Nano/Micro Engineered and Molecular Systems, Bangkok, Thailand (2007)

- K. Koombua and R. M. Pidaparti, "Modeling and Simulation of an Idealized Nanoscale Motor," Proceedings of International Conference on Trends in Product Lift Cycle, Modeling, Simulation, and Synthesis, Bangalore, India (2006)

- K. Koombua, R. M. Pidaparti, P. W. Longest, and K. R. Ward, "Multidisciplinary Analysis for Fluid Dynamic Characteristics in Human Respiratory Airway," Proceedings of the 11th AIAA/ISSMO Multidisciplinary Analysis and Optimization Conference, Portsmouth, VA, USA (2006)

- K. Koombua, R. M. Pidaparti, and M. W. Beatty, "Fracture toughness of a bio-composite: TMJ disc," Proceedings of the 11th International Conference on Composites/Nano Engineering (ICCE-11), Hilton-Head, SC, USA (2004)

JOURNAL PUBLICATIONS

- R. M. Pidaparti, K. Koombua, and K. R. Ward, "Evaluation of Strain Levels Induced by Mechanical Ventilation," Cardiovascular Engineering (submitted)

- K. Koombua, C. P. Cartin, R. M. Pidaparti, and G. M. Atkinson, "Performance Evaluation of a Micropump with Multiple Pneumatic Actuators via Coupled Simulations," International Journal for Numerical Methods in Fluids (submitted)

- K. Koombua, R. M. Pidaparti, P. W. Longest, and G. M. Atkinson, "Evaluation of Performance Characteristics of a Novel Valveless Micropump," Nanoscale and Microscale Thermophysical Engineering (revised)

- K. Koombua, R. M. Pidaparti, P. W. Longest, and K. R. Ward, "Biomechanical Aspects of Compliant Airways due to Mechanical Ventilation," Molecular and Cellular Biomechanics, Vol. 151, pp.1-19 (2009)

- R. M. Pidaparti, K. Koombua, and A. S. Rao, "Corrosion Pit Induced Stresses Prediction from SEM and Finite Element Analysis," International Journal for Computational Methods in Engineering Science & Mechanics, Vol. 10, pp.117-123 (2009)

- R. M. Pidaparti, K. Koombua, I. Abdelsayed, and H. Sharma, "Degradation Experiments and Analysis of Corrosion Damage," International Journal of Damage Mechanics, Prepublished February 16, 2009, DOI:10.1177/1056789508098586

- K. Koombua and R. M. Pidaparti, "Stresses and Flow Characteristics in Human Airways during Inhalation through Fluid-Structure Interaction Analysis," Modelling and Simulation in Engineering, Volume 2008, Article ID 358748, 8 pages (2008)

- K. Koombua, R. M. Pidaparti, P. W. Longest, and K. R. Ward, "Computational Analysis of Fluid Characteristics in Rigid and Flexible Human Respiratory Airway Models," Engineering Applications of Computational Fluid Mechanics, Vol. 2, pp. 185-194 (2008)

- K. Koombua, R. M. Pidaparti, P. W. Longest, and K. R. Ward, "Computational Analysis of Flow Field Patterns in Rigid and Flexible Lung Airway Models," Journal of Critical Care, Vol. 21, pp. 343-344 (2006)

- K. Koombua, R. M. Pidaparti, and M. W. Beatty, "Fracture Toughness Estimation for the TMJ Disc," Journal of Biomedical Materials Research, Vol. 79A, pp. 566-573 (2006)